polymers

MDPI

Review

The Applications of Polymers in Solar Cells: A Review

Wenjing Hou [1], Yaoming Xiao [1,*], Gaoyi Han [1,*] and Jeng-Yu Lin [2,*]

[1] Institute of Molecular Science, Key Laboratory of Chemical Biology and Molecular Engineering of Education Ministry, Key Laboratory of Materials for Energy Conversion and Storage of Shanxi Province, Innovation Center of Chemistry and Molecular Science, Shanxi University, Taiyuan 030006, China; wjhou2016@sohu.com

[2] Department of Chemical Engineering, Tatung University, Taipei 104, Taiwan

* Correspondence: ymxiao@sxu.edu.cn (Y.X.); han_gaoyis@sxu.edu.cn (G.H.); jylin@ttu.edu.tw (J.-Y.L.)

Received: 28 November 2018; Accepted: 9 January 2019; Published: 15 January 2019

Abstract: The emerging dye-sensitized solar cells, perovskite solar cells, and organic solar cells have been regarded as promising photovoltaic technologies. The device structures and components of these solar cells are imperative to the device's efficiency and stability. Polymers can be used to adjust the device components and structures of these solar cells purposefully, due to their diversified properties. In dye-sensitized solar cells, polymers can be used as flexible substrates, pore- and film-forming agents of photoanode films, platinum-free counter electrodes, and the frameworks of quasi-solid-state electrolytes. In perovskite solar cells, polymers can be used as the additives to adjust the nucleation and crystallization processes in perovskite films. The polymers can also be used as hole transfer materials, electron transfer materials, and interface layer to enhance the carrier separation efficiency and reduce the recombination. In organic solar cells, polymers are often used as donor layers, buffer layers, and other polymer-based micro/nanostructures in binary or ternary devices to influence device performances. The current achievements about the applications of polymers in solar cells are reviewed and analyzed. In addition, the benefits of polymers for solar cells, the challenges for practical application, and possible solutions are also assessed.

Keywords: applications; polymers; solar cells

1. Introduction

The rapidly growing population and world economy have led to the continuously growing energy demand [1]. The enormous consumption of traditional fossil energy has resulted in the serious resource exhaustion and environmental pollution. One of the most imperative solutions is to look for alternative renewable energies. The solar energy stands out owing to solar is environmentally friendly and free from regional restrictions [1,2]. The solar cell is one of the most effective utilization approaches for solar energy. At present, the research and development of solar cells mainly focus on: (1) Mature silicon-based solar cells. Although the laboratory efficiency can reach more than 25% [3], the development of traditional silicon-based solar cells was limited by the sophisticated manufacturing process, high energy consumption and high cost [4]. (2) Thin-film solar cells. The typical thin-film solar cells include the gallium arsenide (GaAs) [5], copper indium gallium selenide (CIGS) [6], and cadmium telluride (CdTe) [7], etc. Although these thin-film solar cells have high efficiency and stability, the abundance of gallium and indium in the crust is low and cadmium is toxic. (3) Emerging solar cells. The emerging solar cells are represented by organic photovoltaics (OPV) [8], dye-sensitized solar cell (DSSC) [9] and perovskite solar cell (PSC) [10]. This kind of solar cells have the advantages of lightweight and low cost. However, there are some problems that limit their large-scale application.

For example, organic solar cells still need to be improved in conversion efficiency, spectrum response range and device stability [11]. Dye-sensitized solar cells based on liquid electrolyte are faced with the problems of easy electrolyte leakage and solvent evaporation, which undermine the long-term stability of the device [12]. The all-solid perovskite solar cell, which develops on the basis of DSSC but overcomes the shortcomings of DSSC, has attracted extensive attention from scientists as soon as they were reported. Even though the photoelectric conversion efficiency (PCE) of PSC has ranged from initial 3.8% to the latest 23.3% rapidly **(**Figure 1**)**, the device stability is still a problem that limited the applications [13–15]. Generally, each component of the device influences its performances, by performing their respective tasks. Hence, optimizing the device components is of great significance.

In the past few years, the polymers have been studied widely due to their versatile and adjustable chemical and physical properties [16]. The three-dimensional network structures of polymers decide that they can be employed as the template to fabricate mesoporous materials or be used as a polymeric matrix in solid electrolyte [17–19]; the high catalytic activity for I_3^- reduction make it potential as counter electrode materials. The diversified functional groups make it possible for the polymers to regulate the perovskite morphologies from bulk and interface aspects; the high carrier mobilities enable polymers acting as electron and hole transfer materials; the functional groups in polymers decide that they can be used as the interface layers to passivate defects, adjust the work function of the metal electrode, and improve the device performances [20,21]; the diversified structures and functional modification also equip polymers with various optical adsorption properties and variable electron mobility, being used as the photo-active layer or buffer layer in OPV [22,23]; The processability of polymer also make it possible to fabricate polymer-based micro/nanostructure devices. The partial polymers with good conductivity, named as conductive polymers, were widely used in many fields [24–26].

In this review, the applications of polymers in solar cells are mainly concentrated on DSSC, PSC, and OPV.

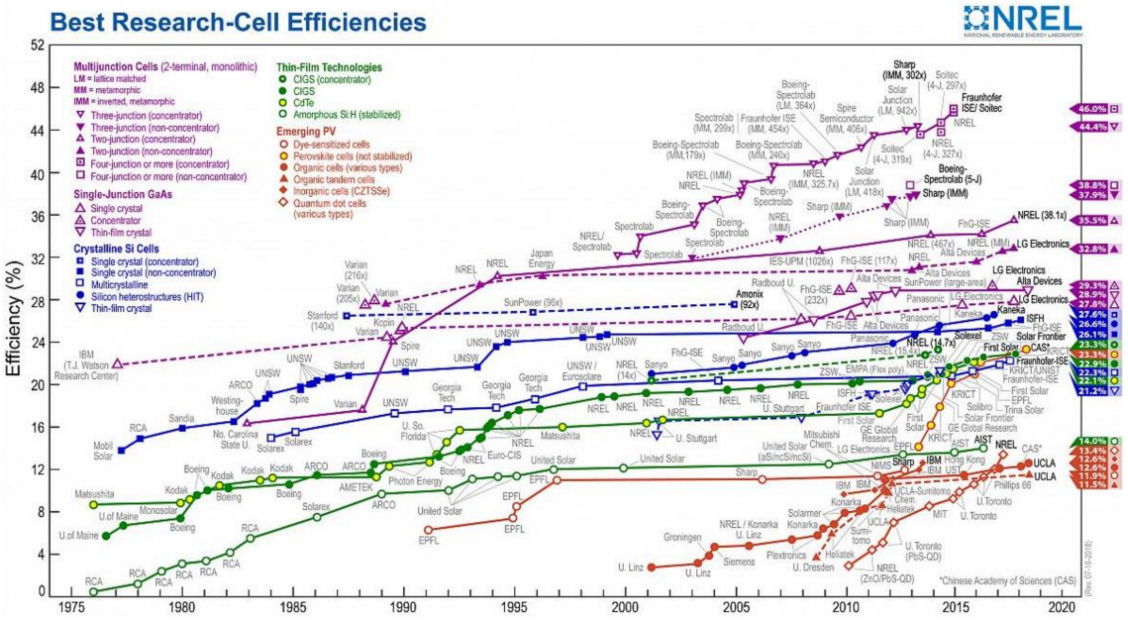

Figure 1. Photoelectric conversion efficiencies for various photovoltaic technologies since 1976 by National Renewable Energy Laboratory (NREL) [15].

2. Polymers in DSSC

Inspired by the photosynthetic process in plants, the O'Regan and Grätzel proposed the first prototype of DSSC in 1991 [27]. The DSSC has achieved stunning progress in recent years due to its low cost, excellent efficiency, and handy and eco-friendly fabrication process [28]. In DSSC, the electrolyte

was encapsulated between the anode and the counter electrode to form a sandwich structure. The principle of DSSC was shown in Figure 2 [29–33]. Generally, the electrons at excited state inject the conduction band (CB) of semiconductor, and then flow to the counter electrode through the external circuit. The oxidized electrolyte obtains the electrons from the counter electrode to produce the reduced electrolyte, realizing the electrolyte regeneration; The electron recombinations occur at these three parts and their interfaces. In this sense, the three parts of the DSSC play the imperative and indispensable roles in deciding the device performances. As we all know, the choosing and fabricating of constituent materials are crucial. Due to the various properties, the polymers can be applied into fabricating the constituent materials, such as: The polymers can be used to fabricate flexible substrates, to constitute mesoporous structure in anode, to prepare polymer gel electrolyte, and to catalyze electrolyte reduction as counter electrodes. The applications of polymers in DSSC are illustrated in the following sections in detail.

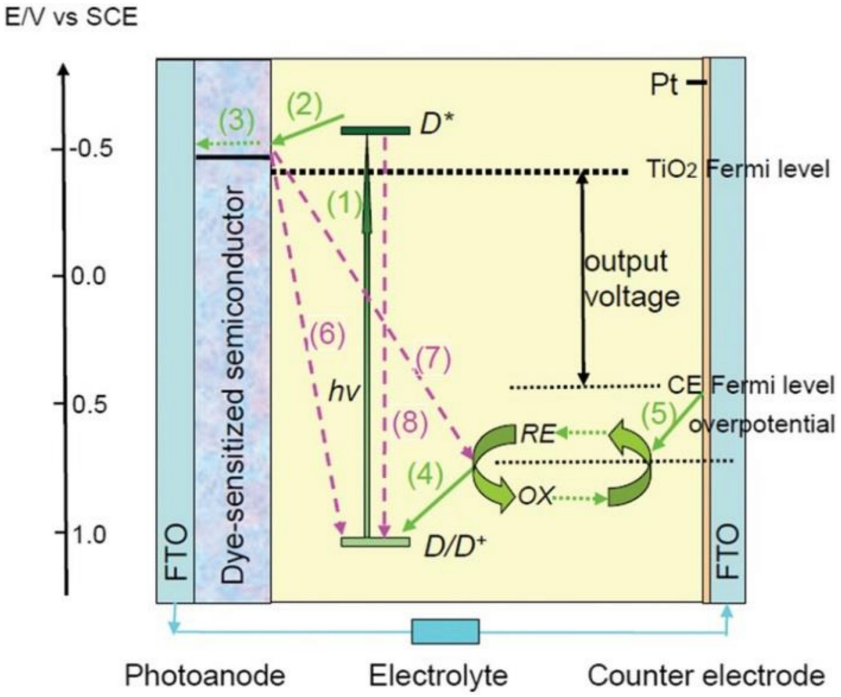

Figure 2. Fundamental processes of dye-sensitized solar cells (Reproduced from Reference [32] with permission, copyright The Royal Society of Chemistry, 2017).

2.1. Polymers as the Substrates of DSSC

Based on the principles of DSSC, the conductive substrate is responsible for supporting cells, transmitting light, collecting and transmitting electrons. The common conductive substrates include indium-doped tin oxide (ITO) glass, fluorine-doped tin oxide (FTO) glass, ITO/polyethylene terephthalate (PET), and ITO/polyethylene naphthalate (PEN). The ITO/PEN and ITO/PET are the most common conductive polymer substrates in DSSCs due to their low cost, high transparency, lightweight, flexibility, and low sheet resistance about 10–15 $\Omega \cdot sq^{-1}$ [34–37]. These merits of ITO/PEN and ITO/PET make it possible to fabricate the roll-to-roll solar cells and other flexible and wearable electronic devices [37]. In DSSCs, the substrates loaded with TiO_2 films often need to be sintered at 450–500 °C to guarantee the high crystallinity and purity of TiO_2. And the high temperature sintering also ensures the tight contact between the TiO_2 films and the conducting substrates [35,38]. Besides, the temperature above 400 °C also is applied to the pyrolysis of platinum (Pt) precursor in the fabrication of Pt counter electrode [38]. Nevertheless, the ITO/PEN and ITO/PET substrates are always sensitive to the high temperature [38]. Once the processing temperature exceeds 150 °C, the ITO/PET and ITO/PEN substrates begin to deform, and even melt at 235 °C [38,39]. The restricted processing temperature below 150 °C goes against the improvement of contact performances between conductive polymer

substrates and TiO_2 anode. These drawbacks inspire the developments of other low temperature deposition techniques.

2.2. Polymers in Mesoporous TiO_2 Photoanode of DSSC

The device performances of DSSC also depend on the photoanode largely. The photoanode in DSSC surves as the support for dye-absorbing, where the incident light is harvested and the electron transport takes place [40]. One of the most common photoanode materials is TiO_2 due to its photochemical stability, nontoxicity, and adequate resources for synthesis [41–43].

In order to improve the dye sensitization effect of TiO_2 nanoparticles photoanode, TiO_2 films are required to have a large specific surface area, which can be realized by fabricating mesoporous TiO_2 film. The more pore structure is, the larger specific surface area is [43,44]. Benkstein and co-workers have reported that the porosity in photoanode film can be realized by applying polymers as pore-forming regent [45]. In the subsequent annealing process, the polymers in photoanode films can be sintered, leaving the pores in their original positions [31,32,45]; and the content of polymers in the photoanode film can be used to control the porousness, which is ideally about 50−60% [31,46]. Excessive polymers create too many pores, which reduce the interconnects between particles and charge collection efficiency [46]. Hou et al. fabricated a series of mesoporous TiO_2 anodes by annealing the blade-coated TiO_2 films, which contain different content polyvinylpyrrolidone (PVP) [47]. The device based on the TiO_2 anode with 20 wt % PVP gives the highest conversion efficiency of 8.39%, approximately 56.63% higher than that of without PVP (5.36%). The enhanced efficiency can be ascribed to that moderately increased porosity can expose more specific surface areas, increasing the dye loading and enhancing the electron transfer and electrolyte diffusion efficiency further. The excessive PVP leads to small specific surface areas owing to excessive PVP reduced the connect between TiO_2 nanoparticles and increased the pore volume. Yun et al. synthesized two kinds of mesoporous TiO_2 photoanodes (MP-TiO_2 (A) and MP-TiO_2 (B)) by using tri-block copolymer (polyethylene oxide-polypropylene oxide-polyethylene oxide, P-123) and inorganic $ZnO/Zn(OH)_2$ templates, respectively [48]. The device based on the MP-TiO_2 (A) achieves the efficiency of 6.71%, higher than that based on the MP-TiO_2 (B) (3.05%) and pure P25 (5.62%). The best performances of MP-TiO_2 (A) based device can be attributed to the largest surface area, the largest pore size, and the largest pore volume of MP-TiO_2 (A) photoanode than other referential photoanodes [48], which can be benefited from the P-123 template. However, the electron mobility in TiO_2 nanoparticle systems is slow due to possible energy loss in the electron trapping process, which increases recombination risks in mesoporous photoanode films [49].

In order to solve above problem, the one-dimensional TiO_2 photoanodes (such as TiO_2 nanofibers and nanotubes) have been widely used in DSSCs due to their special feature: Directional electron transport along the fibers or tubes, and the reduced scattering effect [50]. The electrospinning method is initially used to fabricate the one-dimensional materials, including the one-dimensional TiO_2. Kokubo fabricated the multi-core cable-like TiO_2 nanofibrous membrane by electrospinning the dimethylformamide solution containing 11.5 wt % of polymer vinyl acetate (PVAc) and 1 g titanium isopropoxide and then calcinating the composite of PVAc/titania nanofibres at 500 °C [51]. Then the TiO_2 nanofibrous membrane was used as the photoanode of DSSC, obtaining the efficiency of 5.77%. Joshi fabricated the TiO_2 nanofiber photoanode by electrospinning the solution of isopropanol/demethylformamide containing Titanium n-butoxide (TNBT) and polyvinylpyrrolidone (PVP) and then pyrolysising [52]. The DSSC based on the TiO_2 nanofiber achieved the efficiency of 2.9%. The low efficiency can be deduced to the low dye uptake of 30.49×10^{-6} mol·g^{-1}, which can be attributed to the small specific surface area of TiO_2 nanofiber caused by large diameters [52]. In view of this problem, Joshi et al. prepared the composite TiO_2 nanofibers/nanoparticles (TiO_2 NPs/NFs) photoanode by electronspinning the PVP/TNBT nanofibers on the as-prepared TiO_2 nanoparticles and calcinating them, which obtains a greatly enhanced conversion efficiency of 8.8% [52]. He et al. prepared the TiO_2 photoanode with nanotubes structures by co-axial electrospinning the precursor solution of TNBT and PVP. The device based on the TiO_2 nanotubes photoanode can realize the efficiency of 3.80% [53].

Therefore, we can conclude that the polymers can be used to regulate the electron transfer in photoanode by influencing the porousness and morphologies of photoanodes.

2.3. Polymers as the Counter Electrodes of DSSC

The counter electrode (CE) in DSSC is responsible for catalyzing the reduction reaction of I_3^-, deciding the device performances further [54,55]. The excellent catalytic activity for I_3^- reduction equips the Pt serving as the most common counter electrode material [54]. However, the using of Pt CE hampered the further development and long-term stability of Pt-based DSSC due to its scarcity and possible corrosion in I_3^-/I^- electrolyte system [56]. Therefore, the overwhelming majority of research focuses on looking for alternative materials of Pt CE, such as carbon materials [57,58], metal alloys [59,60], transitional-metal compounds [61,62], conductive polymers [63–68] and corresponding composite [69–72]. Compared with other alternatives, the conductive polymers possess the properties of low cost, high catalytic activity, translucence, facile synthesis, and abundance, which decide the conductive polymers can act as one of the most ideal alternatives of Pt CE [63–68]. The polypyrrole, polyaniline, and poly(3,4-ethylenedioxythiophene) are commonly used as conductive polymers CEs materials.

2.3.1. Polypyrrole as the Counter Electrodes of DSSC

The easy synthesis process, high yield, favorable catalytic activity, and environmental stability make the polypyrrole (PPy) be a potential alternative of Pt CE [73–76]. Table 1 summarizes the photovoltaic performance parameters of DSSCs based on the PPy CEs. The PPy is often formed by polymerizing the pyrrole monomer, accompanying the color changing from yellow to blue or black. The polymerizations can be divided into chemical polymerization and electrochemical polymerization. For the chemical polymerization of PPy, the various oxidants can be used. Peng et al. synthesized the free-standing paper-like polypyrrole nanotube membrane CE by using the Iron(III) chloride hexahydrate ($FeCl_3 \cdot 6H_2O$) to oxidize the pyrrole monomer (Figure 3a,b). The device based on the PPy nanotube membrane counter electrode obtains the efficiency of 5.27%, being comparable with that of Pt CE (6.25%) [76]. Wu and co-workers fabricated the PPy CE by coating the iodine oxidation polymerized PPy nanoparticles on FTO. The device assembled with the PPy CE obtained a PCE of 7.66%, higher than that of Pt CE (6.90%) [77]. Bu et al. fabricated bifacial DSSC assembled with the transparent and stable PPy CE and giving the efficiency of 5.74%. In this case, the FTO was immersed into the mixed solution of the ammonium persulfate (APS) and pyrrole monomer at 0 °C for 3 h, where the APS was used as the oxidant [78]. Besides, Wang fabricated PPy CE with hierarchical nanostructure by using the vanadiumpentoxide (V_2O_5) nanofiber and $FeCl_3$ to oxidize the pyrrole monomer step by step. The best performing device realizes the efficiency of 6.78%, higher than that of PPy nanoparticles (5.41%), being 92.5% of Pt CE (7.33%) [79]. Besides, Xu et al. prepared the PPy-coated cotton fabrics CE by electrochemical polymerization, and the corresponding device obtains the efficiency of 3.83% [80]. Even copious amounts of research focus on the PPy CE, the device efficiencies based on the PPy CEs are disadvantaged. The main issues are concentrated on the high charge transfer resistance (R_{CT}) and low conductivity of PPy [81].

Table 1. Photovoltaic performances parameters of DSSCs based on the PPy counter electrodes.

Preparation Methods of PPy Counter Electrode	Electrolyte	J_{SC} (mA cm^{-2})	V_{OC} (V)	*FF* (%)	η (%)	Ref.
$FeCl_3$ chemical polymerization	$I3^-/I^-$	13.80	0.771	26.3	2.86	[64]
Potentiostatical electrodeposition	$I3^-/I^-$	13.10	0.660	53.9	4.65	[64]
$FeCl_3$ oxidation/Drop-casting	$I3^-/I^-$	15.50	0.791	67.0	8.20	[65]
$FeCl_3$ oxidation	$I3^-/I^-$	13.96	0.712	64.9	6.45	[73]
$FeCl_3$ oxidation/with HCl vapor post-doping	$I3^-/I^-$	11.90	0.725	63.2	5.70	[74]
$FeCl_3$ oxidation/without HCl vapor post-doping	$I3^-/I^-$	15.20	0.721	61.8	6.80	[74]
Liquid-liquid biphasic interfacial polymerization	$I3^-/I^-$	11.31	0.49	63.0	3.50	[75]
$FeCl_3$ oxidation/Heating pulp-like suspensions	$I3^-/I^-$	13.10	0.716	56.0	5.27	[76]
I_2 oxidation	$I3^-/I^-$	15.01	0.74	69.0	7.66	[77]
APS oxidation	$I3^-/I^-$	12.19	0.725	52.0	5.74	[78]
V_2O_5 nanofibers/$FeCl_3$ oxidation	$I3^-/I^-$	15.37	0.69	64.0	6.78	[79]

2.3.2. Polyaniline as the Counter Electrodes of DSSC

Except PPy, the polyaniline (PANI) is also the most studied conductive polymers due to its relatively low cost, multiple oxidation states with different colors, and acid/base doping responsiveness. Table 2 lists the photovoltaic performance parameters of DSSCs based on the PANI CEs. Li and Wu et al. prepared the microporous PANI CE with the average size diameter of 100 nm by perchloride acid doped APS oxidative polymerization. The device with PANI CE realized the efficiency of 7.15%, higher than that of Pt CE (6.90%) [82]. Compared with the random transport in PANI nanoparticles CE, the oriented morphologies are conducive to accelerate the electron transfer efficiency and enhance the device performances further. As Figure 3c,d shown, Hou et al. synthesized a polyaniline nanoribbon (PANI NR) CE with serrated, flexible and ultrathin nanostructures by using the electrospun V_2O_5 as template and oxidant to realize the in situ polymerization of aniline and etching the V_2O_5 template by acid [83]. The lots of active sites, good contact performance with substrate, and the oriented electron transfer along the nanoribbons equip the PANI NR based DSSC a PCE of 7.23%, which can be comparable to that of the Pt-based DSSC (7.42%). Wang et al. in-situ fabricated the oriented PANI nanowire counter electrode by immersing the FTO glass into the aniline/APS solution with the fixed mole ratio of 1.5 at 0–5 °C for 24 h. The obtained PANI nanowire CE exhibits higher cataltic activity and device performances (8.24%) than that of random PANI nanofibers (5.97%) and Pt CE (6.78%) [84]. The enhanced performance can be deduced to the effectively exposed PANI nanowires and the rapid electron transfer along the oriented nanowire. Besides, Xiao et al. fabricated the PANI CE with nanofiber structure by using the pulse potentiostatic electropolymerization method, giving the efficiency of 5.19%, up to 90% of Pt CE [85].

The previous research has indicated that the doping ions will influence the morphologies of electrode materials and corresponding electrochemical properties [86]. Li et al. compared the performances of different PANI films doped by various counter ions SO_4^{2-}, ClO_4^-, BF_4^-, Cl^-, and p-toluenesulfonate (TsO^-), etc. And the results revealed that the DSSC based on the PANI-SO_4^{2-} CE shows the efficiency of 5.6%, being comparable to that of Pt CE (6.0%) [87].

Even though PANI possesses the superior catalytic activities, high conductivity, simple fabrication process, the applications of PANI CE are still limited due to its carcinogenic and self-oxidation properties [88].

Table 2. Photovoltaic performance parameters of DSSCs based on the PANI counter electrodes.

Preparation Methods of PANI Counter Electrode	Electrolyte	J_{SC} (mA cm^{-2})	V_{OC} (V)	*FF* (%)	η (%)	Ref.
APS oxidation	$I3^-/I^-$	15.24	0.71	60.4	6.54	[63]
KPS oxidation	$I3^-/I^-$	13.50	0.76	38.3	3.92	[64]
cyclic voltammetry deposition	$I3^-/I^-$	13.40	0.728	67.6	6.58	[64]
APS oxidation	$I3^-/I^-$	14.60	0.714	69.0	7.15	[82]
V_2O_5 nanofibers oxidation/template etching	$I3^-/I^-$	17.92	0.72	56.0	7.23	[83]
In situ oxidation with fixed content of APS	$Co(bpy)^{33+/2+}$	15.09	0.78	70.0	8.24	[84]
Drop-casting	$Co(bpy)^{33+/2+}$	12.76	0.72	65.0	5.97	[84]
I-t electropolymerization	$I3^-/I^-$	10.88	0.69	58.0	4.35	[85]
Pulse electropolymerization	$I3^-/I^-$	12.18	0.71	60.0	5.19	[85]
Cyclic voltammetry deposition with SO_4^{2-} doping	$I3^-/I^-$	10.70	0.81	64.0	5.60	[87]

2.3.3. Poly(3,4-ethylenedioxythiophene) as the Counter Electrodes of DSSC

As another important conductive polymer, the poly(3,4-ethylenedioxythiophene) (PEDOT) presents the highest catalytic activity for I_3^- reduction and the highest conductivity (300–500 S·cm^{-1}) than those of PANI (0.1–5 S·cm^{-1}) and PPy (10–50 S·cm^{-1}) [89]. The existing conductivity has reached more than 4600 S·cm^{-1} by doping poly(styrene sulfonate) (PSS) [90]. Except for the high conductivity and catalytic activity, the excellent thermal and chemical stability, and electrochemical reversibility have made the PEDOT be an ideal material for DSSC CEs [90,91]. Table 3 enumerates the photovoltaic performance parameters of DSSCs based on the PEDOT CEs. Li et al. fabricated honeycomb-like PEDOT CE by a facile cyclic voltammetry electrodeposition and sacrificial template methods. The resultant device based on the honeycomb-like PEDOT CE exhibits the front efficiency of 9.12% and rear efficiency of 5.75%, outperforming than that of flat PEDOT (8.05% and 3.78%, respectively), which lights up the roads of bifacial and tandem devices [92]. Trevisan et al. fabricated the PEDOT nanotube arrays (Figure 3e,f) by combining the electrodeposition and template etching technique. The best performing device yielded the efficiency of 8.3% [93]. Xia et al. studied the influence of doping ions on the morphologies of PEDOT and corresponding device performances. The ClO_4^- and PSS doped PEDOT CE presented higher efficiencies than those of TsO^- doped PEDOT [94].

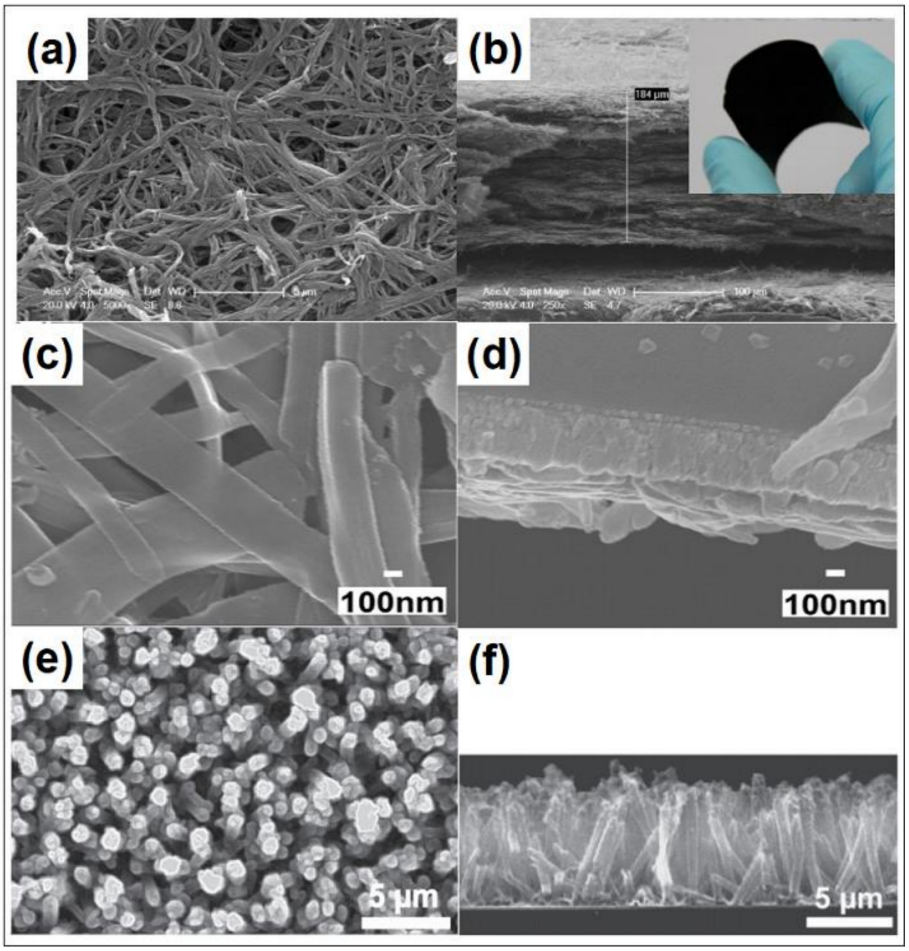

Figure 3. Field Emission Scanning Electron Microscope (FESEM) images and corresponding cross-sectional FESEM images of different conductive polymers counter electrodes: (**a**,**b**) Paper-like PPy membrane (reproduced from Reference [76] with permission, copyright American Chemical Society, 2014); (**c**,**d**) polyaniline (PANI) nanoribbons (reproduced from Reference [83] with permission, copyright Elsevier, 2016); and (**e**,**f**) PEDOT nanotubes (reproduced from Reference [93] with permission, copyright Wiley, 2011), respectively.

Table 3. Photovoltaic performances parameters of DSSCs based on the PEDOT counter electrodes.

Preparation Methods of PEDOT Counter Electrodes	Electrolyte	J_{SC} (mA cm^{-2})	V_{OC} (V)	*FF* (%)	η (%)	Ref.
$Fe(OTs)_3$ oxidative polymerization	$I3^-/I^-$	17.00	0.72	66.0	8.08	[69]
Constant current deposition	$I3^-/I^-$	13.96	0.7116	70.0	6.96	[70]
Potentiostatical electrodeposition	Disulfide/ thiolate	15.90	0.687	72.0	7.90	[86]
Electrochemical polymerization	$I3^-/I^-$	8.84	0.705	63.0	3.93	[91]
cyclic voltammetry/template etching	$I3^-/I^-$	16.75	0.75	64.0	8.05 (front)	[92]
cyclic voltammetry/template etching	$I3^-/I^-$	7.84	0.719	67.0	3.78 (rear)	[92]
cyclic voltammetry electrodeposition	$I3^-/I^-$	17.72	0.768	67.0	9.12 (front)	[92]
cyclic voltammetry electrodeposition	$I3^-/I^-$	11.23	0.731	70.0	5.75 (rear)	[92]
ZnO nanowire template/electropolerization	$I3^-/I^-$	16.24	0.72	70.0	8.30	[93]
Electropolymerization with ClO_4 doping	$I3^-/I^-$	9.60	0.68	66.0	4.20	[94]
Electropolymerization with TsO doping	$I3^-/I^-$	9.10	0.68	67.0	4.20	[94]
Electropolymerization with TsO doping	$I3^-/I^-$	9.20	0.665	66.0	4.0	[94]

2.3.4. The Hybrids Based on Conductive Polymers as the Counter Electrodes of DSSC

Even the conductive polymers present the high catalytic activity for I_3^- reduction, the conductivity of them are still limited due to their semiconductor nature [89]. Therefore, the hybrids based on the conductive polymers have been studied to improve the device performances (Figure 4 and Table 4). The hybrids make the utmost of the synergetic effects of corresponding components. The conductive polymers-based hybrids include the following three parts: (1) Conductive polymers/carbon materials [95–101]; (2) conductive polymers/transitional metal compounds [102,103]; and (3) conductive polymers/conductive polymers [104,105].

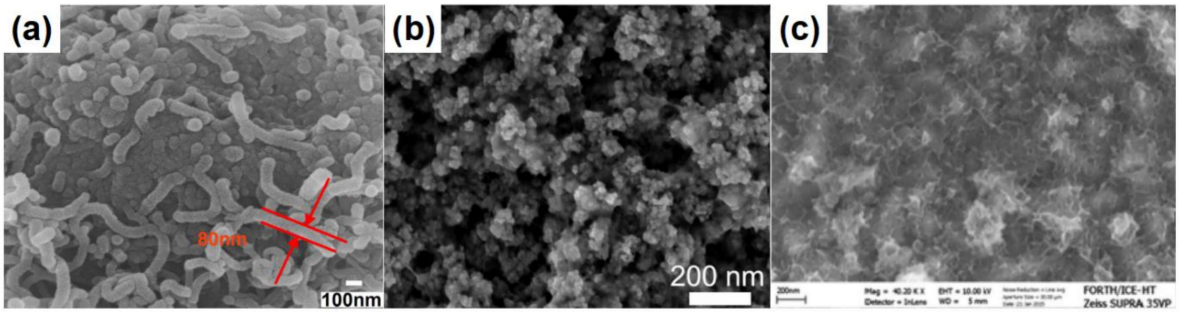

Figure 4. FESEM images of different hybrids counter electrodes based on conductive polymers: (**a**) PPy/MWCNT (reproduced from Reference [101] with permission, copyright Elsevier, 2016); (**b**) TiN particles-PEDOT:PSS (reproduced from Reference [102] with permission, copyright American Chemical Society, 2012); and (**c**) RGO/PPy/PEDOT composites (reproduced from Reference [104] with permission, copyright Elsevier, 2015), respectively.

The carbon materials are used for the hybrids due to their excellent conductivity, such as single/multi-wall carbon nanotube (SWCNT/MWCNT), graphene, and carbon black nanoparticles, and carbon nanofibers, etc. [96–101]. The composites of conductive polymers/carbon materials combine the excellent conductivity of carbon materials with the high catalytic activity of conductive polymers, which accelerate the charge transfer in counter electrodes. He et al. fabricated the composite CE of PANI/graphene by electrodepositing the aniline-graphene complex. The device based on the PANI-8 wt ‰ graphene CE displayed the efficiency of 7.70%, which is superior to that of pure PANI CE (6.40%) [96]. Zhang et al. prepared the PANI-8 wt ‰ MWCNT CE with high transmittance by using the electrodeposition methods, achieving a front efficiency of 7.91%, rear efficiency of 1.72%, and the maximum efficiency of 9.24%, higher than that of pure PANI CE [97]. Compared to pure PPy CE, the DSSC based on the PPy-2 wt ‰ SWCNT CE also presented the enhanced short current density and efficiency [98]. Xiao's group systematically prepared a series of composite CEs of conductive polymers and MWCNT (PANI/MWCNT, PEDOT/MWCNT, and PPy/MWCNT), which yielded the enhanced efficiencies compared to their corresponding component materials, respectively [99–101].

Xu and Cui et al. synthesized the TiN-PEDOT:PSS hybrid CE by simple physical mixing and scraping. The device with the TiN-PEDOT:PSS hybrid CE obtained the enhanced performances owing to that the TiN-PEDOT:PSS hybrid CE ensures the good contact between the TiN-PEDOT:PSS and FTO substrate and avoids the TiN from aggregating [102]. Di et al. fabricated the composite CEs of transitional metal phosphates ($Ni_3(PO)_4$, $Co_3(PO)_4$, and $Ag_3(PO)_4$) and PEDOT. The device assembled with the $Ni_3(PO)_4$-PEDOT CE realized the efficiency of 6.412%, higher than that of $Co_3(PO)_4$-PEDOT CE (6.109%), $Ag_3(PO)_4$-PEDOT CE (3.731%), and original PEDOT CE (5.443%) [103]. The composite PEDOT:PSS/PPy CE was synthesized and the device based on the PEDOT:PSS/PPy CE gave the efficiency of 7.60%, higher than that of PEDOT:PSS (6.31%) and PPy (5.23%), and 98.3% of Pt (7.73%) [105].

These hybrid CEs take the advantage of the high catalytic activity of conductive polymers, the high conductivity of carbon materials, the large specific surface area of transitional metal compounds, hence improving the device efficiency.

Table 4. Photovoltaic performances parameters of DSSCs assembled with conductive polymers-based hybrids counter electrode.

Counter Electrodes	Preparation Methods	Electrolyte	J_{SC} (mA·cm^{-2})	V_{OC} (V)	*FF* (%)	η (%)	Ref.
PEDOT/*N*-doped GO	Constant current deposition	I_3^-/I^-	15.60	0.7392	72.0	8.30	[70]
rGO@PPy	Electrochemical polymerization	I_3^-/I^-	7.49	0.70	42.0	2.21	[71]
PPy/FeS	$FeCl_3$ oxidation/ Na_2S reduction	I_3^-/I^-	15.87	0.711	66.3	7.48	[73]
PANI-graphene	Cyclic voltametric	I_3^-/I^-	16.55	0.699	67.0	7.70	[96]
PANI-MWCNT	Cyclic voltametric	I_3^-/I^-	22.25	0.691	60.1	9.24 (both)	[97]
PANI-MWCNT	Cyclic voltametric	I_3^-/I^-	17.95	0.675	65.3	7.91 (front)	[97]
PANI-MWCNT	Cyclic voltametric	I_3^-/I^-	4.30	0.622	64.3	1.72 (rear)	[97]
PPy-SWCNT	$FeCl_3$ oxidation	I_3^-/I^-	15.68	0.742	71.0	8.30	[98]
PANI-MWCNT	Pulse potentiostatic	I_3^-/I^-	13.53	0.721	64.0	6.24	[99]
PEDOT/MWCNT	Cyclic voltametric/ PMMA template	I_3^-/I^-	17.09	0.792	67.0	9.07 (front)	[100]
PEDOT/MWCNT	Cyclic voltametric/ PMMA template	I_3^-/I^-	10.76	0.757	69.0	5.62 (rear)	[100]
TiN(P)-PEDOT:PSS	Doctor blade	I_3^-/I^-	14.45	0.727	67.18	7.06	[102]
TiN(R)-PEDOT:PSS	Doctor blade	I_3^-/I^-	14.53	0.727	65.26	6.89	[102]
TiN(S)-PEDOT:PSS	Doctor blade	I_3^-/I^-	14.35	0.724	59.48	6.18	[102]
PEDOT-$Ni_3(PO_4)_2$	Spin-coating	I_3^-/I^-	12.21	0.746	70.3	6.412	[103]
PEDOT-$Co_3(PO_4)_2$	Spin-coating	I_3^-/I^-	12.05	0.724	69.6	6.109	[103]
PEDOT-$Ag_3(PO_4)_2$	Spin-coating	I_3^-/I^-	11.08	0.762	44.1	3.731	[103]
rGO/PPy/PEDOT	APS oxidation/ potentiostatic deposition	I_3^-/I^-	17.0	0.76	55.0	7.1	[104]
PEDOT:PSS/PPy	Electrochemical polymerization	I_3^-/I^-	14.27	0.75	71.0	7.60	[105]

2.4. Polymers as the Electrolyte of DSSC

As one of the most imperative components in DSSCs, the electrolyte undertakes the responsibility for transferring carrier, regenerating the dye and itself [106]. The electrolyte exerts dominated influences on the device performances by influencing the related performance parameters, such as the short current density (J_{SC}), open-circuit voltage (V_{OC}), and fill factor (*FF*) [29,107,108]. Specifically speaking, the transfer rate of redox couple in electrolyte will affect the J_{SC} [29,107]. The charge transfer impedance at the interfaces of electrolyte/electrodes has non-ignorable impacts on the *FF* [29,107]. The V_{OC} is a function associated with the femi energy level of the photoanode and the redox potential of the electrolyte [29,108]. Hence, the research about the electrolyte are necessary. The charge transfer in electrolyte is controlled by diffusion, which can be affected by the components, the concentration of redox couple, the viscosity of the solvent, and the distance between photoanode and counter electrode [29,109].

In 1991, O'Regan and Grätzel first employed the organic solvent containing the redox couple (such as I^-/I_3^-) as the electrolyte in DSSCs and achieved an efficiency of 7.0–7.9% [27]. Since then, the liquid electrolytes have been utilized universally. The devices with high efficiency (13%) and champion efficiency (14.3%) are also based on the liquid electrolyte [110–112]. The corrosion of the CE materials, and the degradation and desorption of dye all have a great relationship with the liquid electrodes [113,114]. Meanwhile, the leakage of liquid electrolytes and the volatilization of the solvent all damage the device performances and stability [113,114]. The quasi-solid-state polymer electrolytes are promising to serve as the alternatives of liquid electrolyte, because they are conducive to improve the sealing and stability [29,114–116]. The quasi-solid-state electrolyte are often fabricated by solidifying the liquid electrolyte solution using the organic polymer gelatin [29,114]. Therefore, the organic solvent, polymer or oligomer, and inorganic salt are the indispensable components of quasi-solid-state electrolyte [29]. According to the types of interaction in electrolyte, the polymers-based quasi-solid-state electrolytes can be divided into the thermoplastic polymer

electrolyte, thermosetting polymer electrolyte, and composite polymer electrolyte [29], which are widely used in the DSSCs (Table 5).

2.4.1. Thermoplastic Polymers as the Electrolyte of DSSC

For the thermoplastic polymer electrolyte, the polymer or oligomer fabricates the polymer framework firstly. After mixing the liquid electrolyte with the polymer framework, the system gradually becomes into a viscous gel state under the stimulus of temperature, where the gelatin, adsorption, inflation and polymer assembling processes occur [29,117]. The solvent in liquid electrolyte diminishes the interactions between polymer chains by forming the van der waals and electrostatic interaction with polymers [29,117]. These weak interactions permit the moderate solvent keeping in the gel, presenting the excellent interfacial wetting and filling properties, and high ionic conductivity [29,117,118]. Meanwhile, limited by the polymer matrix, the thermoplastic polymer electrolyte shows the merits of solid electrolyte.

The common polymer gelatin in thermoplastic polymer electrolyte include the poly(acrylonitrile) (PAN), poly(ethylene oxide) (PEO or PEG), PVP, poly(vinylidene ester) (PVE), polystyrene (PS), poly(vinyl chloride) (PVC), poly(methyl methacrylate) (PMMA), and poly(vinylidene fluoride) (PVDF), etc. Cao et al. first fabricated the thermoplastic polymer electrolyte by introducing the I_2/NaI-based liquid electrolyte into PAN polymer [119]. The device assembled with this electrolyte obtains the excellent performances and stability. Wu et al. employed the liquid electrolyte of ethylene asrbonate (EC)/prpopylene carbonate (PC)/N-methyl pyridine iodide and poly(acrylonitrile-*co*-stryrene) matrix to fabricate the gel state electrolyte and obtained the efficiency of 3.10% [120]. Wu et al. synthesized the PC/PEG/KI/I_2 gel electrolyte and achieved the efficiency of (7.22%), being competed to that of liquid electrode (7.60%) [121]. The functional groups make PEO and PEG enhancing the ionic conductivity by forming the interaction with the alkali metal cations and leaving the free-moving iodide anions, thus reducing the recombination and enhancing the device performances [122]. Lee et al. injected the liquid electrolyte into the gap between photoanode and couner electrode coated with PS (Figure 5). The PS is dissolved and becomes into gel state once uptaking the liquid electrolyte. The device based on this gel electrolyte and the liquid electrolyte exhibited the similar efficiency of 7.59% and 7.54%, respectively [123].

Even the utilizations of gel-based electrolytes improve the device stability by avoiding the electrolyte leakage, it is still dilemma to control the ratios of polymers and liquid electrolyte [29,124]. Excessive polymers host will retard the ionic movement [29,124]. Excessive liquid electrolyte will lead to the sealing problem.

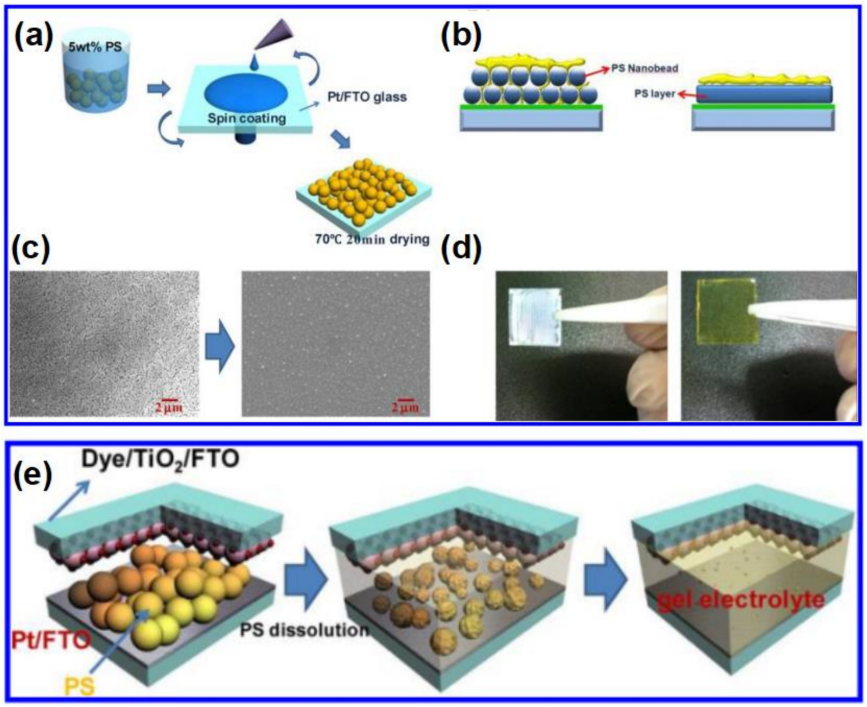

Figure 5. (**a**) Preparation schematic of PS nanobeads on FTO/Pt substrate; (**b**) Comparison schematic of the pore-filling before (left) and after (right) dissolving the PS nanobeads; (**c** and **d**) FESEM images and photographs of the PS nanobeads on the FTO/Pt substrate before (left) and after (right) the dissolution process; (**e**) Conversion schematic of liquid electrolyte to gel electrolyte by using valeronitrile solvent to dissolve the PS nanobeads (reproduced from Reference [123] with permission, copyright American Chemical Society, 2012).

2.4.2. Thermosetting Polymers as the Electrolyte of DSSC

For thermosetting polymer electrolyte, the states cannot change with temperature. Under the stimulus of light or heat, the organic molecules in the mixed solution in-situ cross-link to form the thermosetting polymer electrolyte through chemical covalent interaction, in which, the liquid electrolytes were wrapped with entangled polymer matrix [29,125]. This method can help the electrolytes in-situ fill into the gel electrolyte. Besides, swelling the cross-linked macromoleculor polymer in liquid electrolyte is another representative method to prepare the thermosetting polymer electrolyte [29,126]. For the DSSC device, the electrolyte filling in the electrodes is of great significance. Compared with the liquid electrolyte, it is difficult for the gel electrolyte to impregnate into the mesoporous TiO_2 film [127]. Parvez et al. infiltrated mesoporous TiO_2 film with the polymer monomer solution firstly [127]. After treating by the UV light illumination, poly(ethylene glycol) (PEG) and poly(ethyleneglycol) diacrylate (PEGDA) formed the crosslinked gel structure without damaging the device components. The efficiency and the long-term stability are all enhanced. Wang et al. prepared a novel necklace-like polymer gel electrolyte by heating the precursors of PPDD/I_2/I^-/NMBI/TBP and obtained the efficiency of 7.72%, where the PPDD is polypyridyl-pendant poly(amidoamine) dendritic derivatives, NMBI reprents the *N*-methylbenzimidazole, TBP refers to the tert-butylpyridine [128]. As depicted in Figure 6, Wu et al. synthesized the PEG/PAA/I_2/I^- gel electrolyte by taking advantage of the amphipathy of PEG and the superabsorbent of PAA to absorb the liquid electrolyte. The device with the PEG/PAA/I_2/I^- gel electrolyte achieved an efficiency of 6.10%, which is comparable to that based the liquid electrolyte (6.70%) [129].

Despite tremendous efforts have been devoted in gel electrolyte, the J_{SC} of devices based on polymer gel electrolytes are still lower than that assembled with liquid electrolyte due to the limited conductivity [129].

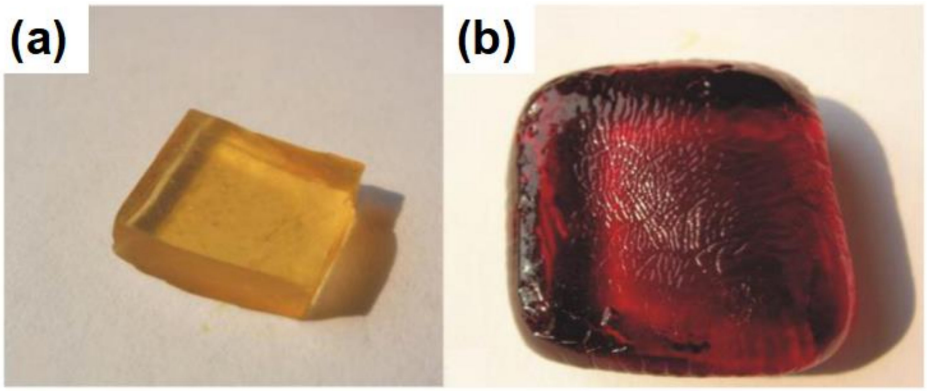

Figure 6. Photographs of thermosetting polymer electrolyte (PAA-PEG/NMP + GBL/NaI + I_2): (**a**) Before and (**b**) after soaking in I_3^-/I^- liquid electrolyte, respectively (reproduced from Reference [129] with permission, copyright Wiley, 2007).

2.4.3. Composite Polymer as the Electrolyte of DSSC

Apart from the thermoplastic and thermosetting polymer electrolytes, the composite polymers are also one kind of the most common electrolytes. The copmosite polymer electrolytes are fabricated by adding the inorganic nanoparticles into the liquid electrolyte containing the polymers, where the inorganic nanoparticles serve as the gelatins to solidify the liquid electrolyte and to enlarge the amorphous phase in electrolyte [29,130]. In this type of electrolytes, the introducing of inorganic nanoparticles can enhance ionic conductivity and device stability. The fabrication of PEO/TiO_2/LiI/I^- composite electrolyte creates the space for I^-/I_3^- migration due to the arrangement of TiO_2 in the polymer network [131]. Yoon et al. used the spherelike and rodlike SiO_2 as the gelatins of poly(ethylene glycol) dimethyl ether (PEGDME) oligomer (Figure 7) [132]. The device performances were improved due to the enhanced redox couple diffusion. Huo et al. introduced TiO_2 nanoparticles into Poly(vinylidenefluoride-*co*-hexafluoropropylene) P(VDF-HFP) based gel electrolyte. After introducing TiO_2 nanoparticles, the ionic diffusion coefficient of I_3^- in P(VDF-HFP) based gel electrolyte increased six times and could be comparable to that in liquid electrolytes. Ultimately, the best performing device reached the efficiency of 7.18%, even higher than that of liquid electrolyte-based DSSCs. After heating at 60 °C for 1000 h, the best performing device maintains 90% of its initial efficiency [133].

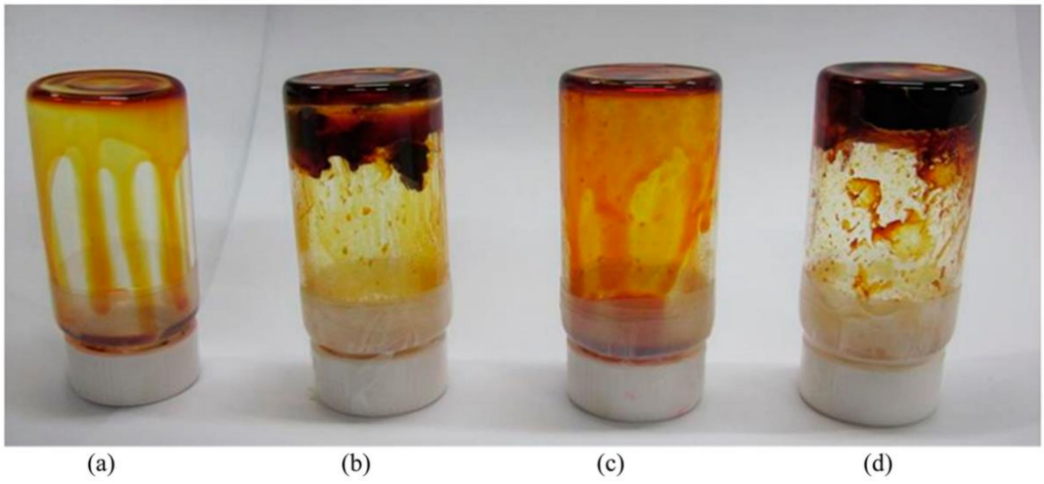

Figure 7. Upside-down vessel containing the PMII/I_2/PEGDME electrolyte with (**a**) none, (**b**) 9 wt % of fumed silica, (**c**) 9 wt % of silica rods, and (**d**)12 wt % of silica rods, respectively (reproduced from Reference [132] with permission, copyright American Chemical Society, 2014).

Table 5. Photovoltaic performance parameters of DSSCs based on the different polymer electrolyte.

Electrolyte System	J_{SC} (mA cm^{-2})	V_{OC} (V)	*FF* (%)	η (%)	Ref.
Epichlomer-16, 0.3 g elastomer, 25 mL acetone, 0.03 g NaI	4.20	0.82	47	1.6	[118]
1.4 g polyacrylonitrile, 10 g ethylene carbonate, 5 mL propylene carbonate, 5 mL acetonitrile, 1.5 g NaI, 0.1 g I_2	3.40	0.58	67.0	4.40	[119]
17.5 wt % Poly(acrylonitrile-*co*-styrene), 0.5 M *N*-methyl pyridine iodide, 0.05 M iodine, ethylene carbonate:propylene carbonate	7.82	0.708	56.0	3.10	[120]
40 wt % PEG, 60 wt % PC, 0.65M KI, 0.065 M I_2,	14.89	0.73	66.45	7.22	[121]
10 wt % PEO, 0.1 M LiI, 0.1 M I_2, 0.6 M DMPII, 0.45 M NMBI in MePN	9.13	0.76	68.1	4.72	[122]
2 wt % PS, 0.6 M butylmethylimidazolium iodide, 0.03 M I_2, 0.1 M guanidinium thiocyanate, 0.5 M *t*BP in acetonitrile/valeronitrile (85:15, *V*/*V*)	15.30	0.77	64.0	7.54	[123]
N-methyl pyridine iodide, iodine, γ-BL, Triton X-100, 0.5 mL glacial acetic acid, 2 mL titanium isopropoxide	5.63	0.635	51.4	3.06	[124]
PAA-PEG, 0.5 M NaI, 0.05 M I_2, 0.4 M pyridine, 30 vol % NMP, 70 vol % GBL	15.28	0.661	62.4	6.30	[126]
PAA-PEG, 1.0 M NaI, 0.15 M I_2, 0.4 M pyridine, 30 vol % NMP, 70 vol % GBL	11.41	0.724	63.5	5.25	[126]
PEG:LiI/I_2 + 15 wt % PEGDA	—	—	—	4.18	[127]
PPDD, 0.5 M iodide, 0–0.5 M inorganic salt, 0.5 M NMBI	17.10	0.70	64.0	7.72	[128]
PAA-PEG 20,000, 0.5 M NaI, 0.05M I_2, 30 vol % NMP, 70 vol % GBL, 0.4 M PY, DMF	12.55	0.735	66.1	6.10	[129]
PEO-TiO_2(I^-/I_3^-)	7.20	0.664	58.0	4.20	[130]
PEO/TiO_2/I^-/I_3^-	2.05	0.67	39.0	0.96	[131]
9 wt % SiO_2 nanorod/PMII/I_2/PEGDME	12.0	0.621	62.8	4.68	[132]
10 wt % P (VDF-HFP), 0.6 M DMPII, 0.1 M LiI, 0.1 M I_2, 0.45 M NMBI	14.746	0.621	62.5	5.72	[133]

2.5. Polymers in All-Weather DSSC

In previous research, Tang et al. have reported the graphene based all-weather dye-sensitized solar cell, which harvests the energy not only from the sunlight, but also from rain [134–137]. The basic principle of all-weather solar cells is forming the π-electron|cation double-layer pseudocapacitance at graphene/raindrop interface. And then, the delocalized π-electron migrate along the penetrating pathways of raindrop forward at spreading process and backward at shrinking periods, finishing the charging and discharging process [135]. In conductive polymers, the conjugated structure between the heteroatom (N or S) and the benzene ring can form the graphene-like π-electron distribution system. In this sense, the conductive polymer can substitute the graphene in the all-weather dye-sensitized solar cell. At the interface between PANI and raindrop, the charge interactions occur, which can meanwhile harvest the energy from sunlight and rain [138]. The hybridized solar cell with PANI yield an efficiency of 6.5%.

3. Polymers in Perovskite Solar Cells

The perovskite refers to the compounds with ABX_3 structure, where A refers to a cation like formamidinium (FA^+), methylammonium (MA^+), or caesium (Cs^+), B represents the metal cation like Pb^{2+} or Sn^{2+}, and the X is halogen ions (F^-, Cl^-, and Br^-). The organic-inorganic hybrid perovskite solar cell is triggering a revolution in the field of photovoltaic cells due to its booming performances [139–142]. The device architecture of PSCs can be divided into two distinct types: Regular n–i–p PSCs and inverted p–i–n PSCs. The schematic diagram of perovskite solar cell is shown in Figure 8 [143–147]: The ambipolar transmission characteristics of perovskite determine that it can generate electrons and holes after being excited by light. The electrons are excited to the CB of perovskite, while the holes left in the valence band (VB). The excited electrons in CB of perovskite transfer to the FTO substrate

through the CB of the electron transport layer (ETL), and then flow through the external circuit. At the same time, holes in the VB of perovskite diffuse to perovskite/HTL interface, and then injected into the HTL and reached the metal electrode to complete the closed loop. The carriers recombination happens through the radiative or non-radiative transition. The back electron transfer at the interface of TiO_2/perovskite and the back hole transfer at the interface of HTL/perovskite occur. The incomplete coverage could lead to the charge recombination at the interface of TiO_2/HTL. Hence, the components materials, the crystallization morphologies of perovskite films, and the interfacial properties all will exert direct influences on device efficiency and stability.

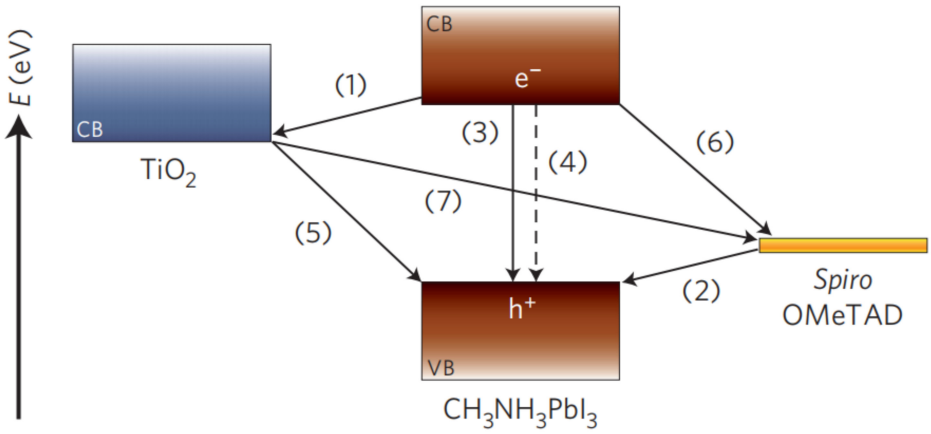

Figure 8. Schematic diagram of energy levels arrangement in perovskite solar cells (reproduced from Reference [145] with permission, copyright Nature Publishing Group, 2014).

3.1. Polymers in Perovskite Morphology Regulations

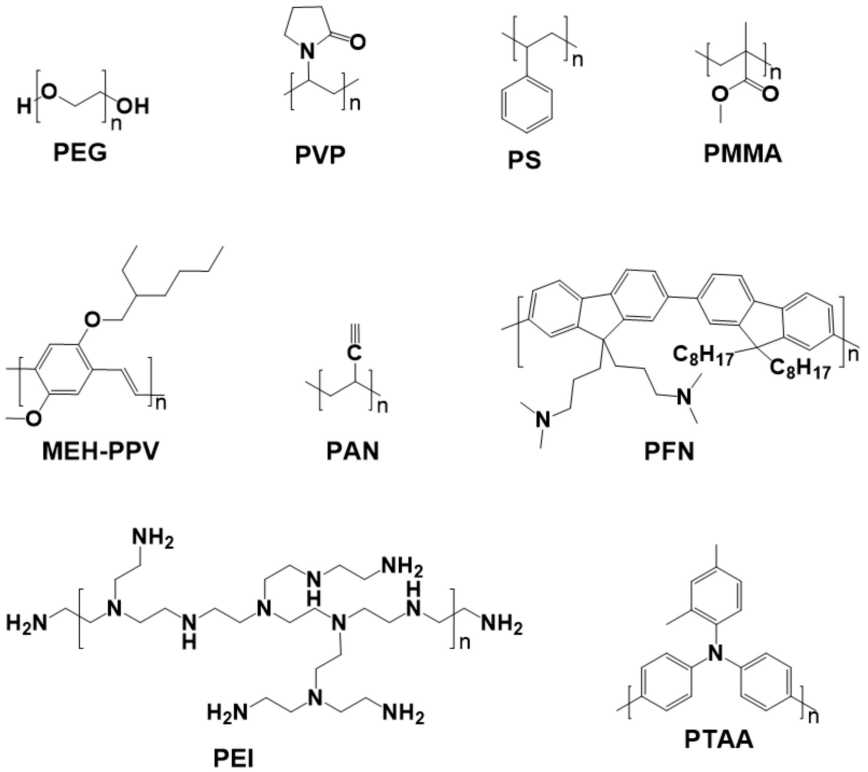

Figure 9. Molecular structures of common polymer additives.

The intrinsic properties of organic-inorganic hybrid perovskite can be used to explain the rapidly increased efficiency, such as high absorption coefficient, direct and tunable bandgap, high carrier mobility and long carrier lifetimes [148,149]. The crystallization morphology of the perovskite film is another imperative consideration for high efficiency device, because it can exert the fatal influences on light absorption and carrier transportation dynamics [150]. Nevertheless, the rapid reaction between precursors introduce the ineluctable defects, which damage the device performances by accelerating the carriers recombination [151,152]. Therefore, more and more endeavors have been dedicated to reduce the defects and pinholes and to obtain the compact and even perovskite films. The additive engineering has been proved to be efficient in facilitating nucleation, regulating crystal growth, and enhancing device performances [153]. The existing additives include the follow aspects: (1) Solvent additives [153]; (2) fullerene additives [154]; (3) metal halide salt additives [155,156]; (4) inorganic acid additives [157,158]; (5) organic halide salt additives [157,158]; (6) nanoparticles additives [159]; (7) polymer additives [160,161]; and (8) other additives [162,163].

The obvious ionic nature of perovskite decides that perovskite can generate multiple chemical interaction with different functional groups [161]: The empty orbitals from Pb or Sn make it possible to form the coordination interaction with molecules containing hetero atoms [164]; The H atom in MA^+ or FA^+ can form hydrogen bonds with atoms with high electronegativity and small radius, such as "F, O, and N atoms" [165]. Polymers are a kind of macromolecule organics with various functional groups and hetero atoms [166]. Therefore, the polymers can be used as the additives to enhance the interaction between grains in perovskite films, enhancing the device stability further [165]. Besides, the good solubility of polymers in polar solvent reduces the contact angle, which guarantees the spread of precursor solution and the even coverage of perovskite film [167]. These unique features make the polymers can be used as additives to improve the crystallization morphology and device performances. Figure 9 shows the molecular structures of common polymers additives, involving poly(ethyleneglycol) (PEG), polyetherimide (PEI), polyvinylpyrrolidone (PVP), polystyrene (PS), poly(methyl methacrylate) (PMMA), 2,4-dimethyl-poly(triarylamine) (PTAA), Poly(2-ethyl-2-oxazoline) (PEOXA), poly[2-methoxy-5-(2-ethylhexyloxy)-1,4-phenylenevinylene] (MEH-PPV), poly-acrylonitrile (PAN), and poly[(9,9-bis(3'-(*N*,*N*-dimethylamino)-propyl)-2,7-fluorene)-alt-2,7-(9,9-dioctyl-fluorene)] (PFN), etc. [164–175]. Figure 10 presents the influences of several polymer additives on the surficial and cross-sectional morphology of perovskite films. It is obvious that theses polymer additives improve the coverage and reduce the pinholes, and are therefore conducive to reduce recombination and enhance device performance.

Masi et al. investigated the effects of following several polymers on the crystallization morphology of perovskite films systematically, such as MEH-PPV, PFN, PMMA, PS, and PTAA [157]. The results revealed that the films based on NEH-PPV and PFN additives are helpful to obtain the smooth morphology with small and uniformly distributed domains. The PMMA, PS, and PTAA based films present obvious bundle/island-like morphology, which can be attributed to the phase separations caused by high aggregation state. Chang et al. fabricated $CH_3NH_3PbI_{3-x}Cl_x$ perovskite with improved coverage by incorporating the PEG additive into the precursor solution [170]. The PEG is beneficial to spread out the precursor solution, to retard the crystallization rate, and to reduce the pinholes in grain boundaries [170]. The perovskite film based on 1 wt % PEG obtained an enhanced efficiency of 13.20%. Apart from the roles of improving the coverage and slowing down the crystallization rate, Zhao et al. found that PEG also served as the scaffold for perovskite film due to its three-dimensional network structure (Figure 11a–d) [171]. The device based on PEG scaffold structure retained 65% of its initial efficiency after aging for 300 h in highly humid condition with RH of 70%. Besides, the color of perovskite films and the device performances based the PEG scaffold can be self-healed quickly after removing the vapor spray (Figure 11e) [171]. The enhanced stability and self-healing effect of the PEG scaffold-based device results from that the hydrogen bonding interaction between perovskite and PEG and the excellent hygroscopicity of the PEG. Guo et al. fabricated the semitransparent

solar cells assembled with stable cubic phase perovskite film by utilizing the PVP additive [172]. The PVP additive can enhance device efficiency and stability by reducing surface roughness, increasing shunting resistance, forming hydrogen bonds, and improving moisture resistance. Ultimately, 3.0 wt % PVP-doped perovkite solar cells obtain the enhanced efficiency than that of reference devices. Bi et al. also fabricate the efficient and stable perovskite solar cells by using the PMMA as template to regular the nucleation and growth of perovskite films [173]. Owing to forming the intermediate adduct with PbI_2, the PMMA can adjust the preferred orientation of nuclei to minimize the total Gibbs free energy. The PMMA template based-device obtained the best efficiency of 21.3%.

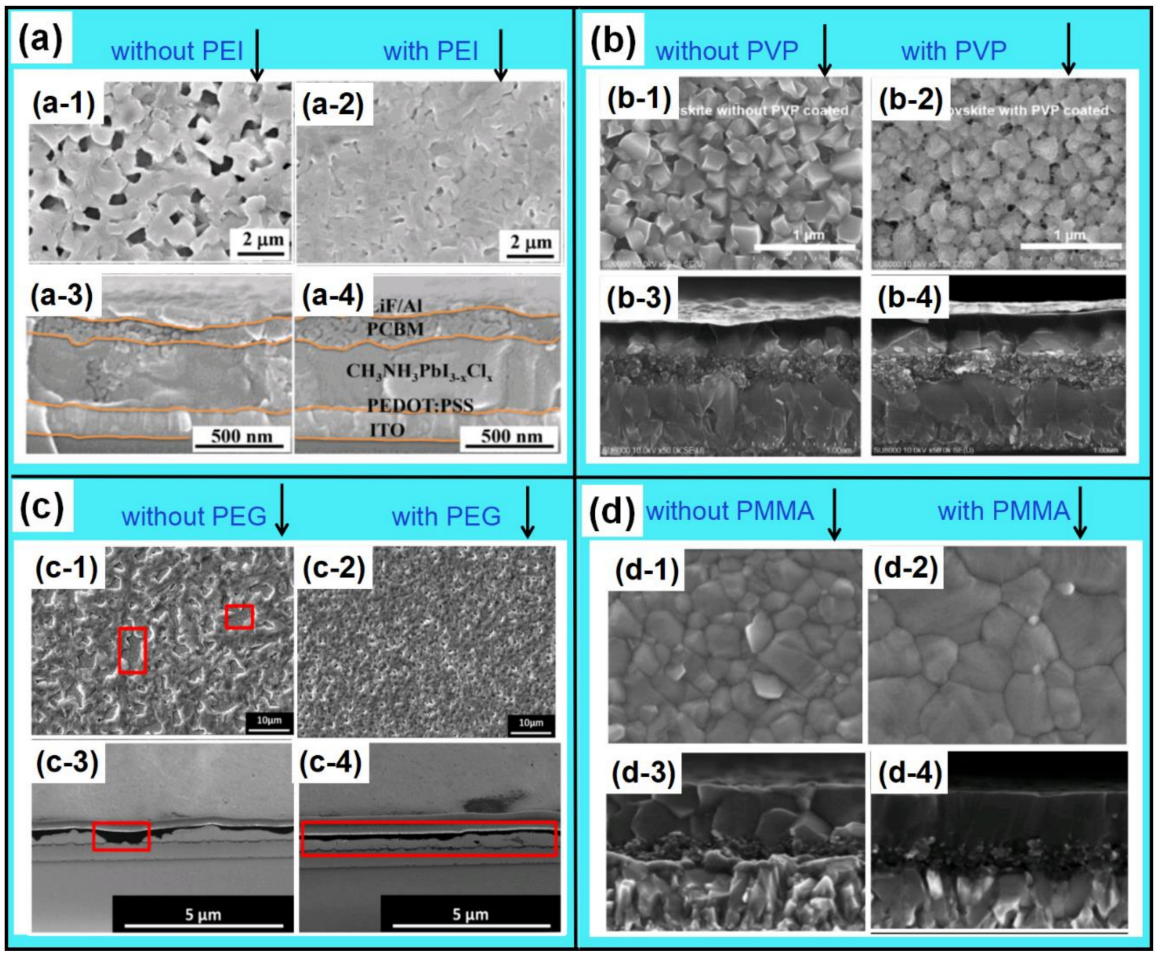

Figure 10. Comparisons of FESEM images and corresponding cross-sectional FESEM images of perovskite films with and without several different polymer additives: (**a**) PEI (reproduced from Reference [165] with permission, copyright The Royal Society of Chemistry, 2016), (**b**) PVP (reproduced from Reference [166] with permission, copyright Wiley, 2017), (**c**) PEG (reproduced from Reference [170] with permission, copyright American Chemical Society, 2015), and (**d**) PMMA (reproduced from Reference [173] with permission, copyright Nature Publishing Group, 2014), respectively.

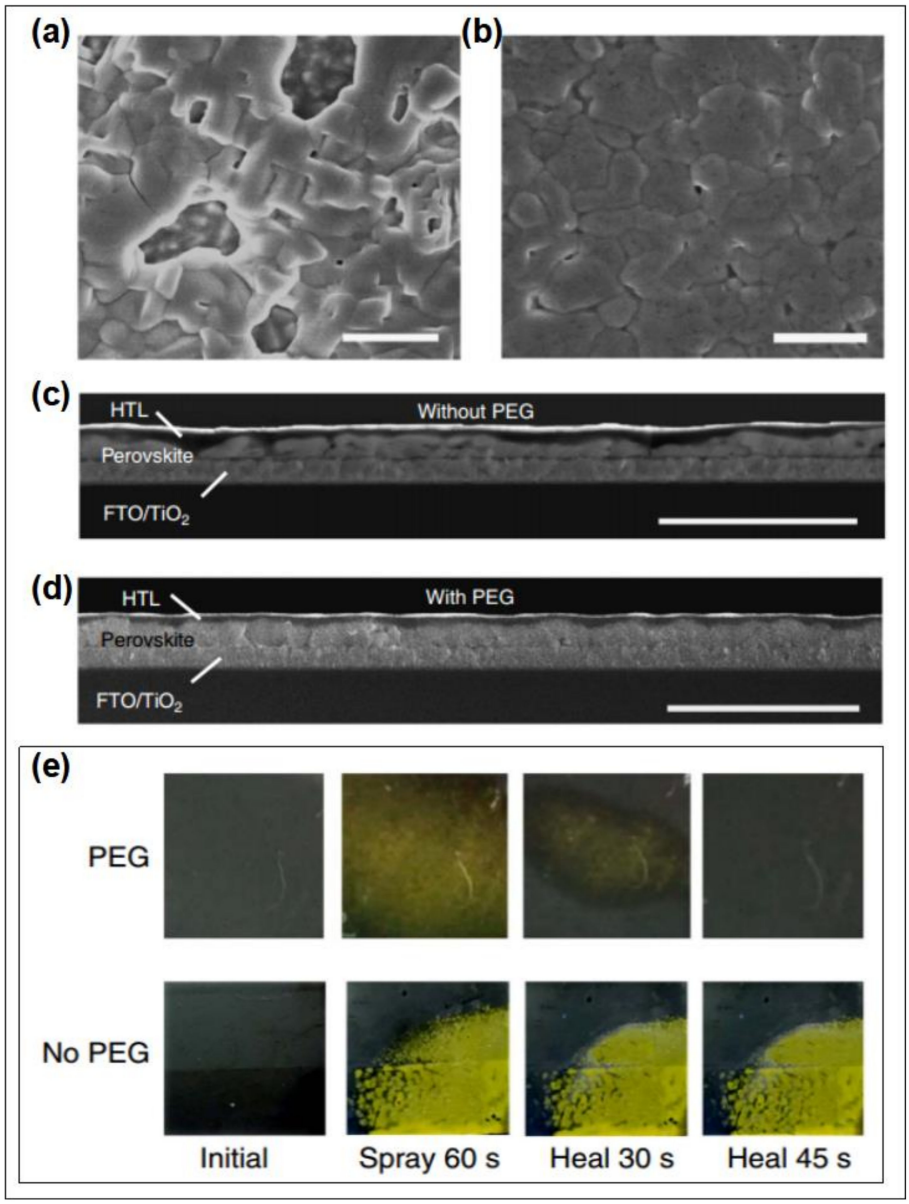

Figure 11. Comparisons of FESEM and corresponding cross-sectional FESEM images of perovskite films: (**a**,**c**) With PEG, and (**b**,**d**) without PEG, respectively. (**e**) Photographs of the color change of perovskite films with and without PEG after water-spraying for 60 s and kept in ambient air for 45 s (reproduced from Reference [171] with permission, copyright Nature Publishing Group, 2016).

3.2. Polymers as Hole Transport Layers (HTLs)

The electron injection process from the CB of perovskite to the CB of TiO_2 finishes within 200 fs. The hole injection process from the VB of perovskite to that of HTL occurs in 0.75 ps. The results indicated that the recombination risks at the interface of perovskite/HTL are higher than that of perovskite/ETL [176]. Therefore, looking for an efficient hole transfer material is imperative and significant to the rapid electron-hole separation and transmission, and excellent device performances. The commonly used materials for HTL include three categories: Organic small molecule HTL, inorganic HTL, and polymeric HTL [177].

The Spiro-OMeTAD is one of the most typical organic small molecule HTL. However, the device based on pure Spiro-OMeTAD HTL always presents poor performances, which can be attributed to its intrinsic low hole-mobility (4×10^{-5} $cm^2 \cdot V^{-1} \cdot S^{-1}$) [178–180]. The lithium bis(trifluoromethanesul-fonyl)imide (Li-TFSI) and tertbutylpyridine (*t*BP) can be used as the efficient

additives to increase the conductivity of Spiro-OMeTAD by an order of magnitude [180–182]. However, the easy deliquescence of Li-TFSI decides the decayed device efficiency and poor environmental stability [141,183]. Besides, the long oxidization process and the cumbersome synthesis and purification processes also greatly increase the cost of Spiro-OMeTAD [183]. Above mentioned drawbacks all limit the long-term utilization of Spiro-OMeTAD HTL. The inorganic HTLs (such as NiMgLiO, CuSCN, and CuI) present the easy fabrication, high hole mobility, and excellent stability [184–186]. However, the solvent used for the deposition of inorganic HTLs might dissolve perovskite partially, damaging perovskite film structure and compromising device performances further [142,176,187,188]. Compared with the organic small molecule HTLs and inorganic HTLs, the conjugated polymer HTLs possess high stability and solution operability, which have been evident from the OPVs. Figure 12 and Table 6 present the common chemical structures of polymer HTLs and corresponding device performance parameters. The common polymer HTLs include the following several types:

3.2.1. Triarylamine-Based Polymers as HTLs

The first PSC device with polymer HTL is based on the (poly-[bis(4-phenyl)(2,4,6-trimethylphenyl)amine] (PTAA). This groundbreaking work illustrates that the triarylamine-based molecular is one kind of the most effective hole transfer materials, which also motivates the research about the HTLs based on the triarylamine and corresponding derivatives. Heo et al. constituted the PTAA HTL based device and yielded the efficiency of 9.0%, even higher than that based on Spiro-OMeTAD (8.4%) [189]. The strong interaction between PTAA and perovskite and its high hole mobility (1×10^{-2}~1×10^{-3} $cm^2 \cdot V^{-1} \cdot S^{-1}$) are the main reasons for excellent efficiency [189]. Even though the device efficiency based the PTAA HTL is higher than that based on Spiro-OMeTAD, the device efficiency of 9.0% is relatively low. However, Yang et al. fabricated the device with the structure of FTO/(bl/mp-TiO_2)/perovskite/PTAA/Au and obtained the efficiency of 20.2%, which fully affirms the possibility and potential of PTAA as HTL [190]. Qin. et al. fabricated the 2,4-dimethoy-phenyl substituted triarylamine oligomer S197 and applied it as the HTL of PSC [191]. The excellent solubility, suitable energy level, high hole mobility equip the S197 as a feasible HTL. This point was evident from its corresponding device efficiency of 12.00% with illumination of 99.6 $mW \cdot cm^{-2}$, higher than that based PTAA (11.50%). Therefore, it is significant to design and synthesis the novel derivatives based on the triarylamine and to employ them as the hole transfer materials.

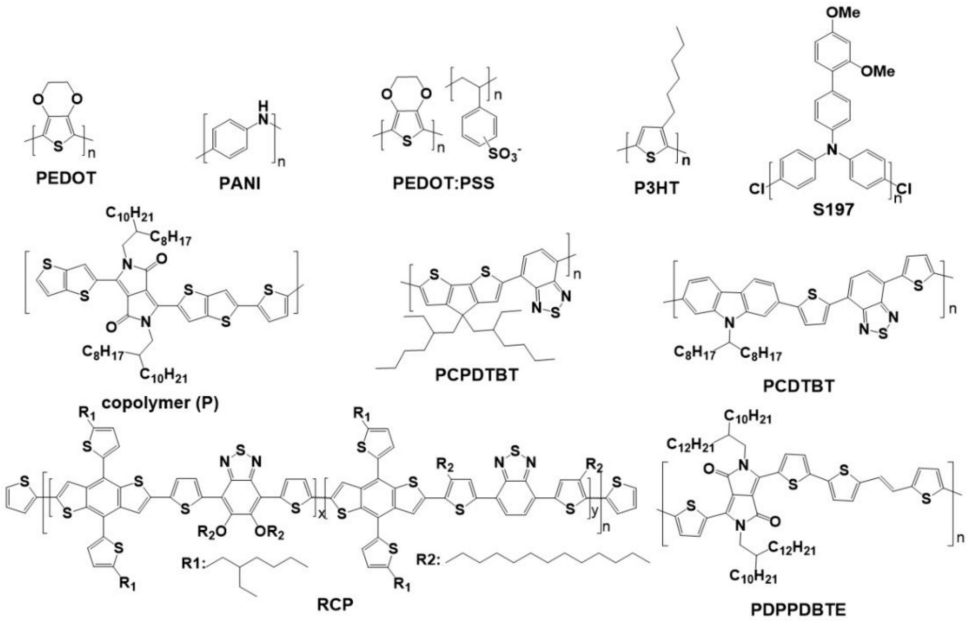

Figure 12. Chemical structures of polymers used to discuss the hole transport materials.

3.2.2. Conductive Polymers as HTLs

The conductive polymers have been extensively used as the hole transfer materials in PSCs due to their easy fabrication process, low cost and p-type semiconductor nature. PEDOT:PSS is one of the most successful HTLs, especially in the inverted planar PSCs [192]. The transparency, good film forming properties, high work function (~5.2 eV), and low processing temperature of PEDOT:PSS enable it to serve as the effective HTL [192,193], especially in the flexible PSCs. Chen et al. fabricated the device with ITO/PEDOT:PSS/$FASnI_3$/Spiro-OMeTAD/Au architecture and obtained the efficiency of 7.05% [194]. Bai et al. compared the performances of PSCs based on several different HTLs. The results illustrate that the PEDOT:PSS based device obtained the lower efficiency than others, which can be explained by the higher working function of PEDOT:PSS than the counterparts [195]. Zhang et al. obtained the efficiency of 17.16% by using the device with ITO/PEDOT:PSS/perovskite/PCBM/Bphen/Al [196]. By controlling the morphologies of perovskite and regulating the interfaces, the PEDOT:PSS-based PSCs can obtain the excellent efficiencies, even higher than 18% [197]. However, the stability of PEDOT:PSS based device is inferior, which results from the hydrophilic and acidic characteristics of PEDOT:PSS [197–200]. The PEDOT:PSS could results in the corrosion of substrates, especially for the ITO substrate [198–201]. Moreover, the devices based on the PEDOT:PSS HTL always achieved the low V_{OC} due to the unmatched work function between perovskite ionization potential and PEDOT:PSS [199,202]. In order to solve these problems, the Nafion was integrated with PEDOT:PSS to fabricate a novel HTL by Ma et al. [202]. The PEDOT:PSS:Nafion increased the transmittance, enhanced the conductivity and hole mobility, improved the V_{OC} to 1.02 V by reducing the work function, and enhanced the environmental stability due to the hydrophobic nature of Nafion. Eventually, the PSC based on the Nafion-modified HTL yield the efficiency of 16.72%, 23.76% higher than that based on the pure PEDOT:PSS (13.51%).

Besides, the PANI has been employed as the HTL in solid-state DSSCs. Inspired by this, Xiao et al. fabricated the PANI HTL with brachyplast structure by using two-step cyclic voltammetry approaches [203]. The PANI-based PSC delivers an efficiency of 7.34% and remains 91.42% of its initial efficiency after 1000 h. As an analogy, the electropolymerized PEDOT electrode was used to assemble the bifacial PSCs, where the PEDOT was used as HTL [204]. Ultimately, the PEDOT HTL-based bifacial PSC device achieved the front and rear efficiencies of 12.33% and 11.78%, respectively. Above all, research illustrates that the conductive polymers are one types of promising hole transfer materials.

3.2.3. Poly-3-hexylthiophene Based Polymers and Composites as HTLs

Poly-3-hexylthiophene (P3HT) was widely used as the HTL due to its low cost and doping-free features. However, the initial efficiency (<7%) of P3HT HTL based PSC can be ascribed to that the flat P3HT molecular is easy to cause the substantial charge recombination due to the close contact between the thiophene units and perovskite [205]. Besides, the device based on the P3HT HTL obtains the low V_{OC}, which can be attributed to the high occupied molecular orbital (HOMO) energy level of P3HT [206]. Zhu et al. synthesized diketopyrrolopyrrole-based copolymer (P) and employed it as a hole transporting layer of $CH_3NH_3PbI_3$ based device [207]. Owing to the hole mobility of P copolymer (1.95 $cm^2 \cdot V^{-1} \cdot S^{-1}$) is higher than that of P3HT (3×10^{-4} $cm^2 \cdot V^{-1} \cdot S^{-1}$), the device-based P HTL obtained the efficiency of 10.80%, higher than that based P3HT HTL (6.62%). However, the device efficiency based on the P3HT is always lower than that based Li-doped Spiro-OMeTAD, which can be ascribed to the low hole mobility of P3HT [208].

Many endeavors have been devoted to improve the hole mobility of P3HT, such as adding the additives or fabricating the composites of P3HT/carbon materials [208–211]. Li-TFSI and *t*BP co-doped P3HT, with an enhanced conductivity, improved the device efficiency from pristine 5.7% to 13.7% [208]. The bamboo-like carbon nanotube [209], graphdiyne [210], and SWCNT [211] were used to fabricate the composites with P3HT to improve the hole mobility. The device based on the P3HT/SWCNT-PMMA HTL yielded the efficiency of 15.3% and presented enhanced thermal

stability and humidity stability (Figure 13) [211]. Looking for another derivatives or composites based on P3HT with high hole mobility is imperative.

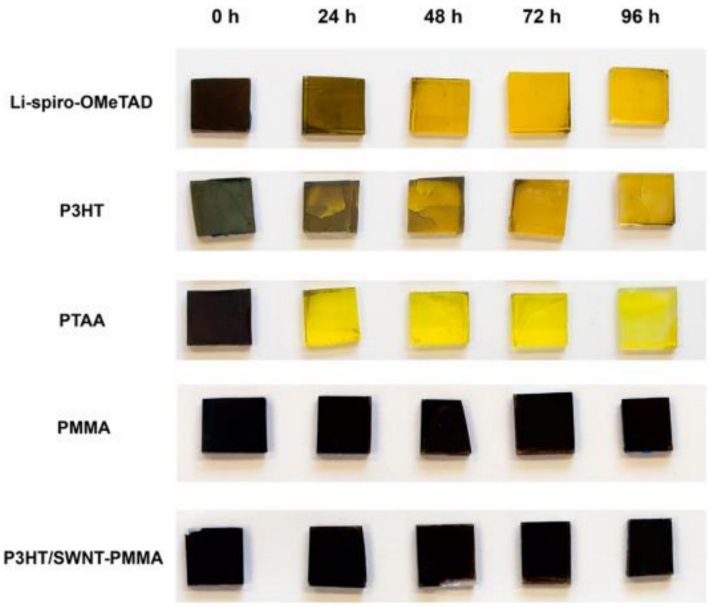

Figure 13. Visible degradation photographs of perovskite films covered with different hole transport materials, including the Li-spiro-OMeTAD, P3HT, PTAA, PMMA and P3HT/SWNT-PMMA (reproduced from Reference [211] with permission, copyright American Chemical Society, 2014).

3.2.4. Other Polymer as HTLs

Heo et al. integrated the several HTLs into PSC devices and studied their effects on the device peformances, such as PTAA, P3HT, poly-[2,1,3-benzothiadiazole-4,7-diyl-[4,4-bis(2-ethyhex-yl)-4H-cyclopenta[2,1-b:3,4-b′]dithiophene-2,6-diyl]] (PCPDTBT), and poly-[[9-(1-octylnonyl)-9H-carbazole-2,7-diyl]-2,5-thiophenediyl-2,1,3-benzothiadiazole-4,7-diyl-2,5-thiophenediyl]) (PCDTBT). The results found that the devices based on the PCPDTBT, PCDTBT, and P3HT HTLs show the efficiency of 5.3%, 4.2% and 6.7%, respectively, lower than that based on the PTAA (9.0%). The lower device efficiencies based on the PCPDTBT, PCDTBT, and P3HT HTLs can be attributed to their lower hole mobility (~1×10^{-4} $cm^2 \cdot V^{-1} \cdot S^{-1}$) than that of PTAA ($1 \times 10^{-2}$~$1 \times 10^{-3}$ $cm^2 \cdot V^{-1} \cdot S^{-1}$) [189]. Kwon et al. synthesized the Poly[2,5-bis(2-decyldodecyl)pyrrolo[3,4-c]pyrrole-1,4(2H,5H)-dione-(E)-1,2-di(2,2′-bithiophen-5-yl)et-hene] (PDPPDBTE) and incorporated it as the HTL, yielding an efficiency of 9.20%, higher than that of Spiro-OMeTAD (7.6%) [212]. The higher device efficiency based on the PDPPDBTE HTL can be ascribed to the higher hole mobility (0.32 $cm^2 \cdot V^{-1} \cdot S^{-1}$) than that of Spiro-OMeTAD (~10^{-4} $cm^2 \cdot V^{-1} \cdot S^{-1}$). After aging 1000 h under a 20% humidity atmosphere, the PDPPDBTE HTL based device remains 91.3% of its initial efficiency [212]. Kim et al. fabricated a novel polymeric HTM RCP based on the benzo[1,2-b:4,5:b′]dithiophene (BDT) and 2,1,3-benzothiadiazole (BT) [213]. As comparision, the P-OR, P-R, and Spiro-OMeTAD were also used as the HTLs. The PSC device based on the RCP HTL obtains the efficiency of 17.3%, higher than that based P-OR (2.6%), P-R (1.9%), and Spiro-OMeTAD (3.8%). The device efficiency can be explained from the highest hole mobility of RCP (3.09×10^{-3} $cm^2 \cdot V^{-1} \cdot S^{-1}$). After adding the Li-TFSI and *t*BP additives (ADDs), the device based on the HTL obtained the reduced efficiency of 16.5%. The device based on the RCP almost remains its pristine efficiency after aging 1400 h at 75% humidity. This research broadens our horizons of designing and selecting the novel hole transfer materials [213].

Table 6. Photovoltaic performances parameters of PSCs based on the different polymer HTLs.

Device Structure of PSCs with Polymer HTLs	J_{SC} (mA·cm^{-2})	V_{OC} (V)	*FF* (%)	η (%)	Ref.
FTO/mp-TiO_2/$CH_3NH_3PbI_3$/PTAA/Au	16.40	0.90	61.4	9.0	[189]
FTO/bl-TiO_2/mp-TiO_2/FAPbI3-based perovskite/PTAA/Au	24.70	1.06	77.5	20.2	[190]
FTO/TiO_2/$CH_3NH_3PbI_3$/S197/Au	17.60	0.967	70.0	12.0	[191]
ITO/PEDOT:PSS/FASnI3/C_{60}/BCP/Cu	24.87	0.45	0.63	7.05	[194]
ITO/PEDOT:PSS/$CH_3NH_3PbI_3$/PC_{61}BM/Au/LiF	19.35	0.80	73.0	11.90	[195]
ITO/PEDOT:PSS/$CH_3NH_3PbI_3$/PCBM/Bphen/Al	22.53	0.983	77.3	17.16	[196]
FTO/(PEDOT:PSS):Nafion/$CH_3NH_3PbI_3$/PCBM/Al	22.17	1.02	73.47	16.68	[202]
FTO/TiO_2/$CH_3NH_3PbI_3$/PANI	14.48	0.78	65.0	7.34	[203]
FTO/TiO_2/$CH_3NH_3PbI_3$/PPEDOT	20.08	0.89	69.0	12.33	[204]
FTO/Mp-TiO_2/$CH_3NH_3PbI_3$/P3HT/Au	12.60	0.73	73.2	6.70	[189]
FTO/TiO_2/$CH_3NH_3PbBr_3$/P3HT/Au	1.13	0.84	54.0	0.52	[206]
ITO/perovskite/P3HT/MoO_3/Ag	17.90	0.87	66.0	10.80	[207]
ITO/perovskite/P/MoO_3/Ag	13.80	0.81	52.0	5.62	[207]
FTO/bl-TiO_2/$CH_3NH_3PbI_3$/P3HT+Li-TFSI+tBP/Au	20.10	0.92	74.0	13.70	[208]
FTO/Mp-TiO_2/$CH_3NH_3PbI_3$/P3HT+BCN/Au	17.75	0.83	49.0	7.60	[209]
FTO/Mp-TiO_2/$CH_3NH_3PbI_3$/P3HT-graphdiyne/Au	19.63	0.939	71.5	13.17	[210]
FTO/Mp-TiO_2/$CH_3NH_3PbI_3$/P3HT/SWCNT-PMMA/Au	22.71	1.02	66.0	15.30	[211]
FTO/Mp-TiO_2/$CH_3NH_3PbI_3$/PCPDTBT/Au	10.30	0.77	66.7	5.30	[189]
FTO/Mp-TiO_2/$CH_3NH_3PbI_3$/PCDTBT/Au	10.50	0.92	43.7	4.20	[189]
FTO/bl-TiO_2/mp-TiO_2/$CH_3NH_3PbI_3$/PDPPDBTE/Au	14.40	0.8553	74.9	9.20	[212]
FTO/bl-SnO2/$CH_3NH_3PbI_3$/RCP/Au	21.9	1.08	75.0	17.30	[213]

3.3. Polymers as Electron Transport Layers (ETLs)

In perovskite solar cells, the ETL plays the roles of collecting electron from perovskite films and transporting it into the external circuit. Therefore, an ideal ETL material should have high electron mobilities and matched energy level with perovskite. In regular n-i-p architecture, the common ETL materials are TiO_2 and ZnO. In inverted p-i-n architecture, fullerene and corresponding derivatives have been used as the most common ETL materials. However, the temporal stability of fullerene and corresponding derivatives is also poor, which can be evident from the morphological changes upon recrystallization [214]. Therefore, the research about ETL is still in a beginning stage, especially for the non-fullerene ETL. In recent years, the organic polymers have been widely used as the electron transfer materials due to their tunable bandgap, excellent film-forming ability, good electron mobility, and low fabrication cost (Figure 13). The existing organic polymer ETLs are mainly based on the naphthalene diimide (NDI) and perylene diimide (PDI) cores. Naphthalene diimide (NDI) was chosen as it is one of the most explored electron deficient building block for n-type polymers. About NDI-based polymers ETL, Sun et al. developed the PFN-2TNDI ETL by introducing amine functional group to the side chains of fluorine unite of PF-2TNDI. The device assembled with PFN-2TNDI ETL exhibited the PCE of 16.7%, higher than that of PCBM based device (12.9%). The increased device performances comes down to two reasons: The amines on polymer side chains can passivate the surface traps of perovskite; the amines can reduce the work function of metal cathode by forming dipoles at interfaces [215]. Wang et al. have employed poly{[*N*,*N*′-bis(2-octyldodecyl)-1,4,5,8-naphthalenediimide-2,6-diyl]-alt-5,5′(2,2′-bithiophene)}(N2200) as the ETL of perovskite and obtained decent PCE of 8.15%, which is competitive to that of PCBM ETL (8.51%). Moreover, in order to prove the universality of organic polymers as ETL in perovskite solar cells, other polymers PNVT-8 and PNDI2OD-TT have also been tested and achieve the efficiency of 7.13% and 6.11%, respectively [216]. Kim et al. developed another P(NDI2DT-TTCN) copolymer ETL with NDI and dicyano-terthiophene. With the intramolecular interaction between the S–N groups, the dicyano-terthiophene shows a pseudo-planar structure, which decides the good electron transport ability and deep LUMO level of P(NDI2DT-TTCN). The device based on P(NDI2DT-TTCN) showed the PCE of 17.0%, outperforming than that of PCBM ETL-based device (14.3%). This study

also illustrates that P(NDI2DT-TTCN) ETL is hydrophobic and can passivate the surface against ambient conditions. The P(NDI2DT-TTCN) ETL also exhibited better mechanical stability than PCBM-based ETLs in bending cycles, which indicates a better prospect for flexible PSC [217]. Guo et al. designed a series of PDI-based polymer PX-PDIs ETL with different X copolymerized units: Vinylene (V), thiophene (T), selenophene (Se), dibenzosilole (DBS), and cyclopentadithiophene (CPDT). The device based on PX-PDI ETL shows the highest PCE of 10.14%, which can be attributed to that PV-PDI ETL shows the deeper LUMO energy level and better planar structure than other PX-PDI (X = T, Se, DBS, and CPDT) [218]. All this research provide valuable design guidelines for devising new polymeric ETLs.

3.4. Polymer as the Interlayer

The perovskite solar cells present the layer-by-layer structure. The invert p-i-n architecture includes the FTO/HTL, HTL/perovskite, perovskite grain/grain, perovskite/ETL, ETL/Au, and Au/atmosphere interfaces. Charge extraction and separation occur at the interfaces, which could suffer from the recombination due to any possible interfacial defects. Therefore, interfacial chemical interaction is decisive factor for the device performances. The interface engineering has been used as a common method to regulate the morphologies of perovskite films, reduce the defects, and improve the device performances. The polymer interfacial modification has been regarded as one of the most effective methods of interface engineering (Figure 14). At the HTL/perovskite interface, Malinkiewicz et al. introduce the poly(*N*,*N*′-bis(4-butylphenyl)-*N*,*N*′-bis(phenyl)benzidine) (polyTPD) layer, which can transfer hole and block electron due to its LUMO is closer to the conductive bandgap energy [219]. Lin et al. introduced the DPP-DTT, PCDTBT, P3HT, and PCPDTBT layers at the PEDOT:PSS/perovskite interface. The perovskite films grown on PCDTBT shows the highest crystallinity intensity and device efficiency than others due to its matched energy level [220]. Wen et al. used the insulating PS to treat the initial perovskite films and formed the tunneling junction between the perovskite film and hole transfer film. The PS films is capable of accelerating the separation of photo-generated electrons and holes by selectively transfer hole while blocking electrons, improving the device efficiency from 15.90% to 17.80% [221]. At the interfaces between perovskite grains, Wang et al. used the chlorobenezene solution of PMMA to treat the as-prepared perovskite films, which can passivate the surface trap states in perovskite films and suppress the recombination [222]. It is worth stressing that manipulating the perovskite films with PMMA is beneficial to enhance the device stability by protecting the perovskite films from oxygen and moisture. At the perovskite/ETL interface, Wang et al. chose the PS, Teflon, and polyvinylidene-trifluoroethylene copolymer (PVDF-TrFE) as the tunneling materials. The tunneling materials allow electron transfer from perovskite to C60 ETL and blocks the holes. The device based on the PS interlayer given the highest PCE of 20.3%, higher than that of control devices (16.9%) [223]. At the ETL/metal interface, polyethyleneimine (PEIE) and poly[3-(6-trimethylammoniumhexyl) thiophene] (P_3TMAHT) create surface dipole. The durface dipole make the work function of Ag decrease from original 4.70 to 3.97 eV (PEIE) and 4.13 eV (P_3TMAHT), and the corresponding PCE increase from original 8.53% to 12.01% (PEIE) and 11.28 (P_3TMAHT), respectively [224]. These studies provide a guideline for using the polymers to realize the interface regulation and modification.

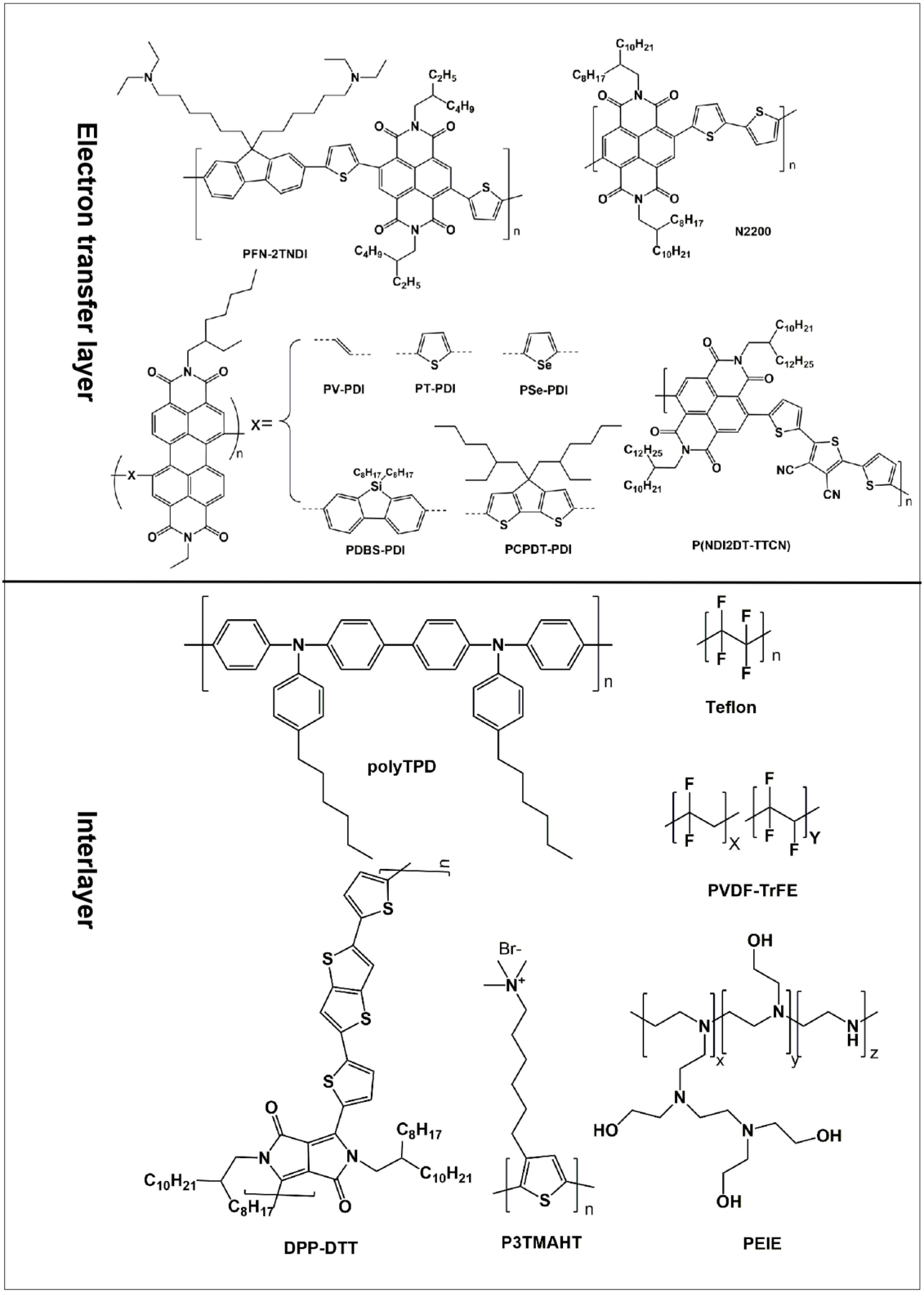

Figure 14. Chemical structures of polymers used to discuss the electron transport layers and interlayers.

4. Polymers in Organic Photovoltaics

The OPVs have attracted much attention since the 1950s. The first breakthrough of OPVs is the development from the initial single-layer architectures to donor-acceptor (D-A) bilayer architectures [11,225–227]. The second breakthrough of OPVs is the development from

the planar heterojunction (PHJ) to bulk heterojunction (BJH) [228]. Compared to the PHJ, the BHJ configuration can improve the charge separation greatly, because the bicontinuous networks ensure the increased D/A interface, where the charge separation happens effectively [11,226,228]. The OPV is composed of the sandwich-like ITO anode/organic polymer active layer (D-A)/metal cathode. As shown in Figure 15, the organic polymer active layer produces the excitons under the excitation of light; The excitons diffuse in the bulk of the active layer; Once reaching to the interface of donor/acceptor, the excitons were separated into the electrons and holes, which were then transferred to the two electrodes to produce the photocurrent [228–231]. Therefore, the design and synthesis of D-A based active layers are imperative, but significant for the excitons separation and device performance. The traditional acceptors include the fullerene and its derivatives due to high electron affinity, long electron diffusion length, and rapid charge separation [11,232], such as C_{60}, $PC_{60}BM$, and $PC_{70}BM$. However, the selection range of polymer donors is wider than that of acceptors. The ideal polymer donors should satisfy the following conditions: With the medium or low bandgap; with high carriers mobility; with matched energy levels; with good solubility [233–236]. Figure 16 and Table 7 show the molecular structures of selected polymer donor materials and the photovoltaic performances parameters of corresponding devices.

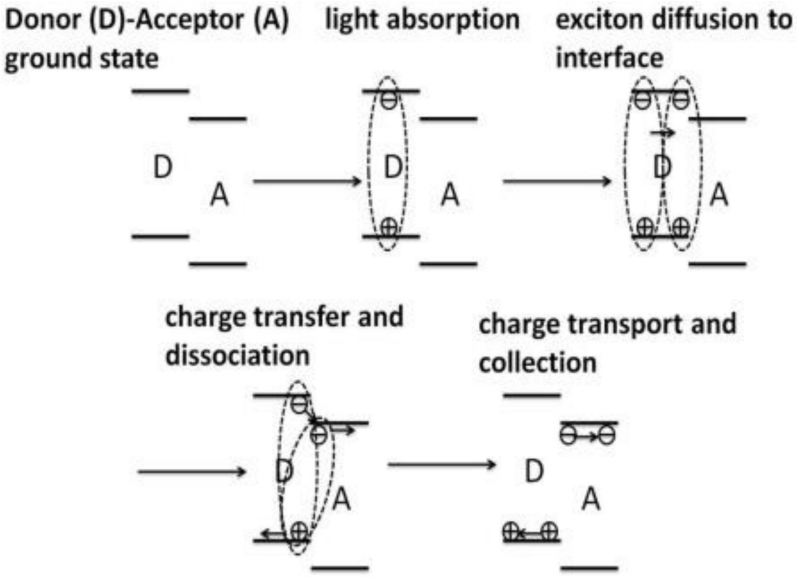

Figure 15. Mechanism diagram of organic photovoltaics (reproduced from Reference [230] with permission, copyright Wiley, 2014).

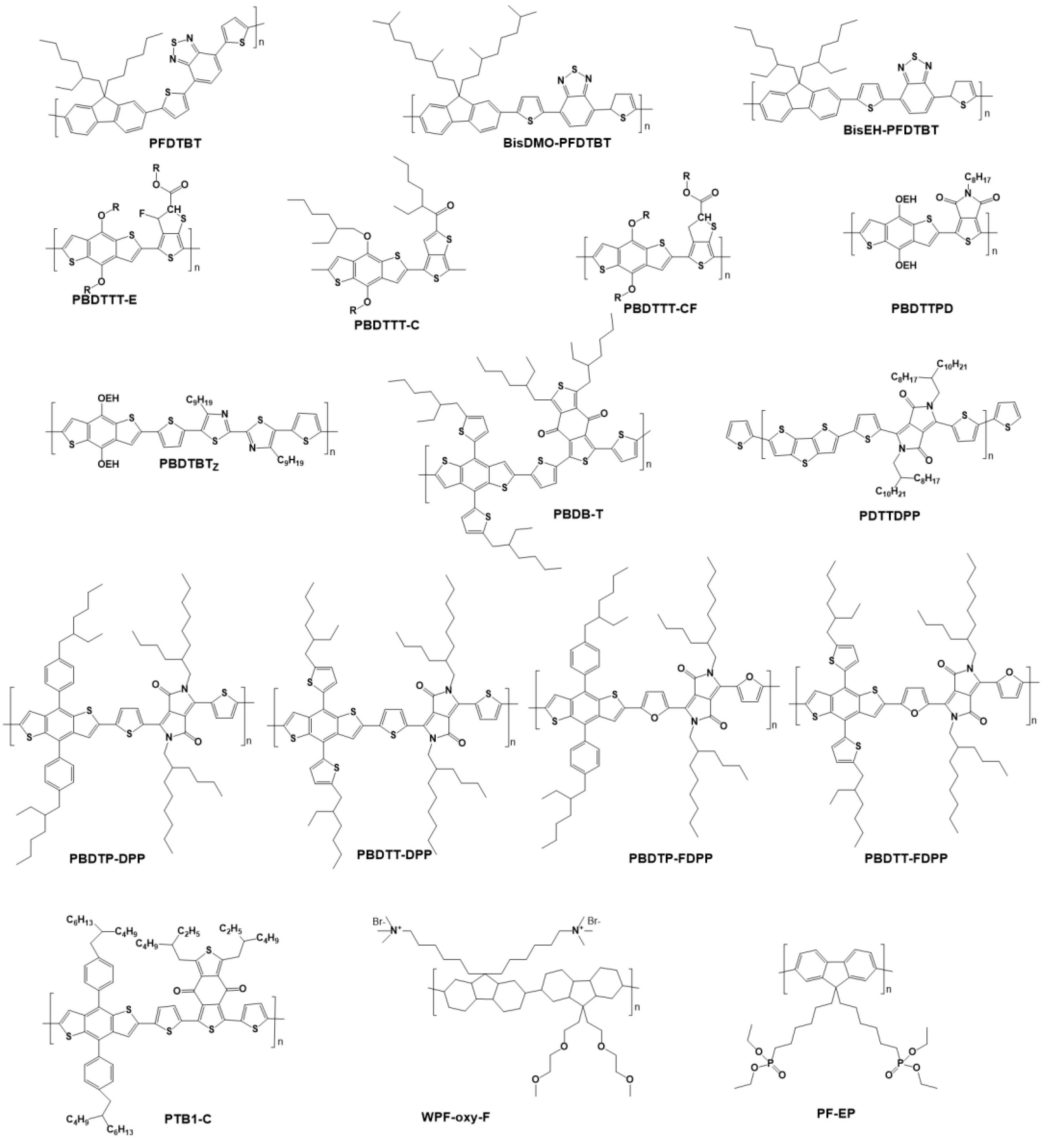

Figure 16. Molecular structures of materials for photoactive layers.

4.1. Polymers in Binary OPVs

4.1.1. Polymers with Wide Bandgap as the Donor Materials of OPVs

The poly(2-methoxy-5-(2′-ethyl-hexyloxy)-1,4-phenylene vinylene) (MEH-PPV) is the first studied polymer donor. Yu et al. blended the MEH-PPV with PCBM as the active layer of OPV, which presents the device efficiency of 2.9% [237]. However, the low charge mobility and narrow spectral absorption range doubtlessly limit the wide application of MEH-PPV donor.

Poly (thiophene)-based conjugated polymer represented by P3HT has been extensively used as the donor in OPV due to its high carrier mobility, good solubility, and excellent crystallinity and self-assembly performance [238]. Ma et al. fabricated the device with the ITO/PEDOT/P3HT:PCBM/Al architecture and obtained the efficiency of 5.0% [239]. Zhao et al. reported the OPV with the structure of ITO/PEDOT:PSS/P3HT:ICBA(1:1, *w*:*w*)/Ca/Al, achieving the efficiency of 6.5% [240], where the ICBA refers to the Indene-C60. After using the K^+(PFCn6:K^+) as the electron transfer layer (ETL), the device efficiency of ITO/ PEDOT:PSS/P3HT:ICBA/ETL/Ca/Al was enhanced to 7.5% [241]. However, the low efficiencies of P3HT-based devices result from that the large bandgap and energy level arrangement of P3HT affect the light-harvesting and V_{OC}.

Besides, polyfluorenes is also one of the typical building blocks for donor due to its excellent features [242–244]: Polyfluorenes possess good charge transport performance; Polyfluorenes is facile to self-organize as the anisotropic liquid crystalline structure; Polyfluorenes can act as the electron or hole conductors; The rigid plane structure of polyfluorene equips it low HOMO energy level. Even though the extensive donors in PV are based on the polyfluorenes, the device efficiencies are still low, which can be attributed to its wide bandgap limits the spectral absorption range [245]. Therefore, much research concentrates on developing the polyfluorene copolymers with narrow bandgap and extended absorption [246,247]. Sevensson fabricated poly(2,7-(9-(2′-ethylhexyl)-9-hexyl-fluorene)-alt-5,5-(4′,7′-di-2-thienyl-2′,1′,3′-benzothiadiazole)) (PFDTBT), which presents the wide absorption and enhanced efficiency of 2.2 % in OPV [244]. The low photocurrent is the major barrier for achieving high efficiencies in this case. In order to solve this problem, Chen and Hou et al. grafted the different side chains on the PFDTBT build block to synthesize poly{[2,7-(9,9-bis-(3,7-dimethyl-octyl)-fluorene)]-alt-[5,5-(4,7-di-20-thienyl-2,1,3-Benzoth-adiazole)]} (BisDMO-PFDTBT) andpoly{[2,7-(9,9-bis-(2-ethylhexyl)-fluorene)]-alt-[5,5-(4,7-di-20-thienyl-10-2,1,3 -benzothiadiazole)]} (BisEH-PFDTBT). The side chain modified PFDTBT yielded the highest efficiency of 4.5% by influencing the solubility, π–π stacking of polymers, and bandgap [248].

The donors based the MEH-PPV, P3HT, and polyfluorenes all possess the wide bandgap, which decides the low short current in corresponding devices. Hence, developing the donors with the medium or low bandgap is significant for improving the device efficiency of OPV.

4.1.2. Polymers with Medium Bandgap as the Donor Materials of OPV

The thieo[3,4-b]thiophene-based structures have raised much attentions due to low bandgaps and improved device efficiency of 7~9% [11,249]. The polymers based on the benzodithiophene and thieno[3,4-b]thiophene (PTB7) units were widely used in the OPV and exhibited the excellent properties due to the synergistic roles [250,251]: The quinoidal structure unit results in a narrow bandgap of 1.6 eV; The plane conjugate structure leads to the good hole mobility; The related side chains enable the good solubility; The introduce of fluorine decreases the HOMO energy level, enhancing the V_{OC}. All these advantages make the OPV device with the PTB7/PC_{71}BM active layer (1:1.5, weight ratio) obtained the best efficiency of 6.22%, where the PTB7/PC_{71}BM were dissolved in dichlorobenzene. When using the mixed solvent of chlorobenzene and 1,8-diiodoctane (97%:3% by volume), the morphology becomes even, and the efficiency was enhanced to 7.40% [251]. Chen and Hou et al. grafted the alkyloxy chain and alky side chain on the carbonyl of the thieno[3,4-b] thiophene unit of PBDTTT to synthesis the PBDTTT-E and PBDTTT-C, respectively. The PBDTTT-C was modified with a fluorine atom to form the PBDTTT-CF. The narrow bandgaps of PBDTTT-C, PBDTTT-E, and PBDTTT-CF (about 1.77 eV) ensure the wide spectrum absorption range, leading to the high short current density of 13~15 mA cm^{-2}. Being influenced by the side chain and fluorine atom, the HOMO level of PBDTTT-CF was reduced, which resulted in the high V_{OC}. Consequently, the corresponding device efficiency was enhanced to 7.73% [252].

He et al. adjusted the work function of ITO from 4.7 eV to 4.1 eV by introducing the PFN thin film on the top of ITO (Figure 16). The ohmic contact between modified ITO and photoactive layer was formed, which accelerates the transport and collection of the carriers. As a result, the device with inverted ITO/PFN/PTB7:PC_{71}BM/MoO_3/Al/Ag structure achieved the efficiency of 9.2% [253]. Except the above mentioned electron donors, the polymers based on the indacenodithiophene (IDT), indacenodithieno[3,2-b]thiophene (IDTT), and 1,3-bis(thiophen-2-yl)-5,7-bisethylhexyl) benzo[1,2-c:4,5-c′]dithiophene-4,8-dione (BDD) also have been used as the donor materials with medium bandgap due to their conjugate structure is helpful to improve the hole mobility [254–257].

4.1.3. Polymers with Narrow Bandgap as the Donor Materials of OPV

Generally, the spectral absorption range of PCBM is always concentrated on 350–550 nm. The absorption edge wavelengths of polymers with wide or medium bandgaps are located

at as far as 700 nm. In order to broad the light-harvesting range, more research is devoted to the design the electrons donors with narrow bandgap [257]. The benzo[1,2-b:4,5-b′]dithiophene (BDT) and diketopyrrolopyrrole (DPP) are two representative units for synthesizing the polymer donor materials with narrow bandgap.

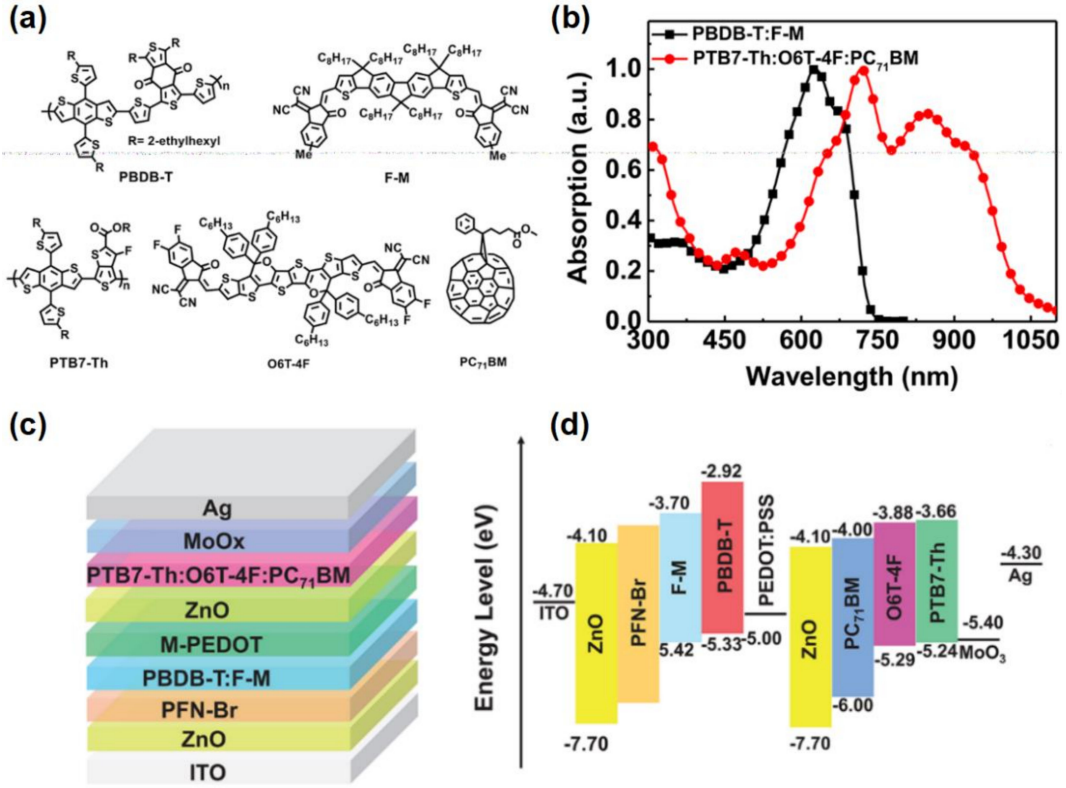

Figure 17. (**a**) Molecular structures of PBDB-T, F-M, PTB7-Th, O6T-4F and $PC_{71}BM$; (**b**) Normalized absorption spectra of PBDB-T:F-M and PTB7-Th:O6T-4F:$PC_{71}BM$ films; (**c**) and (**d**) Device architecture and energy level diagram of the tandem cell, respectively (reproduced from Reference [264] with permission, copyright Science, 2018).

The large planar conjugated structure equips the BDT-based conjugated polymers with the large hole mobility. The small steric hindrance minimizes the impacts of adjacent units on the energy level and bandgap of BDT-based conjugated polymers. These two merits give the priority to use BDT unit to design the ideal donor materials [258]. The BDT unit has been recognized in the OPVs field since the Hou et al. synthesized the eight BDT-based copolymers and explored their photovoltaic properties [258]. The BDT can react with other conjugated units to form the photovoltaic active conjugated polymers, such as the thieno[3,4-b]thiophene (TT) [259], *N*-alkylthieno[3,4-c]pyrrole-4,6-dione (TPD) [260], and bithiazole [261], etc. Cui et al. reported that single-junction OPV baded on PBDB-T:ITCC-M and PBDTTT-E-T:IEICO active layers obtained the efficiency of 10.1% and 8.45%, respectively. The tandem OPV based on above two active layers yielded the best efficiency of 13.8% [262]. Zhao et al. fabricated the poly[(2,6-(4,8-bis(5-(2-ethylhexyl)thiophen-2-yl)-benzo[1,2-b:4,5-b′]dithiophene))-alt-(5,5-(1′,3′-di-2-thienyl-5′,7′-bis(2-ethy-hexyl)benzo[1′,2′-c:4′,5′-c′]dithiophene-4,8-dione))]) (PBDB-T) by modifying the BDT units [263]. The control device based on the PBDB-T:$PC_{71}BM$ yielded an efficiency of 7.45%. After alternating the $PC_{71}BM$ acceptor to 6-3,9-bis(2-methylene-(3-(1,1-dicyanomethylene)-indanone))-5,5,11,11-tetra-kis(4-hexylphenyl)-dithieno[2,3-d:2′,3′-d′]-s-indaceno[1,2-b:5,6-b′]dithiophene) (ITIC) [263]. The OPV based on PBDB-T:ITIC active layer obtained the best efficiency of 11.21% [264]. Meng and Chen et al. recently reported the tandem solar cell based on the ITO/ZnO/PFN-Br/PBDB-T:F-M/M-PEDOT/ZnO/ PTB7-Th:O6T-4F:$PC_{71}BM$/ MoO_x/Ag architecture and presented

the complementary spectrum and matched energy level (Figure 17). The device efficiency reaches to 17.36%, breaking the world record for the efficiency of OPV [264].

The DPP is used to construct the low-bandgap conjugated polymers due to its electron-deficient nature. Dou et al. synthesized a series of conjugated polymers with low bandgap by using the BDT and DPP units [265]: PBDTT-DPP, PBDTP-DPP, PBDTT-FDPP, and PBDTP-DPP. The single layer device and the tandem solar cells based on the PBDTT-DPP:$PC_{71}BM$ obtain the best efficiency of 6.6%, and 8.8%, respectively [265]. Jung et al. reported a novel conjugated polymers PDTTDPP with the bandgap of 1.39 eV using the dithieno[3,2-b:20,30-d]thiophene (DTT) and DPP units. The chloroform solution of PDTTDPP shows the absorption onset at 1015 nm. The absorption even extended to 1055 nm when reducing the thickness of film. The device based the ITO/PEDOT:PSS/PDTTDPP:$PC_{71}BM$ (1:1.5)/LiF/Al obtain the highest efficiency of 6.05% [266]. Hence, designing and synthesising the polymeric donor materials with narrow bandgap are the key to improve the light-harvesting and device efficiency of organic solar cells.

Table 7. Photovoltaic performances parameters of OPVs based on the different polymer donors.

Device Structure of OPVs with Polymer Donors	J_{SC} ($mA{\cdot}cm^{-2}$)	V_{OC} (V)	*FF* (%)	η (%)	Ref.
ITO/PEDOT:PSS/P3HT:ICBA/Ca/Al	10.61	0.84	72.7	6.48	[240]
ITO/PEDOT:PSS/P3HT:ICBA/PFCn6:K^+/Ca/Al	11.65	0.89	72.6	7.50	[241]
ITO/PEDOT:PSS/DiO/Al	3.55	1.01	58.0	2.10	[242]
ITO/PEDOT:PSS/APFO-15:PCBM/LiF/Al	6.00	1.00	63.0	3.70	[247]
ITO/PEDOT:PSS/BisEH-PFDTBT:$PC_{71}BM$/Ca/Al	8.40	0.95	44.0	3.50	[248]
ITO/PEDOT:PSS/BisDMO-PFDTBT:$PC_{71}BM$/Ca/Al	9.10	0.97	51.0	4.50	[248]
ITO/PEDOT:PSS/PTB7:$PC_{71}BM$/Ca/Al	14.50	0.74	68.97	7.40	[251]
ITO/PEDOT:PSS/PBDTTT-E:$PC_{70}BM$/Ca/Al	13.20	0.62	63.0	5.15	[252]
ITO/PEDOT:PSS/PBDTTT-C:$PC_{70}BM$/Ca/Al	14.70	0.70	64.1	6.58	[252]
ITO/PEDOT:PSS/PBDTTT-CF:$PC_{70}BM$/Ca/Al	15.20	0.76	66.9	7.73	[252]
ITO/PEDOT:PSS/PTB7:$PC_{71}BM$/PFN interlayer/Al	15.40	0.759	70.6	8.24	[253]
ITO/PFN interlayer/PTB7:$PC_{71}BM$/MoO_3/Al	17.20	0.740	72.0	9.15	[253]
ITO/PEDOT:PSS/PIDT-DFBT:$PC_{71}BM$/Ca/Al	11.20	0.97	55.0	5.97	[254]
ITO/PEDOT:PSS/PIDTT-DFBT:$PC_{71}BM$/Ca/Al	12.21	0.95	61.0	7.03	[254]
ITO/PEDOT:PSS/PBDTBDD:$PC_{61}BM$/Ca/Al	10.68	0.86	72.27	6.67	[255]
ITO/PEDOT:PSS/PDBT-T1:$PC_{70}BM$/ZrAcac/Al	14.11	0.92	75.0	9.74	[256]
ITO/PEDOT:PSS/PBDTTPD:$PC_{71}BM$/LiF/Al	9.10	0.87	53.8	4.20	[260]
ITO/PEDOT:PSS/PBDTBTz:$PC_{70}BM$/Al	7.84	0.86	57.0	3.82	[261]
ITO/ZnO/PBDB-T:ITIC/MoO_3/Al	16.81	0.899	74.2	11.21	[263]
ITO/ZnO/PFN-Br/PBDB-T:F-M/PEDOT:PSS/ZnO/ PTB7-Th:O6T-4F:$PC_{71}BM$/MoO_3/Ag	14.35	1.642	73.7	17.36	[264]
ITO/PEDOT:PSS/PBDTT-DPP:$PC_{71}BM$/Ca/Al	14.00	0.73	65.0	6.60	[265]
ITO/PEDOT:PSS/PBDTP-DPP:$PC_{71}BM$/Ca/Al	13.60	0.76	60.0	6.20	[265]
ITO/PEDOT:PSS/PBDTT-FDPP:$PC_{71}BM$/Ca/Al	13.80	0.77	55.0	5.80	[265]
ITO/PEDOT:PSS/PBDTP-FDPP:$PC_{71}BM$/Ca/Al	7.42	0.77	59.0	3.30	[265]
ITO/PEDOT:PSS/PDTTDPP:$PC_{71}BM$/LiF/Al	13.70	0.66	66.1	6.05	[265]

4.2. Polymers in Ternary OPVs

The traditional organic solar cells are composed of polymer donors and fullerene-based acceptors. Despite high electron mobilities, fullerene and its derivatives always show large band gap and narrow absorption window, which hinder the further development of OPVs. Therefore, a series of nonfullerene acceptor (NFA) materials have been reported due to its strong light absorption and easily tunable energy levels. Wang et al. introduce a non-fullerene small molecule m-ITIC into PTB7-Th:TQ1 system to fabricate the ternary OPV [267]. The m-ITIC can broaden the spectrum absorption range of OPV, enhancing the resultant device performances further. However, the electron mobilities of NFAs are always low, which affect the device performance directly. Hence, the fullerene acceptor was introduced into the binary polymers donor: Nonfullerene acceptor system to fabricate the ternary

OPV. As the third component, the fullerene can compensate the deficiencies of nonfullerene acceptors. Fu et al. fabricated the ternary OPVs using wide-bandgap PTB1-C as donor and highly conductive $PC_{71}BM$ and narrow-bandgap nonfullerene IT-2F as acceptor [268]. The resultant device obtained increased PCE, which benefits from the increased light harvesting from of IT-2F and enhanced electron transport. Meanwhile, the addition of $PC_{71}BM$ can also suppress the aggregation of IT-2F, reducing the trap density and trap-assisted recombination. When it comes to the ternary OPVs, it is necessary to consider possible and unfavorable large-scale phase separation. Therefore, it is difficult, but imperative, to control the morphology while pursuing high performance. Xie et al. reported that ITIC-2Cl molecules could easily form granular aggregates in the binary blend [269]. After adding 20% ICBA into the blend, the aggregation of ITIC-2Cl reduced, which can be attributed to the amorphous ICBA can disturb intermolecular π–π interactions of ITIC-2Cl. The optimized morphology, low LUMO level, and complementary absorption decide an enhanced PCE of 13.4%.

4.3. Polymers as Buffer Layers of OPV

In organic photovoltaivs, there is a barrier between the active layer and the electrode. The barrier hinders the quick charge transfer, leading to serious charge accumulation at the interfaces. The charge accumulation increase the recombination probability, and attenuate the device performances. Therefore, it is imperative to accelerate the charge separate and transfer efficiency. In order to solve this problem, an interface buffer layer is introduced in the OPVs, including the anode buffer layer and cathode buffer layer. These buffer layers are often established between the active layer and the electrode to form an ohmic contact, which is conducive to the efficient charge extraction and separation. Besides, the buffer layer also can inhibit the possible diffusion and reaction between the active layer and the electrode material. The polymer serves as one kind of the most effective buffer layers. As Table 7 summarized, the PEDOT:PSS has been widely used as the most common anode buffer layer to extract holes, and the corresponding devices achieve enhanced efficiency. Despite the effective charge extraction ability, the acidic PEDOT:PSS solution will cause a certain degree of corrosion of ITO substrate, which in turn reduces the device stability [270]. For the cathode buffer layers, He et al. have applied the alcohol/water-soluble poly[(9,9-bis(3′-(*N*,*N*-diMethylaMino)propyl)-2,7-fluorene)-alt-2,7-(9,9-dioctylfluorene)] (PFN) to extract electron in organic photovoltaics [271]. The OPVs assembled with the PFN cathode buffer layers show enhanced J_{SC}, V_{OC}, and *FF*, which results in a PCE of 8.37% and 6.79% for PTB7 and PCDTBT devices. The positive effect of PFN buffer layer on device performances include: Forming an enhanced built-in potential across the device; and improving the charge separation and transfer efficiency. Na et al. use polyfluorene derivative (WPF-oxy-F) as the interfacial layer between the active layer and metal cathode, which will reduce the metal work function for better electron transport [272]. The PF-EP was introduced as a cathode buffer layer to improve the charge collection efficiency by preventing the metal atoms migrating into the active layer [273].

4.4. Polymer-Based Micro/Nanostructures in the OPVs

The power conversion efficiencies (PCE) of organic photovoltaics (OPV) is still limited and cannot be compared with their inorganic counterpart. The low light trapping efficiency and low charge carrier mobility are the main limitations.

Enhancing light trapping in OPV is important. A thin active layer always leads to optical losses accounting for 40% of total losses [274]. In planar heterojunction structure, the common exciton diffusion length is around 5–10 nm, which decides that the thickness of the active layer is about 10 nm [275]. In bulk heterojunction structure, the thickness of the active layer (about 100~200 nm) is still not enough to absorb and trap light efficiently due to low charge carrier mobilities in most organic materials. Therefore, improving the light trapping within existing OPV architectures is imperative. Apart from developing new materials, another way of improving the light trapping include the uses of textured substrates, noble metal nanoparticles, tandem solar cells, and microlens arrays

(MLA). In the case of textured substrates, the aspect-ratio of textures need to be designed optimally to ensure the conformal coating of the active layers [276]. The unreasonable design will result in shunts and recombination [276]. The noble metal nanoparticles doped active layers employ plasmonic near-field enhancement effects to trap more light. However, the excessive metallic and surface stabilizer on metal could serve as the recombination centers to retard charge transport. In terms of tandem polymer solar cells, the folded structure cause light trapping at high angles and large photocurrent density. Besides, the tandem polymer solar cells also allow multiple bandgap solar cells series or parallel connection. Tvingstedt et al. reported a tandem cell by folding two planar but different cells toward each other, where single cells reflect the non-absorbed light upon another adjacent cell to realize the spectral broadening and light trapping [277]. The ultimate device performances were enhanced. Designing MLA structures on the backside of the transparent conductive substrates has been demonstrated as a universal method to increase light trapping of OPV. This approach couldn't exert influences on the device fabrication processing and active layer morphology. Chen et al. have designed the near-hemispherical MLA of 2 mm diameter, which shows the higher ability to refract incoming light than a pure-hemispherical shape [278]. The diameter of this MLA is close to visible light wavelength. This property decides that the near-hemispherical MLA can not only reduce surface reflections, but also can utilize optical interference to enhance light intensity inside the active layer. Ultimately, for the P3HT:PCBM active layer system, the device with near-hemispherical MLA obtained the increased absorption, absolute external quantum efficiency (EQE), and PCE by 4.3%. For the PCDTBT:$PC_{70}BM$ active layer system, near-hemispherical MLA increases the absorption, EQE and PCE by 10.0%. All of these enhancements can be attributed to the increased light path and absorption, as well as diffraction induced enhanced light intensity. Tvingstedt et al. also studied and demonstrated the principle of MLAs trap the light in detail [279]. The MLAs can make the light display strong directional asymmetric transmission, realizing the recycle of reflected photons. Peer et al. design the device based on dual photonic crystals, where polymer MLAs on the glass was coupled with a photonic-plasmonic crystal at the metal cathode on the back of the cell. The MLAs focuses light on the periodic nanostructure, realizing strong light diffraction. The surface plasmon and waveguiding effect of photonic-plasmonic crystal enhance long wavelength absorption. The joint efforts of MLAs and photonic-plasmonic crystal result in absorption enhancement of 49% and photocurrent enhancement of 58% [280]. In addition to the OPV, the MLAs have also been extended to improve the device performances of perovskite and organic light emitting diodes [281].

Improving the charge carrier mobility and reducing the recombination are imperative to enhance the device efficiency of OPV. For a common device with BJH structure, the electron donor and acceptor interspersed randomly in the active layer, which always leads to the discontinuous electron transport pathways. Hence, the internal interfacial area must be large enough to create the continuous pathways for charge separation and transport. In order to solve this problem, He et al. constitute the nanostructured polymer heterojunctions of composition and morphology in the active layer through a double nanoimprinting process [282]. The devices based on double-imprinted poly((9,9-dioctylfluorene)-2,7-diyl-alt-[4,7-bis(3-hexylthien-5-yl)-2,1,3-benzothia-diazole]-2′,2″-diyl) (F8TBT)/poly(3-hexylthiophene) (P3HT) films obtained a PCE of 1.9%, higher than that of planar F8TBT/P3HT (0.36%). The enhanced device performance can be attributed to ordered structure in the active layer can enhance the separation of electron-hole pairs and improve carrier mobilities further. Wiedemann et al. fabricate similar PCBM/P3HT bilayer devices with controlled nanostructured interfaces by combining nanoimprinting and lamination techniques, which presented a higher PCE (0.05%) than that of common bilayer structured device (0.03%) [283]. This method is also suitable for any other polymer combinations.

5. Summary and Outlook

The polymers have been widely used in the photovoltaic fields, including the DSSC, PSC, and OPV.

In DSSC, the polymers not only can be used as the flexible substrates, but also the pore- and film-forming agents of photoanode films; Besides, the conductive polymers and corresponding composites can be used to fabricate the platinum-free counter electrode materials due to their high catalytic activity; The long chain structure and containing functional groups also decide the polymers can be used to solidify the liquid electrolyte and form the quasi-solid-state electrolytes. The applications of polymers in flexible PAN or PET substrates, mesoporous TiO_2 photoanodes preparation, polymer gel electrolyte and platinum-free counter electrodes are extensive and mature. The conductivity of quasi-solid-state polymer electrolytes is still low. Hence, improving the conductivity of quasi-solid-state electrolytes is still challenging, which can be realized by adjusting the ratios of polymers and liquid electrolyte.

In PSC, the polymers can be used to facilitate the nucleation, regulate the crystallization of perovskite films, and enhance the device stability by forming various interactions with the perovskite films. The polymers can also be employed as the hole transfer materials due to their high hole mobility. It is challenging to design the novel polymers hole transport materials with high hole mobility and appropriate energy level arrangement. Applying the polymers to fabricate the long-term stable PSC devices is another bottleneck. However, these two aspects are not only imperative to improve the carrier separation efficiency and the final device efficiency, but also important for the practical application.

In OPV, the polymers are widely used as the active layers to influence the light harvesting efficiency and device performances. The key to realizing the high-efficient OPV is to design the novel polymer donors with narrow bandgap and appropriate energy level arrangement. Besides, it is promising to select the polymers with complementary spectrum absorption range to fabricate the ternary or tandem OPVs.

Author Contributions: W.H. and Y.X. conceived the structure of the manuscript and wrote the manuscript; G.H. and J.-Y.L. supervised the writing and reviewed the manuscript.

Funding: This research was funded by the National Natural Science Foundation of China (61504076, 61804091, 21574076, and U1510121), Scientific and Technological Innovation Programs of Higher Education Institutions in Shanxi (2014103), the Fund for Shanxi "1331 Project" Key Innovation Research Team, and Doctoral education innovation project (2017BY007) in Shanxi Province, and Ministry of Science and Technology Taiwan (MOST 107-2221-E-036-007-MY3).

Conflicts of Interest: The authors declare no conflict of interest.

References

1. Sovacool, B.K. National context derives concrens. *Nat. Energy* **2018**. [CrossRef]
2. Quirin, S.; Jeff, T.; Tony, S.; Alexandra, W.; Oliver, M. Energy alternatives: Electricity without carbon. *Nature* **2008**, *454*, 816–823. [CrossRef]
3. Green, M.A. The path to 25% silicon solar cell efficiency: History of silicon cell evolution. *Prog. Photovolt Res. Appl.* **2009**, *17*, 183–189. [CrossRef]
4. Razykov, T.M.; Ferekides, C.S.; Morel, D.; Stefanakos, E.; Ullal, H.S.; Upadhyaya, H.M. Solar photovoltaic electricity: Current status and future prospects. *Sol. Energy* **2011**, *85*, 1580–1608. [CrossRef]
5. Hubbard, S.M.; Cress, C.D.; Bailey, C.G.; Raffaelle, R.P.; Bailey, S.G.; Wilt, D.M. Effect of strain compensation on quantum dot enhanced GaAs solar cells. *Appl. Phys. Lett.* **2008**, *92*, 123512. [CrossRef]
6. Chirilă, A.; Buecheler, S.; Pianezzi, F.; Bloesch, P.; Gretener, C.; Uh, A.R.; Fella, C.; Kranz, L.; Perrenoud, J.; Seyrling, S.; et al. Highly efficient Cu(In,Ga)Se_2 solar cells grown on flexible polymer films. *Nat. Mater.* **2011**, *10*, 857–861. [CrossRef] [PubMed]
7. Li, W.; Yang, R.L.; Wang, D.L. CdTe solar cell performance under high-intensity light irradiance. *Sol. Energy Mater. Sol. Cells* **2014**, *123*, 249–254. [CrossRef]
8. Andersen, T.R.; Dam, H.F.; Hosel, M.; Helgesen, M.; Carle, J.E.; Larsen-Olsen, T.T.; Gevorgyan, S.A.; Andreasen, J.W.; Adams, J.; Li, N.; et al. Scalable, ambient atmosphere roll-to-roll manufacture of encapsulated large area, flexible organic tandem solar cell modules. *Energy Environ. Sci.* **2014**, *7*, 2925–2933. [CrossRef]

9. Freitag, M.; Daniel, Q.; Pazoki, M.; Sveinbjornsson, K.; Zhang, J.B.; Sun, L.C.; Hagfeldt, A.; Boschloo, G. High-efficiency dye-sensitized solar cells with molecular copper phenanthroline as solid hole conductor. *Energy Environ. Sci.* **2015**, *8*, 2634–2637. [CrossRef]
10. Wu, Y.Z.; Xie, F.X.; Chen, H.; Yang, X.D.; Su, H.M.; Cai, M.L.; Zhou, Z.M.; Noda, T.; Han, L.Y. Thermally stable $MAPbI_3$ perovskite solar cells with efficiency of 19.19% and area over 1 cm^2 achieved by additive engineering. *Adv. Mater.* **2017**, *29*, 1701073. [CrossRef]
11. Ragoussi, M.E.; Torres, T. New generation solar cells: Concepts, trends and perspectives. *Chem. Commun.* **2015**, *51*, 3957–3972. [CrossRef]
12. Xiao, Y.M.; Wu, J.H.; Lin, J.Y.; Yue, G.T.; Lin, J.M.; Huang, M.L.; Lan, Z.; Fan, L.Q. A dual function of high performance counter-electrode for stable quasi-solid-state dye-sensitized solar cells. *J. Power Sources* **2013**, *241*, 373–378. [CrossRef]
13. Kojima, A.; Teshima, K.; Shirai, Y.; Miyasaka, T. Organometal halide perovskites as visible-light sensitizers for photovoltaic cells. *J. Am. Chem. Soc.* **2009**, *131*, 6050–6051. [CrossRef] [PubMed]
14. Xie, F.X.; Chen, C.C.; Wu, Y.Z.; Li, X.; Cai, M.L.; Liu, X.; Yang, X.D.; Han, L.Y. Vertical recrystallization for highly efficient and stable formamidinium-based inverted-structure perovskite solar cells. *Energy Environ. Sci.* **2017**, *10*, 1942–1949. [CrossRef]
15. Research Cell Efficiency Records. Available online: https://www.nrel.gov/pv/assets/images/efficiency-chart-20180716.jpg (accessed on 10 January 2019).
16. Cichosz, S.; Masek, A.; Zaborski, M. Polymer-based sensors: A review. *Polym. Test.* **2018**, *67*, 342–348. [CrossRef]
17. Lee, M.M.; Teeuscher, J.; Miyasaka, T.; Murakami, T.N.; Snaith, H.J. Efficient hybrid solar cells based on meso-superstructured organometal halide perovskites. *Science* **2012**, *338*, 643–647. [CrossRef] [PubMed]
18. Wei, J.; Li, H.; Zhao, Y.C.; Zhou, W.K.; Fu, R.; Leprince-Wang, Y.; Yu, D.P.; Zhao, Q. Suppressed hysteresis and improved stability in perovskite solar cells with conductive organic network. *Nano Energy* **2016**, *26*, 139–147. [CrossRef]
19. Stephan, A.M. Review on gel polymer electrolytes for lithium batteries. *Eur. Polym. J.* **2006**, *42*, 21–42. [CrossRef]
20. Gao, C.L.; Dong, H.Z.; Bao, X.C.; Zhang, Y.C.; Saparbaev, A.; Yu, L.Y.; Wen, S.G.; Yang, R.Q.; Dong, L.F. Additive engineering to improve efficiency and stability of inverted planar perovskite solar cells. *J. Mater. Chem. C* **2018**, *6*, 8234–8241. [CrossRef]
21. Xue, Q.F.; Hu, Z.C.; Liu, J.; Lin, J.H.; Sun, C.; Chen, Z.M.; Duan, C.H.; Wang, J.; Liao, C.; Lau, W.M.; et al. Highly efficient fullerene/perovskite planar heterojunction solar cells via cathode modification with an amino-functionalized polymer interlayer. *J. Mater. Chem. A* **2014**, *2*, 19598–19603. [CrossRef]
22. Chang, C.M.; Li, W.B.; Guo, X.; Guo, B.; Ye, C.N.; Su, W.Y.; Fan, Q.P.; Zhang, M.J. A narrow-bandgap donor polymer for highly efficient as-cast non-fullerene polymer solar cells with a high open circuit voltage. *Organ. Electron.* **2018**, *58*, 82–87. [CrossRef]
23. Scharber, M.C.; Sariciftci, N.S. Efficiency of bulk-heterojunction organic solar cells. *Prog. Polym. Sci.* **2013**, *38*, 1929–1940. [CrossRef] [PubMed]
24. Gao, J.; Yang, Y.; Zhang, Z.; Yan, J.Y.; Lin, Z.H.; Guo, X.Y. Bifacial quasi-solid-state dye-sensitized solar cells with poly (vinyl pyrrolidone)/polyaniline transparent counter electrode. *Nano Energy* **2016**, *26*, 123–130. [CrossRef]
25. Lee, C.P.; Lin, C.A.; Wei, T.C.; Tsai, M.L.; Meng, Y.; Li, C.T.; Huo, K.C.; Wu, C.I.; Lau, S.P.; He, J.H. Economical low-light photovoltaics by using the Pt-free dye-sensitized solar cell with graphene dot/PEDOT:PSS counter electrodes. *Nano Energy* **2015**, *18*, 109–117. [CrossRef]
26. Jeon, S.S.; Kim, C.; Lee, T.H.; Lee, Y.W.; Do, K.; Ko, J.; Im, S.S. Camphorsulfonic acid-doped polyaniline transparent counter electrode for dye-sensitized solar cells. *J. Phys. Chem. C* **2012**, *116*, 22743–22748. [CrossRef]
27. O'Regan, B.; Grätzel, M. A low-cost, high-efficiency solar cell based on dye-sensitized colloidal TiO_2 films. *Nature* **1991**, *353*, 737–740. [CrossRef]
28. Han, L.Y.; Islam, A.; Chen, H.; Malapaka, C.; Chiranjeevi, B.; Zhang, S.F.; Yang, X.D.; Yanagida, M. High-efficiency dye-sensitized solar cell with a novel co-adsorbent. *Energy Environ. Sci.* **2012**, *5*, 6057–6060. [CrossRef]

29. Wu, J.H.; Lan, Z.; Lin, J.M.; Huang, M.L.; Huang, Y.F.; Fan, L.Q.; Luo, G.G. Electrolytes in dye-sensitized solar cells. *Chem. Rev.* **2015**, *115*, 2136–2173. [CrossRef]
30. Hagfeldt, A.; Grätzel, M. Light-induced redox reactions in nanocrystalline systems. *Chem. Rev.* **1995**, *95*, 49–68. [CrossRef]
31. Hagfeldt, A.; Boschloo, G.; Sun, L.C.; Kloo, L.; Pettersson, H. Dye-sensitized solar cells. *Chem. Rev.* **2010**, *110*, 6595–6663. [CrossRef]
32. Wu, J.H.; Lan, Z.; Lin, J.M.; Huang, M.L.; Huang, Y.F.; Fan, L.Q.; Luo, G.G.; Lin, Y.; Xie, Y.M.; Wei, Y.L. Counter electrodes in dye-sensitized solar cells. *Chem. Soc. Rev.* **2017**, *46*, 5975–6023. [CrossRef] [PubMed]
33. Freitag, M.; Boschloo, G. The revival of dye-sensitized solar cells. *Curr. Opin. Electrochem.* **2017**, *2*, 111–119. [CrossRef]
34. Zardetto, V.; Brown, T.M.; Reale, A.; Carlo, A.D. Substrates for flexible electronics: A practical investigation on the electrical, film flexibility, optical, temperature, and solvent resistance properties. *J. Polym. Sci. Part B Polym. Phys.* **2011**, *49*, 638–648. [CrossRef]
35. Agarkar, S.A.; Dhas, V.V.; Muduli, S.; Ogale, S.B. Dye sensitized solar cell (DSSC) by a novel fully room temperature process: A solar paint for smart windows and flexible substrates. *RSC Adv.* **2012**, *2*, 11645–11649. [CrossRef]
36. Qin, Q.; Zhang, R. A novel conical structure of polyaniline nanotubes synthesized on ITO-PET conducting substrate by electrochemical method. *Electrochim. Acta* **2013**, *89*, 726–731. [CrossRef]
37. Miettunen, K.; Halme, J.; Lund, P. Metallic and plastic dye solar cells. *Wires Energy Environ.* **2012**, *2*, 104–120. [CrossRef]
38. Zardetto, V.; Giacomo, F.D.; Garcia-Alonso, D.; Keuning, W.; Creatore, M.; Mazzuca, C.; Reale, A.; Carlo, A.D.; Brown, T.M. Fully plastic dye solar cell devices by low-temperature UV-irradiation of both the mesoporous TiO_2 photo- and platinized counter-electrodes. *Adv. Energy Mater.* **2013**, *3*, 1292–1298. [CrossRef]
39. Yun, S.N.; Freitas, J.N.; Nogueira, A.F.; Wang, Y.M.; Ahmad, S.; Wang, Z.S. Dye-sensitized solar cells employing polymers. *Prog. Polym. Sci.* **2016**, *59*, 1–40. [CrossRef]
40. Wu, W.Q.; Xu, Y.F.; Rao, H.S.; Feng, H.L.; Su, C.Y.; Kuang, D.B. Constructing 3D branched nanowire coated macroporous metal oxide electrodes with homogeneous or heterogeneous compositions for efficient solar cells. *Angew. Chem. Int. Ed.* **2014**, *53*, 4816–4821. [CrossRef]
41. Mor, G.K.; Shankar, K.; Paulose, M.; Varghese, O.K.; Grimes, C.A. Use of highly-ordered TiO_2 nanotube arrays in dye-sensitized solar cells. *Nano Lett.* **2006**, *6*, 215–218. [CrossRef]
42. Wang, J.; Lin, Z.Q. Dye-sensitized TiO_2 nanotube solar cells with markedly enhanced performance via rational surface engineering. *Chem. Mater.* **2010**, *22*, 579–584. [CrossRef]
43. Jang, Y.H.; Xin, X.K.; Byun, M.; Jang, Y.J.; Lin, Z.Q.; Kim, D.H. An unconventional route to high-efficiency dye-sensitized solar cells via embedding graphitic thin films into TiO_2 nanoparticle photoanode. *Nano Lett.* **2012**, *12*, 479–485. [CrossRef] [PubMed]
44. Jung, H.G.; Kang, Y.S.; Sun, Y.K. Anatase TiO_2 spheres with high surface area and mesoporous structure via a hydrothermal process for dye-sensitized solar cells. *Electrochim. Acta* **2010**, *55*, 4637–4641. [CrossRef]
45. Low, F.W.; Lai, C.W. Recent developments of graphene-TiO_2 composite nanomaterials as efficient photoelectrodes in dye-sensitized solar cells: A review. *Renew. Sustain. Energ. Rev.* **2018**, *82*, 103–125. [CrossRef]
46. Benkstein, K.D.; Kopidakis, N.; Lagemaat, J.; Frank, A.J. Influence of the percolation network geometry on electron transport in dye-sensitized titanium dioxide solar cells. *J. Phys. Chem. B* **2003**, *107*, 7759–7767. [CrossRef]
47. Hou, W.J.; Xiao, Y.M.; Han, G.Y.; Zhou, H.H.; Chang, Y.Z.; Zhang, Y. Preparation of mesoporous titanium dioxide anode by a film- and pore-forming agent for the dye-sensitized solar cell. *Mater. Res. Bull.* **2016**, *76*, 140–146. [CrossRef]
48. Yun, T.K.; Park, S.S.; Kim, D.; Hwang, Y.K.; Huh, S.; Bae, J.Y.; Won, Y.S. Pore-size effect on photovoltaic performance of dye-sensitized solar cells composed of mesoporous anatase-titania. *J. Power Sources* **2011**, *196*, 3678–3682. [CrossRef]
49. Pandikumar, A.; Lim, S.P.; Jayabal, S.; Huang, N.M.; Lim, H.N.; Ramaraj, R. Titania@gold plasmonic nanoarchitectures: An ideal photoanode for dye-sensitized solar cells. *Renew. Sustain. Energ. Rev.* **2016**, *60*, 408–420. [CrossRef]

50. Menon, H.; Gopakumar, G.; Nair, V.S.; Nair, S.V.; Shanmugam, M. 2D-layered MoS_2-incorporated TiO_2-nanofiber-based dye-sensitized solar cells. *Chemistryselect* **2018**, *3*, 5801–5807. [CrossRef]
51. Kokubo, H.; Ding, B.; Naka, T.; Tsuchihira, H.; Shiratori, S. Multi-core cable-like TiO_2 nanofibrous membranes for dye-sensitized solar cells. *Nanotechnology* **2007**, *18*, 165604. [CrossRef]
52. Joshi, P.; Zhang, L.F.; Davoux, D.; Zhu, Z.T.; Galipeau, D.; Fong, H. Composite of TiO_2 nanofibers and nanoparticles for dye-sensitized solar cells with significantly improved efficiency. *Energy Environ. Sci.* **2010**, *3*, 1507–1510. [CrossRef]
53. He, G.F.; Wang, X.X.; Xi, M.; Zheng, F.; Zhu, Z.T.; Fong, H. Fabrication and evaluation of dye-sensitized solar cells with photoanodes based on electrospun TiO_2 nanotubes. *Mater. Lett.* **2013**, *106*, 115–118. [CrossRef]
54. Briscoe, J.; Dunn, S. The future of using earth-abundant elements in counter electrodes for dye-sensitized solar cells. *Adv. Mater.* **2016**, *28*, 3802–3813. [CrossRef] [PubMed]
55. Hou, W.J.; Xiao, Y.M.; Han, G.Y. An interconnected ternary MIn_2S_4 (M=Fe, Co, Ni) thiospinel nanosheet array: A type of efficient platinum-free counter electrode for dye-sensitized solar cells. *Angew. Chem. Int. Ed.* **2017**, *56*, 9146–9150. [CrossRef] [PubMed]
56. Li, L.; Zhang, X.; Wang, D.Y.; Zhang, W.M.; Li, X.W.; Zhao, X.H.; Zhang, Q.H.; Gu, L.; Yu, Z.; Wu, M.X. Electrospinning synthesis of high performance carbon nanofiber coated flower-like MoS_2 nanosheets for dye-sensitized solar cells counter electrode. *Electrochim. Acta* **2018**, *280*, 94–100. [CrossRef]
57. Jing, H.Y.; Shi, Y.T.; Wu, D.Y.; Liang, S.X.; Song, X.D.; An, Y.L.; Hao, C. Well-defined heteroatom-rich porous carbon electrocatalyst derived from biowaste for high-performance counter electrode in dye-sensitized solar cells. *Electrochim. Acta* **2018**, *281*, 646–653. [CrossRef]
58. Zheng, H.Q.; Neo, C.Y.; Mei, X.G.; Qiu, J.; Ouyang, J.Y. Reduced graphene oxide films fabricated by gel coating and their application as platinum-free counter electrodes of highly efficient iodide/triiodide dye-sensitized solar cells. *J. Mater. Chem.* **2012**, *22*, 14465–14474. [CrossRef]
59. Xiao, Y.M.; Han, G.Y.; Li, Y.P.; Li, M.Y.; Lin, J.Y. Three-dimensional hollow platinum-nickel bimetallic nanoframes for use in dye-sensitized solar cells. *J. Power Sources* **2015**, *278*, 149–155. [CrossRef]
60. Tang, Q.W.; Zhang, H.H.; Meng, Y.Y.; He, B.L.; Yu, L.M. Dissolution engineering of platinum alloy counter electrodes in dye-sensitized solar cells. *Angew. Chem. Int. Ed.* **2015**, *54*, 11448–11452. [CrossRef]
61. Yang, W.; Li, Z.H.; Xu, X.W.; Hou, L.Q.; Tang, Y.S.; Deng, B.J.; Yang, F.; Wang, Y.; Li, Y.F. Atomic N-coordinated cobalt sites within nanomesh graphene as highly efficient electrocatalysts for triiodide reduction in dye-sensitized solar cells. *Chem. Eng. J.* **2018**, *349*, 782–790. [CrossRef]
62. Hou, W.J.; Xiao, Y.M.; Han, G.Y. The dye-sensitized solar cells based on the interconnected ternary cobalt diindium sulfide nanosheet array counter electrode. *Mater. Res. Bull.* **2018**, *107*, 204–212. [CrossRef]
63. Tai, Q.D.; Chen, B.L.; Guo, F.; Xu, S.; Hu, H.; Sebo, B.; Zhao, X.Z. In situ prepared transparent polyaniline electrode and its application in bifacial dye-sensitized solar cells. *ACS Nano* **2011**, *5*, 3795–3799. [CrossRef]
64. Tang, Q.W.; Cai, H.Y.; Yuan, S.S.; Wang, X. Counter electrodes from double-layered polyaniline nanostructures for dye-sensitized solar cell applications. *J. Mater. Chem. A* **2013**, *1*, 317–323. [CrossRef]
65. Jeon, S.S.; Kim, C.; Ko, J.; Im, S.S. Spherical polypyrrole nanoparticles as a highly efficient counter electrode for dye-sensitized solar cells. *J. Mater. Chem.* **2011**, *21*, 8146–8151. [CrossRef]
66. Tang, Z.Y.; Wu, J.H.; Zheng, M.; Tang, Q.W.; Liu, Q.; Lin, J.M.; Wang, J.L. High efficient PANI/Pt nanofiber counter electrode used in dye-sensitized solar cell. *RSC Adv.* **2012**, *2*, 4062–4064. [CrossRef]
67. Park, J.W.; Jang, J. Fabrication of graphene/free-standing nanofibrillar PEDOT/P(VDF-HFP) hybrid device for wearable and sensitive electronic skin application. *Carbon* **2015**, *87*, 275–281. [CrossRef]
68. Zhou, L.; Yu, M.J.; Chen, X.L.; Nie, S.H.; Lai, W.Y.; Su, W.M.; Cui, Z.; Huang, W. Screen-Printed poly(3,4-ethylenedioxythiophene): poly(styrenesulfonate) grids as ITO-free anodes for flexible organic light-emitting diodes. *Adv. Funct. Mater.* **2018**, *28*, 1705955. [CrossRef]
69. Lee, K.M.; Chiu, W.H.; Wei, H.Y.; Hu, C.W.; Suryanarayanan, V.; Hsieh, W.F.; Ho, K.C. Effects of mesoscopic poly(3,4-ethylenedioxythiophene) films as counter electrodes for dye-sensitized solar cells. *Thin Solid Film.* **2010**, *518*, 1716–1721. [CrossRef]
70. Chen, P.Y.; Li, C.T.; Lee, C.P.; Vittal, R.; Ho, K.C. PEDOT-decorated nitrogen-doped graphene as the transparent composite film for the counter electrode of a dye-sensitized solar cell. *Nano Energy* **2015**, *12*, 374–385. [CrossRef]

71. Lim, S.P.; Pandikumar, A.; Lim, Y.S.; Huang, N.M.; Lim, H.N. In-situ electrochemically deposited polypyrrole nanoparticles incorporated reduced graphene oxide as an efficient counter electrode for platinum-free dye-sensitized solar cells. *Sci. Rep.* **2014**, *4*, 5305. [CrossRef]
72. Li, Y.; Feng, Q.Y.; Wang, H.; Zhou, G.; Wang, Z.S. Reduced graphene oxide-Ta_3N_5 composite: A potential cathode for efficient $Co(bpy)_3^{3+/2+}$ mediated dye-sensitized solar cells. *J. Mater. Chem. A* **2013**, *1*, 6342–6349. [CrossRef]
73. Huo, J.H.; Zheng, M.; Tu, Y.G.; Wu, J.H. High-performance and transparent counter electrodes based on polypyrrole and ferrous sulfide nanoparticles for dye-sensitized solar cells. *J. Mater. Sci. Mater. Electron.* **2016**, *27*, 5680–5685. [CrossRef]
74. Hwang, D.K.; Song, D.; Jeon, S.S.; Han, T.H.; Kang, Y.S.; Im, S.S. Ultrathin polypyrrole nanosheets doped with HCl as counter electrodes in dye-sensitized solar cells. *J. Mater. Chem. A* **2014**, *2*, 859–865. [CrossRef]
75. Veerender, P.; Saxena, V.; Jha, P.; Koiry, S.P.; Gusain, A.; Samanta, S.; Chauhan, A.K.; Aswal, D.K.; Gupta, S.K. Free-standing polypyrrole films as substrate-free and pt-free counterelectrodes for quasi-solid dye-sensitized solar cells. *Org. Electron.* **2012**, *13*, 3032–3039. [CrossRef]
76. Peng, T.; Sun, W.W.; Huang, C.L.; Yu, W.J.; Sebo, B.; Dai, Z.G.; Guo, S.S.; Zhao, X.Z. Self-assembled free-standing polypyrrole nanotube membrane as an efficient FTO- and pt-free counter electrode for dye-sensitized solar cells. *ACS Appl. Mater. Interfaces* **2014**, *6*, 14–17. [CrossRef] [PubMed]
77. Wu, J.H.; Li, Q.H.; Fan, L.Q.; Lan, Z.; Li, P.J.; Lin, J.M.; Hao, S.C. High-performance polypyrrole nanoparticles counter electrode for dye-sensitized solar cells. *J. Power Sources* **2008**, *181*, 172–176. [CrossRef]
78. Bu, C.H.; Tai, Q.D.; Liu, Y.M.; Guo, S.S.; Zhao, X.Z. A transparent and stable polypyrrole counter electrode for dye-sensitized solar cell. *J. Power Sources* **2013**, *221*, 78–83. [CrossRef]
79. Wang, G.Q.; Dong, W.N.; Yan, C.; Hou, S.; Zhang, W. Facile synthesis of hierarchical nanostructured polypyrrole and its application in the counter electrode of dye-sensitized solar cells. *Mater. Lett.* **2018**, *214*, 158–161. [CrossRef]
80. Xu, Q.; Li, M.X.; Yan, P.; Wei, C.Z.; Fang, L.L.; Wei, W.; Bao, H.F.; Xu, J.; Xu, W.L. Polypyrrole-coated cotton fabrics prepared by electrochemical polymerization as textile counter electrode for dye-sensitized solar cells. *Org. Electron.* **2016**, *29*, 107–113. [CrossRef]
81. Saranya, K.; Rameez, M.; Subramania, A. Developments in conducting polymer based counter electrodes for dye-sensitized solar cells-an overview. *Eur. Polym. J.* **2015**, *66*, 207–227. [CrossRef]
82. Li, Q.H.; Wu, J.H.; Tang, Q.W.; Lan, Z.; Li, P.J.; Lin, J.M.; Fan, L.Q. Application of microporous polyaniline counter electrode for dye-sensitized solar cells. *Electrochem. Commun.* **2008**, *10*, 1299–1302. [CrossRef]
83. Hou, W.J.; Xiao, Y.Y.; Han, G.Y.; Fu, D.Y.; Wu, R.F. Serrated, flexible and ultrathin polyaniline nanoribbons: An efficient counter electrode for the dye-sensitized solar cell. *J. Power Sources* **2016**, *322*, 155–162. [CrossRef]
84. Wang, H.; Feng, Q.Y.; Gong, F.; Li, Y.; Zhou, G.; Wang, Z.S. In situ growth of oriented polyaniline nanowires array for efficient cathode of Co(III)/Co(II) mediated dye-sensitized solar cell. *J. Mater. Chem. A* **2013**, *1*, 97–104. [CrossRef]
85. Xiao, Y.M.; Lin, J.Y.; Wang, W.Y.; Tai, S.Y.; Yue, G.T.; Wu, J.H. Enhanced performance of low-cost dye-sensitized solar cells with pulse-electropolymerized polyaniline counter electrodes. *Electrochim. Acta* **2013**, *90*, 468–474. [CrossRef]
86. Burschka, J.; Brault, V.; Ahmad, S.; Breau, L.; Nazeeruddin, M.K.; Marsan, B.; Zakeeruddin, S.M.; Grätzel, M. Influence of the counter electrode on the photovoltaic performance of dye-sensitized solar cells using a disulfide/thiolate redox electrolyte. *Energy Environ. Sci.* **2012**, *5*, 6089–6097. [CrossRef]
87. Li, Z.P.; Ye, B.X.; Hu, X.D.; Ma, X.Y.; Zhang, X.P.; Deng, Y.Q. Facile electropolymerized-PANI as counter electrode for low cost dye-sensitized solar cell. *Electrochem. Commun.* **2009**, *11*, 1768–1771. [CrossRef]
88. Yun, S.N.; Hagfeldt, A.; Ma, T.L. Pt-free counter electrode for dye-sensitized solar cells with high efficiency. *Adv. Mater.* **2014**, *26*, 6210–6237. [CrossRef]
89. Wei, W.; Wang, H.; Hu, Y.H. A review on PEDOT-based counter electrodes for dye-sensitized solar cells. *Int. J. Energy Res.* **2014**, *38*, 1099–1111. [CrossRef]
90. Worfolk, B.J.; Andrews, S.C.; Park, S.; Reinspach, J.; Liu, N.; Toney, M.F.; Mannsfeld, S.C.B.; Bao, Z.N. Ultrahigh electrical conductivity in solution-sheared polymeric transparent films. *Proc. Natl. Acad. Sci. USA* **2015**, *112*, 14138–14143. [CrossRef]

91. Lee, K.M.; Chen, P.Y.; Hsu, C.Y.; Huang, J.H.; Ho, W.H.; Chen, H.C.; Ho, K.C. A high-performance counter electrode based on poly(3,4-alkylenedioxythiophene) for dye-sensitized solar cells. *J. Power Sources* **2009**, *188*, 313–318. [CrossRef]
92. Li, H.G.; Xiao, Y.M.; Han, G.Y.; Hou, W.J. Honeycomb-like poly(3,4-ethylenedioxythiophene) as an effective and transparent counter electrode in bifacial dye-sensitized solar cells. *J. Power Sources* **2017**, *342*, 709–716. [CrossRef]
93. Trevisan, R.; Döbbelin, M.; Boix, P.P.; Barea, E.M.; Tena-Zaera, R.; Mora-Seró, I.; Bisquert, J. PEDOT nanotube arrays as high performing counter electrodes for dye sensitized solar cells. Study of the interactions among electrolytes and counter electrodes. *Adv. Energy Mater.* **2011**, *1*, 781–784. [CrossRef]
94. Xia, J.B.; Masaki, N.; Jiang, K.J.; Yanagida, S. The influence of doping ions on poly(3,4-ethylenedioxythiophene) as a counter electrode of a dye-sensitized solar cell. *J. Mater. Chem.* **2007**, *17*, 2845–2850. [CrossRef]
95. Li, R.; Tang, Q.W.; Yu, L.M.; Yan, X.F.; Zhang, Z.M.; Yang, P.Z. Counter electrodes from conducting polymer intercalated graphene for dye-sensitized solar cells. *J. Power Sources* **2016**, *309*, 231–237. [CrossRef]
96. He, B.L.; Tang, Q.W.; Wang, M.; Ma, C.Q.; Yuan, S.S. Complexation of polyaniline and graphene for efficient counter electrodes in dye-sensitized solar cells: Enhanced charge transfer ability. *J. Power Sources* **2014**, *256*, 8–13. [CrossRef]
97. Zhang, H.H.; He, B.L.; Tang, Q.W.; Yu, L.M. Bifacial dye-sensitized solar cells from covalent-bonded polyanilineemultiwalled carbon nanotube complex counter electrodes. *J. Power Sources* **2015**, *275*, 489–497. [CrossRef]
98. He, B.L.; Tang, Q.W.; Luo, J.H.; Li, Q.H.; Chen, X.X.; Cai, H.Y. Rapid charge-transfer in polypyrrole-single wall carbon nanotube complex counter electrodes: Improved photovoltaic performances of dye-sensitized solar cells. *J. Power Sources* **2014**, *256*, 170–177. [CrossRef]
99. Xiao, Y.M.; Lin, J.Y.; Wu, J.H.; Tai, S.Y.; Yue, G.T.; Lin, T.W. Dye-sensitized solar cells with high-performance polyaniline/multi-wall carbon nanotube counter electrodes electropolymerized by a pulse potentiostatic technique. *J. Power Sources* **2013**, *233*, 320–325. [CrossRef]
100. Li, H.G.; Xiao, Y.M.; Han, G.Y.; Zhang, Y. A transparent honeycomb-like poly(3,4-ethylenedioxythiophene) /multi-wall carbon nanotube counter electrode for bifacial dyesensitized solar cells. *Org. Electron.* **2017**, *50*, 161–169. [CrossRef]
101. Hou, W.J.; Xiao, Y.M.; Han, G.Y.; Zhou, H.H. Electro-polymerization of polypyrrole/multi-wall carbon nanotube counter electrodes for use in platinum-free dye-sensitized solar cells. *Electrochim. Acta* **2016**, *190*, 720–728. [CrossRef]
102. Xu, H.X.; Zhang, X.Y.; Zhang, C.J.; Liu, Z.H.; Zhou, X.H.; Pang, S.P.; Chen, X.; Dong, S.M.; Zhang, Z.Y.; Zhang, L.X.; et al. Nanostructured titanium nitride/PEDOT:PSS composite films as counter electrodes of dye-sensitized solar cells. *ACS Appl. Mater. Interfaces* **2012**, *4*, 1087–1092. [CrossRef] [PubMed]
103. Di, Y.; Xiao, Z.H.; Liu, Z.T.; Chen, B.; Feng, J.W. Hybrid films of PEDOT containing transition metal phosphates as high effective Pt-free counter electrodes for dye sensitized solar cells. *Org. Electron.* **2018**, *57*, 171–177. [CrossRef]
104. Ramasamy, M.S.; Nikolakapoulou, A.; Raptis, D.; Dracopoulos, V.; Paterakis, G.; Lianos, P. Reduced graphene oxide/Polypyrrole/PEDOT composite films as efficient Pt-free counter electrode for dye-sensitized solar cells. *Electrochim. Acta* **2015**, *173*, 276–281. [CrossRef]
105. Yue, G.T.; Wu, J.H.; Xiao, Y.M.; Lin, J.M.; Huang, M.L.; Lan, Z. Application of poly(3,4-ethylenedioxythiophene):polystyrenesulfonate/polypyrrole counter electrode for dye-sensitized solar cells. *J. Phys. Chem. C* **2012**, *116*, 18057–18063. [CrossRef]
106. Goncalves, L.M.; Bermudez, V.D.Z.; Ribeiro, H.A.; Mendes, A.M. Dye-sensitized solar cells: A safe bet for the future. *Energy Environ. Sci.* **2008**, *1*, 655–667. [CrossRef]
107. Grätzel, M. Recent advances in sensitized mesoscopic solar cells. *Acc. Chem. Res.* **2009**, *42*, 1788–1798. [CrossRef]
108. Li, B.; Guo, E.Y.; Wang, C.X.; Yin, L.W. Novel Au inlaid Zn_2SnO_4/SnO_2 hollow rounded cubes for dye-sensitized solar cells with enhanced photoelectric conversion performance. *J. Mater. Chem. A* **2016**, *4*, 466–477. [CrossRef]
109. Yu, Z.; Vlachopoulos, N.; Gorlov, M.; Kloo, L. Liquid electrolytes for dye-sensitized solar cells. *Dalton Trans.* **2011**, *40*, 10289–10303. [CrossRef]
110. Hamann, T.W.; Ondersma, J.W. Dye-sensitized solar cell redox shuttles. *Energy Environ. Sci.* **2011**, *4*, 370–381. [CrossRef]

111. Mathew, S.; Yella, A.; Gao, P.; Humphry-Baker, R.; Curchod, B.F.E.; Ashari-Astani, N.; Tavernelli, I.; Rothlisberger, U.; Nazeeruddin, M.K.; Grätzel, M. Dye-sensitized solar cells with 13% efficiency achieved through the molecular engineering of porphyrin sensitizers. *Nat. Chem.* **2014**, *6*, 242–247. [CrossRef]
112. Kakiage, K.; Aoyama, Y.; Yano, T.; Oya, K.; Fujisawa, J.; Hanaya, M. Highly-efficient dye-sensitized solar cells with collaborative sensitization by silyl-anchor and carboxy-anchor dyes. *Chem. Commun.* **2015**, *51*, 15894–15897. [CrossRef]
113. Wang, P.; Wenger, B.; Humphry-Baker, R.; Moser, J.E.; Teuscher, J.; Kantlehner, W.; Mezger, J.; Stoyanov, E.V.; Zakeeruddin, S.M.; Grätzel, M. Charge separation and efficient light energy conversion in sensitized mesoscopic solar cells based on binary ionic liquids. *J. Am. Chem. Soc.* **2005**, *127*, 6850–6856. [CrossRef] [PubMed]
114. Wu, J.H.; Lan, Z.; Hao, S.C.; Li, P.J.; Lin, J.M.; Huang, M.L.; Fang, L.Q.; Huang, Y.F. Progress on the electrolytes for dye-sensitized solar cells. *Pure Appl. Chem.* **2008**, *80*, 2241–2258. [CrossRef]
115. Chalkias, D.A.; Giannopoulos, D.I.; Kollia, E.; Petala, A.; Kostopoulos, V.; Papanicolaou, G.C. Preparation of polyvinylpyrrolidone-based polymer electrolytes and their application by in-situ gelation in dye-sensitized solar cells. *Electrochim. Acta* **2018**, *271*, 632–640. [CrossRef]
116. Wang, P.; Zakeeruddin, S.M.; Moser, J.E.; Nazeeruddin, M.K.; Sekiguchi, T.; Grätzel, M. A stable quasi-solid-state dye-sensitized solar cell with an amphiphilic ruthenium sensitizer and polymer gel electrolyte. *Nat. Mater.* **2003**, *2*, 402–407. [CrossRef] [PubMed]
117. Nogueira, A.F.; Longo, C.; Paoli, M.A.D. Polymers in dye sensitized solar cells: Overview and perspectives. *Coord. Chem. Rev.* **2004**, *248*, 1455–1468. [CrossRef]
118. Nogueira, A.F.; Paoli, M.A.D. Electron transfer dynamics in dye sensitized nanocrystalline solar cells using a polymer electrolyte. *J. Phys. Chem. B* **2001**, *105*, 7517–7524. [CrossRef]
119. Cao, F.; Oskam, G.; Searson, P.C. A solid state, dye sensitized photoelectrochemical cell. *J. Phys. Chem.* **1995**, *99*, 17071–17073. [CrossRef]
120. Wu, J.H.; Lan, Z.; Wang, D.B.; Hao, S.C.; Lin, J.M.; Huang, Y.F.; Yin, S.; Sato, T. Gel polymer electrolyte based on poly(acrylonitrile-co-styrene) and a novel organic iodide salt for quasi-solid state dye-sensitized solar cell. *Electrochim. Acta* **2006**, *51*, 4243–4249. [CrossRef]
121. Wu, J.H.; Hao, S.C.; Lan, Z.; Lin, J.M.; Huang, M.L.; Huang, Y.F.; Fang, L.Q.; Yin, S.; Sato, T. A thermoplastic gel electrolyte for stable quasi-solid-state dye-sensitized solar cells. *Adv. Funct. Mater.* **2007**, *17*, 2645–2652. [CrossRef]
122. Shi, Y.T.; Zhan, C.; Wang, L.D.; Ma, B.B.; Gao, R.; Zhu, Y.F.; Qiu, Y. The electrically conductive function of high-molecular weight poly(ethylene oxide) in polymer gel electrolytes used for dye-sensitized solar cells. *Phys. Chem. Chem. Phys.* **2009**, *11*, 4230–4235. [CrossRef] [PubMed]
123. Lee, K.S.; Jun, Y.; Park, J.H. Controlled dissolution of polystyrene nanobeads: Transition from liquid electrolyte to gel electrolyte. *Nano Lett.* **2012**, *12*, 2233–2237. [CrossRef] [PubMed]
124. Lan, Z.; Wu, J.H.; Wang, D.B.; Hao, S.C.; Lin, J.M.; Huang, Y.F. Quasi-solid-state dye-sensitized solar cells based on a sol-gel organic-inorganic composite electrolyte containing an organic iodide salt. *Sol. Energy* **2007**, *81*, 117–122. [CrossRef]
125. Su, J.Y.; Tsai, C.H.; Wang, S.A.; Huang, T.W.; Wu, C.C.; Wong, K.T. Functionalizing organic dye with cross-linked electrolyte-blocking shell as a new strategy for improving DSSC efficiency. *RSC Adv.* **2012**, *2*, 3722–3728. [CrossRef]
126. Lan, Z.; Wu, J.H.; Hao, S.C.; Lin, J.M.; Huang, M.L.; Huang, Y.F. Template-free synthesis of closed-microporous hybrid and its application in quasi-solid-state dye-sensitized solar cells. *Energy Environ. Sci.* **2009**, *2*, 524–528. [CrossRef]
127. Parvez, M.K.; In, I.; Park, J.M.; Lee, S.H.; Kim, S.R. Long-term stable dye-sensitized solar cells based on UV photo-crosslinkable poly(ethylene glycol) and poly(ethylene glycol) diacrylate based electrolytes. *Sol. Energy Mater. Sol. Cells* **2011**, *95*, 318–322. [CrossRef]
128. Wang, L.; Fang, S.B.; Lin, Y.; Zhou, X.W.; Li, M.Y. A 7.72% efficient dye sensitized solar cell based on novel necklace-like polymer gel electrolyte containing latent chemically cross-linked gel electrolyte precursors. *Chem. Commun.* **2005**, *45*, 5687–5689. [CrossRef]
129. Wu, J.H.; Lan, Z.; Lin, J.M.; Huang, M.L.; Hao, S.C.; Sato, T.; Yin, S. A novel thermosetting gel electrolyte for stable quasi-solid-state dye-sensitized solar cells. *Adv. Mater.* **2007**, *19*, 4006–4011. [CrossRef]

130. Stergiopoulos, T.; Arabatzis, I.M.; Katsaros, G.; Falaras, P. Binary polyethylene oxide/titania solid-state redox electrolyte for highly efficient nanocrystalline TiO_2 photoelectrochemical cells. *Nano Lett.* **2002**, *2*, 1259–1261. [CrossRef]
131. Katsaros, G.; Stergiopoulos, T.; Arabatzis, I.M.; Papadokostaki, K.G.; Falaras, P. A solvent-free composite polymer/inorganic oxide electrolyte for high efficiency solid-state dye-sensitized solar cells. *J. Photochem. Photobiol. A Chem.* **2002**, *149*, 191–198. [CrossRef]
132. Yoon, I.N.; Song, H.K.; Won, J.; Kang, Y.S. Shape dependence of SiO_2 nanomaterials in a quasi-solid electrolyte for application in dye-sensitized solar cells. *J. Phys. Chem. C* **2014**, *118*, 3918–3924. [CrossRef]
133. Huo, Z.P.; Dai, S.Y.; Wang, K.J.; Kong, F.T.; Zhang, C.N.; Pan, X.; Fang, X.Q. Nanocomposite gel electrolyte with large enhanced charge transport properties of an I_3^-/I^- redox couple for quasi-solid-state dye-sensitized solar cells. *Sol. Energy Mater. Sol. Cells* **2007**, *91*, 1959–1965. [CrossRef]
134. Zhang, Y.; Tang, Q.W.; He, B.L.; Yang, P.Z. Graphene enabled all-weather solar cells for electricity harvest from sun and rain. *J. Mater. Chem. A* **2016**, *4*, 13235–13241. [CrossRef]
135. Tang, Q.W.; Zhang, H.N.; He, B.L.; Yang, P.Z. An all-weather solar cell that can harvest energy from sunlight and rain. *Nano Energy* **2016**, *30*, 818–824. [CrossRef]
136. Meng, Y.Y.; Zhang, Y.; Sun, W.Y.; Wang, M.; He, B.L.; Chen, H.Y.; Tang, Q.W. Biomass converted carbon quantum dots for all-weather solar cells. *Electrochim. Acta* **2017**, *257*, 259–266. [CrossRef]
137. Zhu, W.L.; Wang, M.; Wang, Z.L.; Sun, W.Y.; He, B.L.; Tang, Q.W. Photoelectric engineering of all-weather bifacial solar cells in the dark. *Electrochim. Acta* **2017**, *254*, 299–307. [CrossRef]
138. Duan, J.L.; Duan, Y.Y.; Zhao, Y.Y.; Wang, Y.L.; Tang, Q.W.; He, B.L. Bifunctional polyaniline electrode tailored hybridized solar cells for energy harvesting from sun and rain. *J. Energy Chem.* **2018**, *27*, 742–747. [CrossRef]
139. Ye, F.; Chen, H.; Xie, F.X.; Tang, W.T.; Yin, M.S.; He, J.J.; Bi, E.B.; Wang, Y.B.; Yang, X.D.; Han, L.Y. Soft-cover deposition of scaling-up uniform perovskite thin films for high cost-performance solar cells. *Energy Environ. Sci.* **2016**, *9*, 2295–2301. [CrossRef]
140. Yang, W.S.; Park, B.W.; Jung, E.H.; Jeon, N.J.; Kim, Y.C.; Lee, D.U.; Shin, S.S.; Seo, J.; Kim, E.K.; Noh, J.H.; et al. Iodide management in formamidinium-lead-halide- based perovskite layers for efficient solar cells. *Science* **2017**, *356*, 1376–1379. [CrossRef]
141. Zhang, T.Y.; Li, G.; Xu, F.; Wang, Y.P.; Guo, N.J.; Qian, X.F.; Zhao, Y.X. In situ gas/solid reaction for the formation of luminescent quantum confined $CH_3NH_3PbBr_3$ perovskite planar film. *Chem. Commun.* **2016**, *52*, 11080–11083. [CrossRef]
142. Huang, J.B.; Tan, S.Q.; Lund, P.D.; Zhou, H.P. Impact of H_2O on organic-inorganic hybrid perovskite solar cells. *Energy Environ. Sci.* **2017**, *10*, 2284–2311. [CrossRef]
143. Green, M.A.; Ho-Baillie, A.; Snaith, H.J. The emergence of perovskite solar cells. *Nat. Photon.* **2014**, *8*, 506–514. [CrossRef]
144. Calió, L.; Kazim, S.; Grätzel, M.; Ahmad, S. Hole-transport materials for perovskite solar cells. *Angew. Chem. Int. Ed.* **2016**, *55*, 14522–14545. [CrossRef] [PubMed]
145. Marchioro, A.; Teuscher, J.; Friedrich, D.; Kunst, M.; Krol, R.V.D.; Moehl, T.; Grätzel, M.; Moser, J.E. Unravelling the mechanism of photoinduced charge transfer processes in lead iodide perovskite solar cells. *Nat. Photonics* **2014**, *8*, 250–255. [CrossRef]
146. Sum, T.C.; Mathews, N. Advancements in perovskite solar cells: Photophysics behind the photovoltaics. *Energy Environ. Sci.* **2014**, *7*, 2518–2534. [CrossRef]
147. Shi, S.W.; Li, Y.F.; Li, X.Y.; Wang, H.Q. Advancements in all-solid-state hybrid solar cells based on organometal halide perovskites. *Mater. Horiz.* **2015**, *2*, 378–405. [CrossRef]
148. Shen, Q.; Ogomi, Y.; Chang, J.; Toyoda, T.; Fujiwara, K.; Yoshino, K.; Sato, K.; Yamazaki, K.; Akimoto, M.; Kuga, Y.; et al. Optical absorption, charge separation and recombination dynamics in Sn/Pb cocktail perovskite solar cells and their relationships to photovoltaic performances. *J. Mater. Chem. A* **2015**, *3*, 9308–9316. [CrossRef]
149. Eperon, G.E.; Burlakov, V.M.; Docampo, P.; Goriely, A.; Snaith, H.J. Morphological control for high performance, solution-processed planar heterojunction perovskite solar cells. *Adv. Funct. Mater.* **2014**, *24*, 151–157. [CrossRef]
150. Salim, T.; Sun, S.Y.; Abe, Y.; Krishna, A.; Grimsdale, A.C.; Lam, Y.M. Perovskite-based solar cells: Impact of morphology and device architecture on device performance. *J. Mater. Chem. A* **2015**, *3*, 8943–8969. [CrossRef]

151. Nie, W.Y.; Tsai, H.; Asadpour, R.; Blancon, J.C.; Neukirch, A.J.; Gupta, G.; Crochet, J.J.; Chhowalla, M.; Tretiak, S.; Alam, M.A.; et al. High-efficiency solution-processed perovskite solar cells with millimeter-scale grains. *Science* **2015**, *347*, 522–525. [CrossRef]
152. Xiao, M.D.; Huang, F.Z.; Huang, W.C.; Dkhissi, Y.; Zhu, Y.; Etheridge, J.; Gray-Weale, A.; Bach, U.; Cheng, Y.B.; Spiccia, L. A fast deposition-crystallization procedure for highly efficient lead iodide perovskite thin-film solar cells. *Angew. Chem. Int. Ed.* **2014**, *53*, 9898–9903. [CrossRef] [PubMed]
153. Liang, P.W.; Liao, C.Y.; Chueh, C.C.; Zuo, F.; Williams, S.T.; Xin, X.K.; Lin, J.J.; Jen, A.K.Y. Additive enhanced crystallization of solution-processed perovskite for highly efficient planar-heterojunction solar cells. *Adv. Mater.* **2014**, *26*, 3748–3754. [CrossRef] [PubMed]
154. Xu, J.X.; Buin, A.; Ip, A.H.; Li, W.; Voznyy, O.; Comin, R.; Yuan, M.J.; Jeon, S.; Ning, Z.J.; McDowell, J.J.; et al. Perovskite-fullerene hybrid materials suppress hysteresis in planar diodes. *Nat. Cmmun.* **2015**, *6*, 7081. [CrossRef] [PubMed]
155. Saliba, M.; Matsui, T.; Domanski, K.; Seo, J.Y.; Ummadisingu, A.; Zakeeruddin, S.M.; Correa-Baena, J.P.; Tress, W.R.; Abate, A.; Hagfeldt, A.; et al. Incorporation of rubidium cations into perovskite solar cells improves photovoltaic performance. *Science* **2016**, *354*, 206–209. [CrossRef] [PubMed]
156. Jahandar, M.; Heo, J.H.; Song, C.E.; Kong, K.J.; Shin, W.S.; Lee, J.C.; Im, S.H.; Moon, S.J. Highly efficient metal halide substituted $CH_3NH_3I(PbI_2)_{1-X}(CuBr_2)_X$ planar perovskite solar cells. *Nano Energy* **2016**, *27*, 330–339. [CrossRef]
157. Zhao, Y.X.; Zhu, K. Efficient planar perovskite solar cells based on 1.8 eV band gap $CH_3NH_3PbI_2Br$ nanosheets via thermal decomposition. *J. Am. Chem. Soc.* **2014**, *136*, 12241–12244. [CrossRef] [PubMed]
158. Zhao, L.C.; Luo, D.Y.; Wu, J.; Hu, Q.; Zhang, W.; Chen, K.; Liu, T.H.; Liu, Y.; Zhang, Y.F.; Liu, F.; et al. High-performance inverted planar heterojunction perovskite solar cells based on lead acetate precursor with efficiency exceeding 18%. *Adv. Funct. Mater.* **2016**, *26*, 3508–3514. [CrossRef]
159. Li, S.S.; Chang, C.H.; Wang, Y.C.; Lin, C.W.; Wang, D.Y.; Lin, J.C.; Chen, C.C.; Sheu, H.S.; Chia, H.C.; Wu, W.R.; et al. Intermixing-seeded growth for high-performance planar heterojunction perovskite solar cells assisted by precursor-capped nanoparticles. *Energy Environ. Sci.* **2016**, *9*, 1282–1289. [CrossRef]
160. Tripathi, N.; Shirai, Y.; Yanagida, M.; Karen, A.; Miyano, K. Novel surface passivation technique for low-temperature solution-processed perovskite PV cells. *ACS Appl. Mater. Interfaces* **2016**, *8*, 4644–4650. [CrossRef]
161. Li, T.T.; Pan, Y.F.; Wang, Z.; Xia, Y.D.; Chen, Y.H.; Huang, W. Additive engineering for highly efficient organic-inorganic halide perovskite solar cells: Recent advances and perspectives. *J. Mater. Chem. A* **2017**, *5*, 12602–12652. [CrossRef]
162. Zuo, C.T.; Ding, L.M. An 80.11% FF record achieved for perovskite solar cells by using the NH_4Cl additive. *Nanoscale* **2014**, *6*, 9935–9938. [CrossRef] [PubMed]
163. Xiao, Z.G.; Wang, D.; Dong, Q.F.; Wang, Q.; Wei, W.; Dai, J.; Zeng, X.C.; Huang, J.S. Unraveling the hidden function of a stabilizer in a precursor in improving hybrid perovskite film morphology for high efficiency solar cells. *Energy Environ. Sci.* **2016**, *9*, 867–872. [CrossRef]
164. Zuo, L.J.; Guo, H.X.; DeQuilettes, D.W.; Jariwala, S.; Marco, N.D.; Dong, S.Q.; DeBlock, R.; Ginger, D.S.; Dunn, B.; Wang, M.K.; et al. Polymer-modified halide perovskite films for efficient and stable planar heterojunction solar cells. *Sci. Adv.* **2017**, *3*, e1700106. [CrossRef] [PubMed]
165. Dong, Q.Q.; Wang, Z.W.; Zhang, K.C.; Yu, H.; Huang, P.; Liu, X.D.; Zhou, Y.; Chen, N.; Song, B. Easily accessible polymer additives for tuning the crystal-growth of perovskite thin-films for highly efficient solar cells. *Nanoscale* **2016**, *8*, 5552–5558. [CrossRef] [PubMed]
166. Chaudhary, B.; Kulkarni, A.; Jena, A.K.; Ikegami, M.; Udagawa, Y.; Kunugita, H.; Ema, K.; Miyasaka, T. Poly(4-Vinylpyridine)-based interfacial passivation to enhance voltage and moisture stability of lead halide perovskite solar cells. *ChemSusChem* **2017**, *10*, 2473–2479. [CrossRef] [PubMed]
167. Masi, S.; Rizzo, A.; Aiello, F.; Balzano, F.; Uccello-Barretta, G.; Listorti, A.; Giglia, G.; Colella, S. Multiscale morphology design of hybrid halide perovskites through a polymeric template. *Nanoscale* **2015**, *7*, 18956–18963. [CrossRef] [PubMed]
168. Xue, Q.F.; Hu, Z.C.; Sun, C.; Chen, Z.M.; Huang, F.; Yip, H.L.; Cao, Y. Metallohalide perovskite-polymer composite film for hybrid planar heterojunction solar cells. *RSC Adv.* **2015**, *5*, 775–783. [CrossRef]
169. Wang, Y.Y.; Luo, J.M.; Nie, R.M.; Deng, X.Y. Planar perovskite solar cells using $CH_3NH_3PbI_3$ films: A simple process suitable for large-scale production. *Energy Technol.* **2016**, *4*, 473–478. [CrossRef]

170. Chang, C.Y.; Chu, C.Y.; Huang, Y.C.; Huang, C.W.; Chang, S.Y.; Chen, C.A.; Chao, C.Y.; Su, W.F. Tuning perovskite morphology by polymer additive for high efficiency solar cell. *ACS Appl. Mater. Interfaces* **2015**, *7*, 4955–4961. [CrossRef]
171. Zhao, Y.C.; Wei, J.; Li, H.; Yan, Y.; Zhou, W.K.; Yu, D.P.; Zhao, Q. A polymer scaffold for self-healing perovskite solar cells. *Nat. Commun.* **2016**, *7*, 10228. [CrossRef]
172. Guo, Y.L.; Shoyama, K.; Sato, W.; Nakamura, E. Polymer stabilization of lead(II) perovskite cubic nanocrystals for semitransparent solar cells. *Adv. Energy Mater.* **2016**, *6*, 1502317. [CrossRef]
173. Bi, D.Q.; Yi, C.Y.; Luo, J.S.; Décoppet, J.D.; Zhang, F.; Zakeeruddin, S.M.; Li, X.; Hagfeldt, A.; Grätzel, M. Polymer-templated nucleation and crystal growth of perovskite films for solar cells with efficiency greater than 21%. *Nat. Energy* **2016**, *1*, 16142. [CrossRef]
174. Wang, F.J.; Shimazaki, A.; Yang, F.J.; Kanahashi, K.; Matsuki, K.; Miyauchi, Y.; Takenobu, T.; Wakamiya, A.; Murata, Y.; Matsuda, K. Highly efficient and stable perovskite solar cells by interfacial engineering using solution-processed polymer layer. *J. Phys. Chem. C* **2017**, *121*, 1562–1568. [CrossRef]
175. Ji, X.X.; Peng, X.F.; Wang, Q.; Ren, J.; Xiong, Z.H.; Yang, X.H. On the performance of polymer:organometal halide perovskite composite light emitting devices: The effects of polymer additives. *Org. Electron.* **2018**, *52*, 350–355. [CrossRef]
176. Piatkowski, P.; Cohen, B.; Ramos, F.J.; Nunzio, M.D.; Nazeeruddin, M.K.; Grätzel, M.; Ahmad, S.; Douhal, A. Direct monitoring of ultrafast electron and hole dynamics in perovskite solar cells. *Phys. Chem. Chem. Phys.* **2015**, *17*, 14674–14684. [CrossRef] [PubMed]
177. Yu, Z.; Sun, L.C. Recent progress on hole-transporting materials for emerging organometal halide perovskite solar cells. *Adv. Energy Mater.* **2015**, *5*, 1500213. [CrossRef]
178. Leijtens, T.; Lim, J.; Teuscher, J.; Park, T.; Snaith, H.J. Charge density dependent mobility of organic hole-transporters and mesoporous TiO_2 determined by transient mobility spectroscopy: Implications to dye-sensitized and organic solar cells. *Adv. Mater.* **2013**, *25*, 3227–3233. [CrossRef]
179. Cappel, U.B.; Daeneke, T.; Bach, U. Oxygen-induced doping of Spiro-MeOTAD in solid-state dye-sensitized solar cells and its impact on device performance. *Nano Lett.* **2012**, *12*, 4925–4931. [CrossRef]
180. Nguyen, W.H.; Bailie, C.D.; Unger, E.L.; McGehee, M.D. Enhancing the hole-conductivity of Spiro-OMeTAD without oxygen or lithium salts by using $Spiro(TFSI)_2$ in perovskite and dye-sensitized solar cells. *J. Am. Chem. Soc.* **2014**, *136*, 10996–11001. [CrossRef]
181. Lee, I.; Yun, J.H.; Son, H.J.; Kim, T.S. Accelerated degradation due to weakened adhesion from Li-TFSI additives in perovskite solar cells. *ACS Appl. Mater. Interfaces* **2017**, *9*, 7029–7035. [CrossRef]
182. Abate, A.; Leijtens, T.; Pathak, S.; Teuscher, J.; Avolio, R.; Errico, M.E.; Kirkpatrik, J.; Ball, J.M.; Docampo, P.; McPhersonc, I.; et al. Lithium salts as "redox active" p-type dopants for organic semiconductors and their impact in solid-state dye-sensitized solar cells. *Phys. Chem. Chem. Phys.* **2013**, *15*, 2572–2579. [CrossRef] [PubMed]
183. Bakr, Z.H.; Wali, Q.; Fakharuddin, A.; Schmidt-Mendec, L.; Brown, T.M.; Jose, R. Advances in hole transport materials engineering for stable and efficient perovskite solar cells. *Nano Energy* **2017**, *34*, 271–305. [CrossRef]
184. Chen, W.; Wu, Y.Z.; Yue, Y.F.; Liu, J.; Zhang, W.J.; Yang, X.D.; Chen, H.; Bi, E.B.; Ashraful, I.; Grätzel, M.; et al. Efficient and stable large-area perovskite solar cells with inorganic charge extraction layers. *Science* **2015**, *350*, 944–948. [CrossRef] [PubMed]
185. Arora, N.; Dar, M.I.; Hinderhofer, A.; Pellet, N.; Schreiber, F.; Zakeeruddin, S.M.; Grätzel, M. Perovskite solar cells with CuSCN hole extraction layers yield stabilized efficiencies greater than 20%. *Science* **2017**, *358*, 768–771. [CrossRef] [PubMed]
186. Christians, J.A.; Fung, R.C.M.; Kamat, P.V. An inorganic hole conductor for organo-lead halide perovskite solar cells. Improved hole conductivity with copper iodide. *J. Am. Chem. Soc.* **2014**, *136*, 758–764. [CrossRef] [PubMed]
187. Qin, P.; Tanaka, S.; Ito, S.; Tetreault, N.; Manabe, K.; Nishino, H.; Nazeeruddin, M.K.; Grätzel, M. Inorganic hole conductor-based lead halide perovskite solar cells with 12.4% conversion efficiency. *Nat. Commun.* **2014**, *5*, 3834. [CrossRef] [PubMed]
188. Yang, X.C.; Wang, H.X.; Cai, B.; Yu, Z.; Sun, L.C. Progress in hole-transporting materials for perovskite solar cells. *J. Energy Chem.* **2018**, *27*, 650–672. [CrossRef]

189. Heo, J.H.; Im, S.H.; Noh, J.H.; Mandal, T.N.; Lim, C.S.; Chang, J.A.; Lee, Y.H.; Kim, H.J.; Sarkar, A.; Nazeeruddin, M.K.; et al. Efficient inorganic-organic hybrid heterojunction solar cells containing perovskite compound and polymeric hole conductors. *Nat. Photonics* **2013**, *7*, 486–491. [CrossRef]
190. Yang, W.S.; Noh, J.H.; Jeon, N.J.; Kim, Y.C.; Ryu, S.; Seo, J.; Seok, S.I. High-performance photovoltaic perovskite layers fabricated through intramolecular exchange. *Science* **2015**, *348*, 1234–1237. [CrossRef] [PubMed]
191. Qin, P.; Tetreault, N.; Dar, M.I.; Gao, P.; McCall, K.L.; Rutter, S.R.; Ogier, S.D.; Forrest, N.D.; Bissett, J.S.; Simms, M.J.; et al. A novel oligomer as a hole transporting material for efficient perovskite solar cells. *Adv. Energy Mater.* **2014**, *5*, 1400980. [CrossRef]
192. Sin, D.H.; Ko, H.; Jo, S.B.; Kim, M.; Bae, G.Y.; Cho, K. Decoupling charge transfer and transport at polymeric hole transport layer in perovskite solar cells. *ACS Appl. Mater. Interfaces* **2016**, *8*, 6546–6553. [CrossRef] [PubMed]
193. Yan, W.B.; Ye, S.Y.; Li, Y.L.; Sun, W.H.; Rao, H.X.; Liu, Z.W.; Bian, Z.Q.; Huang, C.H. Hole-transporting materials in inverted planar perovskite solar cells. *Adv. Energy Mater.* **2016**, *6*, 1600474. [CrossRef]
194. Chen, K.; Wu, P.; Yang, W.Q.; Su, R.; Luo, D.Y.; Yang, X.Y.; Tu, Y.G.; Zhu, R.; Gong, Q.H. Low-dimensional perovskite interlayer for highly efficient lead-free formamidinium tin iodide perovskite solar cells. *Nano Energy* **2018**, *49*, 411–418. [CrossRef]
195. Bai, L.B.; Wang, Z.; Han, Y.M.; Zuo, Z.Y.; Liu, B.; Yu, M.N.; Zhang, H.J.; Lin, J.Y.; Xia, Y.D.; Yin, C.R.; et al. Diarylfluorene-based nano-molecules as dopant-free hole-transporting materials without post-treatment process for flexible p-i-n type perovskite solar cells. *Nano Energy* **2018**, *46*, 241–248. [CrossRef]
196. Zhang, F.; Song, J.; Zhang, L.X.; Niu, F.F.; Hao, Y.Y.; Zeng, P.J.; Niu, H.B.; Huang, J.S.; Lian, J.R. Film-through large perovskite grains formation via a combination of sequential thermal and solvent treatment. *J. Mater. Chem. A* **2016**, *4*, 8554–8561. [CrossRef]
197. Chiang, C.H.; Nazeeruddin, M.K.; Grätzel, M.; Wu, C.G. The synergistic effect of H_2O and DMF towards stable and 20% efficiency inverted perovskite solar cells. *Energy Environ. Sci.* **2017**, *10*, 808–817. [CrossRef]
198. Jørgensen, M.; Norrman, K.; Krebs, F.C. Stability/degradation of polymer solar cells. *Sol. Energy Mater. Sol. Cells* **2008**, *92*, 686–714. [CrossRef]
199. Xue, Q.F.; Chen, G.T.; Liu, M.Y.; Xiao, J.Y.; Chen, Z.M.; Hu, Z.C.; Jiang, X.F.; Zhang, B.; Huang, F.; Yang, W.; et al. Improving film formation and photovoltage of highly efficient inverted-type perovskite solar cells through the incorporation of new polymeric hole selective layers. *Adv. Energy Mater.* **2016**, *6*, 1502021. [CrossRef]
200. Zhao, D.W.; Sexton, M.; Park, H.Y.; Baure, G.; Nino, J.C.; So, F. High-efficiency solution-processed planar perovskite solar cells with a polymer hole transport layer. *Adv. Energy Mater.* **2014**, *5*, 1401855. [CrossRef]
201. Chang, S.H.; Lin, K.F.; Chiu, K.Y.; Tsai, C.L.; Cheng, H.M.; Yeh, S.C.; Wu, W.T.; Chen, W.N.; Chen, C.T.; Chen, S.H.; et al. Improving the efficiency of $CH_3NH_3PbI_3$ based photovoltaics by tuning the work function of the PEDOT:PSS hole transport layer. *Sol. Energy* **2015**, *122*, 892–899. [CrossRef]
202. Ma, S.; Qiao, W.Y.; Cheng, T.; Zhang, B.; Yao, J.X.; Alsaedi, A.; Hayat, T.; Ding, Y.; Tan, Z.A.; Dai, S.Y. Optical-electrical-chemical engineering of PEDOT:PSS by incorporation of hydrophobic nafion for efficient and stable perovskite solar cells. *ACS Appl. Mater. Interfaces* **2018**, *10*, 3902–3911. [CrossRef] [PubMed]
203. Xiao, Y.M.; Han, G.Y.; Chang, Y.Z.; Zhou, H.H.; Li, M.Y.; Li, Y.P. An all-solid-state perovskite-sensitized solar cell based on the dual function polyaniline as the sensitizer and p-type hole-transporting material. *J. Power Sources* **2014**, *267*, 1–8. [CrossRef]
204. Xiao, Y.M.; Han, G.Y.; Wu, J.H.; Lin, J.Y. Efficient bifacial perovskite solar cell based on a highly transparent poly(3,4-ethylenedioxythiophene) as the p-type hole-transporting material. *J. Power Sources* **2016**, *306*, 171–177. [CrossRef]
205. Bi, D.Q.; Yang, L.; Boschloo, G.; Hagfeldt, A.; Johansson, E.M.J. Effect of different hole transport materials on recombination in $CH_3NH_3PbI_3$ perovskite-sensitized mesoscopic solar cells. *J. Phys. Chem. Lett.* **2013**, *4*, 1532–1536. [CrossRef] [PubMed]
206. Edri, E.; Kirmayer, S.; Cahen, D.; Hodes, G. High open-circuit voltage solar cells based on organic-inorganic lead bromide perovskite. *J. Phys. Chem. Lett.* **2013**, *4*, 897–902. [CrossRef] [PubMed]
207. Zhu, Q.Q.; Bao, X.C.; Yu, J.H.; Zhu, D.Q.; Qiu, M.; Yang, R.Q.; Dong, L.F. Compact layer free perovskite solar cells with a high-mobility hole-transporting layer. *ACS Appl. Mater. Interfaces* **2016**, *8*, 2652–2657. [CrossRef] [PubMed]

208. Heo, J.H.; Im, S.H. $CH_3NH_3PbI_3$/poly-3-hexylthiophen perovskite mesoscopic solar cells: Performance enhancement by Li-assisted hole conduction. *Phys. Status Solidi RRL* **2014**, *8*, 816–821. [CrossRef]
209. Cai, M.L.; Tiong, V.T.; Hreid, T.; Bell, J.; Wang, H.X. An efficient hole transport material composite based on poly(3-hexylthiophene) and bamboostructured carbon nanotubes for high performance perovskite solar cells. *J. Mater. Chem. A* **2015**, *3*, 2784–2793. [CrossRef]
210. Xiao, J.Y.; Shi, J.J.; Liu, H.B.; Xu, Y.Z.; Lv, S.T.; Luo, Y.H.; Li, D.M.; Meng, Q.B.; Li, Y.L. Efficient $CH_3NH_3PbI_3$ perovskite solar cells based on graphdiyne (GD)-modified P3HT hole-transporting material. *Adv. Energy Mater.* **2015**, *5*, 1401943. [CrossRef]
211. Habisreutinger, S.N.; Leijtens, T.; Eperon, G.E.; Stranks, S.D.; Nicholas, R.J.; Snaith, H.J. Carbon nanotube/polymer composites as a highly stable hole collection layer in perovskite solar cells. *Nano Lett.* **2014**, *14*, 5561–5568. [CrossRef]
212. Kwon, Y.S.; Lim, J.; Yun, H.J.; Kim, Y.H.; Park, T. A diketopyrrolopyrrole-containing hole transporting conjugated polymer for use in efficient stable organic-inorganic hybrid solar cells based on a perovskite. *Energy Environ. Sci.* **2014**, *7*, 1454–1460. [CrossRef]
213. Kim, G.W.; Kang, G.; Kim, J.; Lee, G.Y.; Kim, H.I.; Pyeon, L.; Leeb, J.; Park, T. Dopant-free polymeric hole transport materials for highly efficient and stable perovskite solar cells. *Energy Environ. Sci.* **2016**, *9*, 2326–2333. [CrossRef]
214. Jung, S.K.; Lee, D.S.; Ann, M.H.; Im, S.H.; Kim, J.H.; Kwon, O.P. Non-fullerene organic electron-transporting materials for perovskite solar cells. *ChemSusChem* **2018**, *11*, 3882–3892. [CrossRef]
215. Sun, C.; Wu, Z.H.; Yip, H.L.; Zhang, H.; Jiang, X.F.; Xue, Q.F.; Hu, Z.C.; Hu, Z.H.; Shen, Y.; Wang, M.K.; et al. Amino-functionalized conjugated polymer as an efficient electron transport layer for high-performance planar-heterojunction perovskite solar cells. *Adv. Energy Mater.* **2016**, *6*, 1501534. [CrossRef]
216. Wang, W.W.; Yuan, J.Y.; Shi, G.Z.; Zhu, X.X.; Shi, S.H.; Liu, Z.K.; Han, L.; Wang, H.Q.; Ma, W.L. Inverted planar heterojunction perovskite solar cells employing polymer as the electron conductor. *ACS Appl. Mater. Interfaces* **2015**, *7*, 3994–3999. [CrossRef] [PubMed]
217. Kim, H.I.; Kim, M.J.; Choi, K.; Lim, C.; Kim, Y.H.; Kwon, S.K.; Park, T. Improving the performance and stability of inverted planar flexible perovskite solar cells employing a novel NDI-based polymer as the electron transport layer. *Adv. Energy Mater.* **2018**, 1702872. [CrossRef]
218. Guo, Q.; Xu, Y.X.; Xiao, B.; Zhang, B.; Zhou, E.J.; Wang, F.Z.; Bai, Y.M.; Hayat, T.; Alsaedi, A.; Tan, Z.A. Effect of energy alignment, electron mobility, and film morphology of perylene diimide based polymers as electron transport layer on the performance of perovskite solar cells. *ACS Appl. Mater. Interfaces* **2017**, *9*, 10983–10991. [CrossRef]
219. Malinkiewicz, O.; Yella, A.; Lee, Y.H.; Espallargas, G.M.; Graetzel, M.; Nazeeruddin, M.K.; Bolink, H.J. Perovskite solar cells employing organic charge-transport layers. *Nat. Photonics* **2014**, *8*, 128–132. [CrossRef]
220. Lin, Q.Q.; Armin, A.; Nagiri, R.C.R.; Burn, P.L.; Meredith, P. Electro-optics of perovskite solar cells. *Nat. Photonics* **2015**, *9*, 106–112. [CrossRef]
221. Wen, X.R.; Wu, J.M.; Ye, M.D.; Gao, D.; Lin, C.J. Interface engineering via an insulating polymer for highly efficient and environmentally stable perovskite solar cells. *Chem. Commun.* **2016**, *52*, 11355–11358. [CrossRef]
222. Snaitha, H.J.; Grätzel, M. Enhanced charge mobility in a molecular hole transporter via addition of redox inactive ionic dopant: Implication to dye-sensitized solar cells. *Appl. Phys. Lett.* **2006**, *89*, 262114. [CrossRef]
223. Wang, Q.; Dong, Q.F.; Li, T.; Gruverman, G.; Huang, J.S. Thin insulating tunneling contacts for effcient and water-resistant perovskite solar cells. *Adv. Mater.* **2016**, *28*, 6734. [CrossRef] [PubMed]
224. Zhang, H.; Azimi, H.; Hou, Y.; Ameri, T.; Przybilla, T.; Spiecker, E.; Kraft, M.; Scherf, U.; Brabec, C.J. Improved high-efficiency perovskite planar heterojunction solar cells via incorporation of a polyelectrolyte interlayer. *Chem. Mater.* **2014**, *26*, 5190–5193. [CrossRef]
225. Li, G.; Chang, W.H.; Yang, Y. Low-bandgap conjugated polymers enabling solution-processable tandem solar cells. *Nat. Rev. Mater.* **2017**, *2*, 17043. [CrossRef]
226. Brabec, C.J.; Sariciftci, N.S.; Hummelen, J.C. Plastic solar cells. *Adv. Funct. Mater.* **2001**, *11*, 15–26. [CrossRef]
227. Tang, C.W. Two-layer organic photovoltaic cell. *Appl. Phys. Lett.* **1986**, *48*, 183–185. [CrossRef]
228. Yu, G.; Heeger, A.J. Charge separation and photovoltaic conversion in polymer composites with internal donor-acceptor heterojunctions. *J. Appl. Phys.* **1995**, *78*, 4510–4515. [CrossRef]
229. Koster, L.J.A.; Smits, E.C.P.; Mihailetchi, V.D.; Blom, P.W.M. Device model for the operation of polymer/fullerene bulk heterojunction solar cells. *Phys. Rev. B* **2005**, *72*, 085205. [CrossRef]

230. Lu, L.Y.; Yu, L.P. Understanding low bandgap polymer PTB7 and optimizing polymer solar cells based on it. *Adv. Mater.* **2014**, *26*, 4413–4430. [CrossRef]
231. He, Z.C.; Zhong, C.M.; Huang, X.; Wong, W.Y.; Wu, H.B.; Chen, L.W.; Su, S.J.; Cao, Y. Simultaneous enhancement of open-circuit voltage, short-circuit current density, and fill factor in polymer solar cells. *Adv. Mater.* **2011**, *23*, 4636–4643. [CrossRef]
232. Scharber, M.C.; Mühlbacher, D.; Koppe, M.; Denk, P.; Waldauf, C.; Heeger, A.J.; Brabec, C.J. Design rules for donors in bulk-heterojunction solar cells-towards 10% energy-conversion efficiency. *Adv. Mater.* **2006**, *18*, 789–794. [CrossRef]
233. Li, Y.F. Molecular design of photovoltaic materials for polymer solar cells: Toward suitable electronic energy levels and broad absorption. *Acc. Chem. Res.* **2012**, *45*, 723–733. [CrossRef] [PubMed]
234. Beaujuge, P.M.; Frechet, J.M.J. Molecular design and ordering effects in π-functional materials for transistor and solar cell applications. *J. Am. Chem. Soc.* **2011**, *133*, 20009–20029. [CrossRef] [PubMed]
235. Yao, H.F.; Ye, L.; Zhang, H.; Li, S.S.; Zhang, S.Q.; Hou, J.H. Molecular design of benzodithiophene-based organic photovoltaic materials. *Chem. Rev.* **2016**, *116*, 7397–7457. [CrossRef] [PubMed]
236. Xu, T.; Yu, L.P. How to design low bandgap polymers for highly efficient organic solar cells. *Mater. Today* **2014**, *17*, 11–15. [CrossRef]
237. Yu, G.; Gao, J.; Hummelen, J.C.; Wudl, F.; Heeger, A.J. Polymer photovoltaic cells-enhanced efficiencies via a network of internal donor-acceptor heterojunctions. *Science* **1995**, *270*, 1789–1791. [CrossRef]
238. Yang, H.; Shin, T.J.; Yang, L.; Cho, K.; Ryu, C.Y.; Bao, Z.N. Effect of mesoscale crystalline structure on the field-effect mobility of regioregular poly(3-hexyl thiophene) in thin-film transistors. *Adv. Funct. Mater.* **2010**, *15*, 671–676. [CrossRef]
239. Ma, W.L.; Yang, C.Y.; Gong, X.; Lee, K.; Heeger, A.J. Thermally stable, efficient polymer solar cells with nanoscale control of the interpenetrating network morphology. *Adv. Funct. Mater.* **2005**, *15*, 1617–1622. [CrossRef]
240. Zhao, G.J.; He, Y.J.; Li, Y.F. 6.5% Efficiency of polymer solar cells based on poly(3-hexylthiophene) and indene-C_{60} bisadduct by device optimization. *Adv. Mater.* **2010**, *22*, 4355–4358. [CrossRef]
241. Liao, S.H.; Li, Y.L.; Jen, T.H.; Cheng, Y.S.; Chen, S.A. Multiple functionalities of polyfluorene grafted with metal ion-intercalated crown ether as an electron transport layer for bulk-heterojunction polymer solar cells: Optical interference, hole blocking, interfacial dipole, and electron conduction. *J. Am. Chem. Soc.* **2012**, *134*, 14271–14274. [CrossRef]
242. Inganäs, O.; Svensson, M.; Zhang, F.; Gadisa, A.; Persson, N.K.; Wang, X.; Andersson, M.R. Low bandgap alternating polyfluorene copolymers in plastic photodiodes and solar cells. *Appl. Phys. A* **2004**, *79*, 31–35. [CrossRef]
243. Campbell, A.J.; Bradley, D.D.C.; Antoniadis, H. Dispersive electron transport in an electroluminescent polyfluorene copolymer measured by the current integration time-of-flight method. *Appl. Phys. Lett.* **2001**, *79*, 2133–2135. [CrossRef]
244. Svensson, M.; Zhang, F.L.; Veenstra, S.C.; Verhees, W.J.H.; Hummelen, J.C.; Kroon, J.M.; Inganäs, O.; Andersson, M.R. High-performance polymer solar cells of an alternating polyfluorene copolymer and a fullerene derivative. *Adv. Mater.* **2003**, *15*, 988–991. [CrossRef]
245. Grell, M.; Bradley, D.D.C.; Inbasekaran, M.; Woo, E.P. A glass-forming conjugated main-chain liquid crystal polymer for polarized electroluminescence applications. *Adv. Mater.* **1997**, *9*, 798–802. [CrossRef]
246. Russell, D.M.; Arias, A.C.; Friend, R.H.; Silva, C.; Ego, C.; Grimsdale, A.C.; Mullen, K. Efficient light harvesting in a photovoltaic diode composed of a semiconductor conjugated copolymer blend. *Appl. Phys. Lett.* **2002**, *80*, 2204–2206. [CrossRef]
247. Gadisa, A.; Mammo, W.; Andersson, L.M.; Admassie, S.; Zhang, F.L.; Andersson, M.R.; Inganäs, O. A new donor-acceptor-donor polyfluorene copolymer with balanced electron and hole mobility. *Adv. Funct. Mater.* **2007**, *17*, 3836–3842. [CrossRef]
248. Chen, M.H.; Hou, J.; Hong, Z.R.; Yang, G.W.; Sista, S.; Chen, L.M.; Yang, Y. Efficient polymer solar cells with thin active layers based on alternating polyfluorene copolymer/fullerene bulk heterojunctions. *Adv. Mater.* **2009**, *21*, 4238–4242. [CrossRef]
249. Umeyama, T.; Imahori, H. Design and control of organic semiconductors and their nanostructures for polymer-fullerene-based photovoltaic devices. *J. Mater. Chem. A* **2014**, *2*, 11545–11560. [CrossRef]

250. Liang, Y.Y.; Wu, Y.; Feng, D.Q.; Tsai, S.T.; Son, H.J.; Li, G.; Yu, L.P. Development of new semiconducting polymers for high performance solar cells. *J. Am. Chem. Soc.* **2009**, *131*, 56–57. [CrossRef]
251. Liang, Y.Y.; Xu, Z.; Xia, J.B.; Tsai, S.T.; Wu, Y.; Li, G.; Ray, C.; Yu, L.P. For the bright future-bulk heterojunction polymer solar cells with power conversion efficiency of 7.4%. *Adv. Mater.* **2010**, *22*, E135–E138. [CrossRef]
252. Chen, H.Y.; Hou, J.H.; Zhang, S.Q.; Liang, Y.Y.; Yang, G.W.; Yang, Y.; Yu, L.P.; Wu, Y.; Li, G. Polymer solar cells with enhanced open-circuit voltage and efficiency. *Nat. Photonics* **2009**, *3*, 649–653. [CrossRef]
253. He, Z.C.; Zhong, C.M.; Su, S.J.; Xu, M.; Wu, H.B.; Cao, Y. Enhanced power-conversion efficiency in polymer solar cells using an inverted device structure. *Nat. Photonics* **2012**, *6*, 591–595. [CrossRef]
254. Xu, Y.X.; Chueh, C.C.; Yip, H.L.; Ding, F.Z.; Li, Y.X.; Li, C.Z.; Li, X.S.; Chen, W.C.; Jen, A.K.Y. Improved charge transport and absorption coefficient in indacenodithieno[3,2-b]thiophene-based ladder-type polymer leading to highly efficient polymer solar cells. *Adv. Mater.* **2012**, *24*, 6356–6361. [CrossRef]
255. Qian, D.P.; Ye, L.; Zhang, M.J.; Liang, Y.R.; Li, L.J.; Huang, Y.; Guo, X.; Zhang, S.Q.; Tan, Z.A.; Hou, J.H. Design, application, and morphology study of a new photovoltaic polymer with strong aggregation in solution state. *Macromolecules* **2012**, *45*, 9611–9617. [CrossRef]
256. Huo, L.J.; Liu, T.; Sun, X.B.; Cai, Y.H.; Heeger, A.J.; Sun, Y.M. Single-junction organic solar cells based on a novel wide-bandgap polymer with efficiency of 9.7%. *Adv. Mater.* **2015**, *27*, 2938. [CrossRef] [PubMed]
257. Winder, C.; Sariciftci, N.S. Low bandgap polymers for photon harvesting in bulk heterojunction solar cells. *J. Mater. Chem.* **2004**, *14*, 1077–1086. [CrossRef]
258. Hou, J.H.; Park, M.H.; Zhang, S.Q.; Yao, Y.; Chen, L.M.; Li, J.H.; Yang, Y. Bandgap and molecular energy level control of conjugated polymer photovoltaic materials based on benzo[1,2-b:4,5-b′]dithiophene. *Macromolecules* **2008**, *41*, 6012–6018. [CrossRef]
259. Hou, J.H.; Chen, H.Y.; Zhang, S.Q.; Chen, R.I.; Yang, Y.; Wu, Y.; Li, G. Synthesis of a low band gap polymer and its application in highly efficient polymer solar cells. *J. Am. Chem. Soc.* **2009**, *131*, 15586–15587. [CrossRef]
260. Zhang, Y.; Hau, S.K.; Yip, H.L.; Sun, Y.; Acton, O.; Jen, A.K.Y. Efficient polymer solar cells based on the copolymers of benzodithiophene and thienopyrroledione. *Chem. Mater.* **2010**, *22*, 2696–2698. [CrossRef]
261. Zhang, M.J.; Fan, H.J.; Guo, X.; He, Y.J.; Zhang, Z.G.; Min, J.; Zhang, J.; Zhao, G.J.; Zhan, X.W.; Li, Y.F. Synthesis and photovoltaic properties of a copolymer of Benzo[1,2-b:4,5-b′]dithiophene and bithiazole. *Macromolecules* **2010**, *43*, 8714–8717. [CrossRef]
262. Tang, C.G.; Ang, M.C.Y.; Choo, K.K.; Keerthi, V.; Tan, J.K.; Syafiqah, M.N.; Kugler, T.; Burroughes, J.H.; Png, R.Q.; Chua, L.L.; et al. Doped polymer semiconductors with ultrahigh and ultralow work functions for ohmic contacts. *Nature* **2016**, *539*, 536–540. [CrossRef] [PubMed]
263. Zhao, W.C.; Qian, D.P.; Zhang, S.Q.; Li, S.S.; Inganäs, O.; Gao, F.; Hou, J.H. Fullerene-free polymer solar cells with over 11% efficiency and excellent thermal stability. *Adv. Mater.* **2016**, *28*, 4734–4739. [CrossRef] [PubMed]
264. Meng, L.X.; Zhang, Y.M.; Wan, X.J.; Li, C.X.; Zhang, X.; Wang, Y.B.; Ke, X.; Xiao, Z.; Ding, L.M.; Xia, R.X.; et al. Organic and solution-processed tandem solar cells with 17.3% efficiency. *Science* **2018**. [CrossRef] [PubMed]
265. Dou, L.T.; Gao, J.; Richard, E.; You, J.B.; Chen, C.C.; Cha, K.C.; He, Y.J.; Li, G.; Yang, Y. Systematic investigation of benzodithiophene- and diketopyrrolopyrrole-based low-bandgap polymers designed for single junction and tandem polymer solar cells. *J. Am. Chem. Soc.* **2012**, *134*, 10071–10079. [CrossRef] [PubMed]
266. Jung, J.W.; Liu, F.; Russell, T.P.; Jo, W.H. A high mobility conjugated polymer based on dithienothiophene and diketopyrrolopyrrole for organic photovoltaics. *Energy Environ. Sci.* **2012**, *5*, 6857–6861. [CrossRef]
267. Wang, C.F.; Xu, X.F.; Zhang, W.; Dkhil, S.B.; Meng, X.Y.; Liu, X.J.; Margeat, O.; Yartsev, A.; Ma, W.; Ackermann, J.; et al. Ternary organic solar cells with enhanced open circuit voltage. *Nano Energy* **2017**, *37*, 24–31. [CrossRef]
268. Fu, H.T.; Li, C.; Bi, P.Q.; Hao, X.T.; Liu, F.; Li, Y.; Wang, Z.H.; Sun, Y.M. Effcient ternary organic solar cells enabled by the integration of nonfullerene and fullerene acceptors with a broad composition tolerance. *Adv. Funct. Mater.* **2018**, 1807006. [CrossRef]
269. Xie, Y.P.; Yang, F.; Li, Y.X.; Uddin, M.A.; Bi, P.Q.; Fan, B.B.; Cai, Y.H.; Hao, X.T.; Woo, H.Y.; Li, W.W.; et al. Morphology control enables effcient ternary organic solar cells. *Adv. Mater.* **2018**, *30*, 1803045. [CrossRef]
270. Kim, Y.H.; Lee, S.H.; Noh, J.; Han, S.H. Performance and stability of electroluminescent device with self-assembled layers of poly(3,4-ethylenedioxythiophene)-poly(styrenesulfonate) and polyelectrolytes. *Thin Solid Film* **2006**, *510*, 305–310. [CrossRef]

271. He, Z.C.; Zhang, C.; Xu, X.F.; Zhang, L.J.; Huang, L.; Chen, J.W.; Wu, H.B.; Cao, Y. Largely enhanced efficiency with a PFN/Al bilayer cathode in high efficiency bulk heterojunction photovoltaic cells with a low bandgap polycarbazole donor. *Adv. Mater.* **2011**, *23*, 3086–3089. [CrossRef]
272. Na, S.I.; Oh, S.H.; Kim, S.S.; Kim, D.Y. Efficient organic solar cells with polyfluorene derivatives as a cathode interfacial layer. *Org. Electron.* **2009**, *10*, 496–500. [CrossRef]
273. Zhao, Y.; Xie, Z.Y.; Qin, C.J.; Qu, Y.; Geng, Y.H.; Wang, L.X. Enhanced charge collection in polymer photovoltaic cells by using an ethanol-soluble conjugated polyfluorene as cathode buffer layer. *Sol Energy Mater. Sol. Cells* **2009**, *93*, 604–608. [CrossRef]
274. Kirchartz, T.; Taretto, K.; Rau, U. Efficiency limits of organic bulk heterojunction solar cells. *J. Phys. Chem. C* **2009**, *113*, 17958–17966. [CrossRef]
275. Mikhnenko, O.V.; Azimi, H.; Scharber, M.; Morana, M.; Blom, P.W.M.; Loi, M.A. Exciton diffusion length in narrow bandgap polymers. *Energy Environ. Sci.* **2012**, *5*, 6960–6965. [CrossRef]
276. Nalwa, K.S.; Park, J.M.; Ho, K.M.; Chaudhary, S. On realizing higher efficiency polymer solar cells using a textured substrate platform. *Adv. Mater.* **2011**, *23*, 112–116. [CrossRef]
277. Tvingstedt, K.; Andersson, V.; Zhang, F.L.; Inganäs, O. Folded reflective tandem polymer solar cell doubles efficiency. *Appl. Phys. Lett.* **2007**, *91*, 123514. [CrossRef]
278. Chen, Y.Q.; Elshobaki, M.; Ye, Z.; Park, J.M.; Noack, M.A.; Ho, K.M.; Chaudhary, S. Microlens array induced light absorption enhancement in polymer solar cells. *Phys. Chem. Chem. Phys.* **2013**, *15*, 4297–4302. [CrossRef]
279. Tvingstedt, K.; Zilio, S.D.; Inganäs, O.; Tormen, M. Trapping light with micro lenses in thin film organic photovoltaic cells. *Opt. Express* **2008**, *16*, 21608–21615. [CrossRef]
280. Peer, A.; Biswas, R. Nanophotonic organic solar cell architecture for advanced light trapping with dual photonic crystals. *ACS Photonics* **2014**, *1*, 840–847. [CrossRef]
281. Peer, A.; Biswas, R.; Park, J.M.; Shinar, R.; Shinar, J. Light management in perovskite solar cells and organic LEDs with microlens arrays. *Opt. Express* **2017**, *25*, 10704–10709. [CrossRef]
282. He, X.M.; Gao, F.; Tu, G.L.; Hasko, D.; Huttner, S.; Steiner, U.; Greenham, N.C.; Friend, R.H.; Huck, W.T.S. Formation of nanopatterned polymer blends in photovoltaic devices. *Nano Lett.* **2010**, *10*, 1302–1307. [CrossRef] [PubMed]
283. Wiedemann, W.; Sims, L.; Abdellah, A.; Exner, A.; Meier, R.; Musselman, K.P.; MacManus-Driscoll, J.L.; Müller-Buschbaum, P.; Scarpa, G.; Lugli, P.; et al. Nanostructured interfaces in polymer solar cells. *Appl. Phys. Lett.* **2010**, *96*, 263109–263111. [CrossRef]